

鋼骨托梁抗彎接頭含梯度漸擴式  
梁翼板之耐震行為

**Seismic Performance of Steel Column-Tree Moment  
Connections with Tapered Beam Flanges**

研究生：林 群 洲

Student : Chun-Chou Lin

指導教授：陳 誠 直 博士

Adviser : Dr. Cheng-Chih Chen

國 立 交 通 大 學  
土 木 工 程 學 系  
博 士 論 文

A Thesis

Submitted to Department of Civil Engineering

National Chiao Tung University

in Partial Fulfillment of the Requirements

for the Degree of

Doctor of Philosophy

in

Civil Engineering

October, 2006

Hsinchu, Taiwan, Republic of China

中華民國九十五年十月

## 誌 謝

在交大六年攻讀碩士與博士學位的求學生涯，是我人生中最寶貴的黃金年代；追隨恩師 陳誠直教授的研究生涯，亦是我人生中最難得的學習歷程。感謝恩師多年來的指導與提攜，讓學生能以嚴謹的態度面對求學與為人處世上的種種難題，受益匪淺，師恩浩大無邊，弟子銘記在心間。於論文口試期間，承蒙國立台灣大學土木系 蔡克銓教授、鐘立來教授、國立中興大學土木系 呂東苗教授與本校 劉俊秀教授、周中哲教授對於本論文提供諸多寶貴的意見與指教，使得本論文更臻完備，在此致上最誠摯之感謝。

特別感謝財團法人中興工程科技研究發展基金會提供獎學金，使我能無後顧之憂的順利完成學業，特此誌謝；並蒙春源鋼鐵 郭金宇廠長、林祺華組長及鴻舜機械 周仁財先生對於試體製作的配合與協助，在此深表謝忱。

本論文得以順利付梓，不諱言需感謝歷年來同門的師兄弟們，南交、澤許、新梓、源興、潔祥、崇豪、文賢、智民、仁甫、文銘及建霖，於研究期間不分晝夜的鼎力協助，在此一併誌謝。此外，在這六年的研究生涯中認識許多知心的學弟妹，承載了滿滿的歡樂回憶，在此誠心的祝福大家，願你們前途無量。

最後，僅將本論文獻給我最摯愛的父母、家人及親戚們，感謝你們一直以來的支持與體諒，在精神上給予許多關懷與鼓勵，願與你們一起分享我獲得博士學位的喜悅與驕傲。

群洲 九十五年十月

# **Seismic Performance of Steel Column-Tree Moment Connections with Tapered Beam Flanges**

Student: Chun-Chou Lin

Adviser: Dr. Cheng-Chih Chen

Department of Civil Engineering  
National Chiao Tung University

## **ABSTRACT**

With a prospective advantage of better quality control of the shop welding, steel column-tree constructions are widely used in design practice of Taiwan and Japan nowadays. These connections used in the column-tree system are fabricated in the shop by welding short pieces of stub beams to the column. However, brittle fracturing of the column-tree connections was observed during the 1995 Kobe earthquake. The purpose of this study is to develop a new scheme of moment connections for steel column-tree moment-resisting frames. This connection improvement is intended to enhance the ductility of the connection by tapering portions of beam flanges following the seismic moment gradient.

A series of the finite element parametric study was conducted to investigate the effect of the taper flange geometry on the connection performance. Numerical analyses revealed that significant yielding spread around the tapered region of the beam and took place away from the column face. Full-scale subassembly specimens, consisting of a typical pre-Kobe connection and six tapered flange connections, were designed and tested to clarify their seismic performance. Experimental observations

demonstrated that the pre-Kobe specimen failed caused by a brittle fracture of the beam flange originated from the toe of the weld access hole, whereas the specimens with the tapered flange connection sustained a sufficient 5% rad story drift angle and resulted in stable energy dissipation. A design procedure of the tapered flange connection, accordingly, is proposed based on the results of the finite element analyses and full-scale connection tests. In addition, pushover analysis of frames with tapered flange connections was carried out. The performance of the tapered flange frames was compared to that of the moment-resisting frames with unreinforced connections. The results of the structural analyses demonstrated that frames with tapered flange connections have stable inelastic performance and satisfied ductility.

Key words: column-tree, special moment frame, moment connection, pushover analysis, tapered beam flange.



# 鋼骨托梁抗彎接頭含梯度漸擴式 梁翼板之耐震行為

研究生：林群洲

指導教授：陳誠直 博士

國立交通大學土木工程學系

## 摘 要

鋼骨托梁式建築由於擁有較佳工廠銲接品質的優勢，因此普遍的被台灣與日本的工程界採用。然而，於 1995 阪神地震中觀察到此型式之梁柱接頭發生非預期的脆性破壞。本研究之目的為發展新型式之托梁抗彎接頭，改良方式為逐漸擴大一部分之梁翼板使梁之彎矩容量符合耐震彎矩梯度，藉由大範圍之降伏區域提高梁柱接頭的韌性行為。

一系列有限元素參數研究用以探討各設計參數對於梯度擴翼板幾何形狀之影響。數值分析結果顯示，梯度擴翼式接頭可於梁梯度漸擴段展現廣泛的塑性降伏範圍，並將塑性鉸機制移離梁柱交接處。實尺寸梁柱接頭試驗，包括試驗一組傳統托梁式接頭與六組梯度擴翼式接頭，以驗證其耐震性能。試驗結果顯示，傳統托梁式試體於扇形開孔根部之撕裂導致梁翼板之脆性斷裂；而梯度擴翼式試體能發揮層間變位角 5% 弧度之行為，並提供穩定的消能效果。根據參數研究與實尺寸梁柱接頭試驗之結果，提出梯度擴翼式梁柱接頭之設計流程。此外，本研究利用非線性的構架側推分析，探討應用此梯度擴翼式接頭之抗彎構架的耐震特性，並與採用傳統未補強式接頭之抗彎構架比較。構架分析結果顯示，採用梯度擴翼式接頭之抗彎構架，具有穩定的非彈性行為及滿意的韌性能力。

關鍵字：托梁、特殊抗彎構架、抗彎接頭、側推分析、梯度梁翼板

# List of Contents

Abstract.....	i
List of Contents.....	iv
List of Tables.....	vi
List of Figures.....	vii
Chapter 1. Introduction.....	1
1.1 Background.....	1
1.2 Objectives of Research.....	2
1.3 Scope and Approach of Research.....	2
1.4 Organization of Dissertation.....	3
Chapter 2. Seismic Performance of Special Moment Frames.....	5
2.1 General.....	5
2.2 Review of Previous Work.....	5
2.2.1 Unreinforced moment connections with built-up box columns.....	5
2.2.2 Welded reinforced moment connections.....	7
2.2.3 Reduced beam section moment connections.....	9
2.2.4 Improvements in connection details.....	10
2.3 Proposed Column-Tree Structural Systems with Tapered Flange Connections.....	11
2.3.1 Design concept.....	13
2.3.2 Design parameters.....	13
Chapter 3. Parametric Study.....	15
3.1 General.....	15
3.2 Analytical Model Description.....	15
3.2.1 Finite element modeling.....	15
3.2.2 Performance indicators.....	17
3.2.3 Material properties.....	18
3.3 Parametric Study of Tapered Flange Connection.....	18
3.3.1 Effect of tapered flange on connection behavior.....	19
3.3.2 Effects of parameter $\beta_j$ and length of tapered zone $L_{tap}$ .....	19
3.3.3 Effect of main reinforced part $L_{w1}$ .....	20
3.3.4 Effect of tapered flange extension $L_{ext}$ .....	21
3.3.5 Plastification of tapered flange connection.....	21
Chapter 4. Full-Scale Connection Tests.....	22
4.1 General.....	22
4.2 Design of Test Specimens.....	22
4.3 Test Setup and Procedure.....	24
4.4 Observed Behavior of Test Specimens.....	25
4.4.1 Specimen PK.....	25
4.4.2 Specimens of Series W.....	25
4.4.3 Specimens of Series B.....	27
4.5 Test Results and Discussion.....	27
4.5.1 Hysteretic response and failure modes.....	27
4.5.2 Connection moment capacity and envelope response.....	30
4.5.3 Energy dissipation.....	30
Chapter 5. Evaluation of Analytical and Experimental Response.....	32
5.1 General.....	32

5.2	Evaluation of tapered flange connection subassembly .....	32
5.2.1	Global response.....	32
5.2.2	Local response .....	33
5.3	Stress and strain distribution in connection .....	34
5.3.1	Distributions of von Mises stress and equivalent plastic strain .....	34
5.3.2	Force transfer in beam .....	35
5.3.3	Strain response around connection .....	38
Chapter 6.	Design Recommendation .....	40
6.1	General.....	40
6.2	Design Procedure .....	40
Chapter 7.	Inelastic Structural Analysis for SMFs with Tapered Flange Connections.....	44
7.1	General.....	44
7.2	Design of Prototype Buildings.....	44
7.2.1	Prototype building configuration .....	44
7.2.2	Elastic analysis of prototype buildings .....	45
7.3	Nonlinear Static Pushover Analysis.....	50
7.3.1	Frame modeling and validation .....	50
7.3.2	Evaluation methodology .....	52
7.3.3	Discussion of analytical results.....	53
Chapter 8.	Summary and Conclusions .....	57
8.1	Summary .....	57
8.2	Conclusions.....	58
References	.....	62
Appendix A	Design Example .....	134
Appendix B	Design Base Shear for Building.....	136



## List of Tables

Table 3.1	Parameters used in finite element analysis .....	65
Table 4.1	Material properties of test specimens .....	66
Table 4.2	Details of test specimens .....	66
Table 4.3	Overview of test results .....	67
Table 5.1	Percentage of beam shear force for specimen W1-L03 .....	67
Table 7.1	Dead loads for studied buildings .....	68
Table 7.2	Live loads for studied buildings .....	68
Table 7.3	Distribution of design seismic forces for studied frames .....	69
Table 7.4	Tapered flanges used in studied frames .....	69
Table 7.5	Confidence levels for different confidence parameters $\lambda$ .....	70
Table 7.6	Confidence level evaluation for studied frames .....	71





## List of Figures

Figure 1.1	Connection details of web-bolted flange-welded pre-Northridge moment connection.....	72
Figure 2. 1	Connection details between H-shaped beam and welded built-up box column.....	73
Figure 2.2	A schema of SESNET electroslag welding.....	73
Figure 2.3	Examples of reinforced moment connections.....	74
Figure 2.4	Reinforced moment connection with wing plates. (陳嘉有 1995).....	75
Figure 2.5	Different RBS configurations.....	75
Figure 2.6	Weld access hole configurations: (a) a quarter-circular shape; (b) a modified shape recommended by FEMA-350.....	76
Figure 2.7	Steel column-tree moment frame.....	76
Figure 2.8	Typical pre-Kobe column-tree connections: (a) Through-diaphragm connection; (b) Interior-diaphragm connection.....	77
Figure 2.9	Widened flange connection configuration. (Chen et al. 2006).....	78
Figure 2.10	Normalized moment versus total plastic rotation curves for specimens W10-L2 and W08-L1. (Chen et al. 2006).....	78
Figure 2.11	Geometry of tapered flange connection.....	79
Figure 2.12	Comparison with seismic moment demand and flexure capacity: (a) for tapered flange connections; (b) for widened flange connections.....	79
Figure 3.1	Geometry of 3-D structural solid element SOLID45 (ANSYS 2002)....	80
Figure 3.2	Boundary conditions and meshes of finite element model.....	80
Figure 3.3	Details of weld access hole.....	81
Figure 3.4	Critical sections of pre-Kobe connection: (a) at CJP groove weld; (b) at root of WAH.....	82
Figure 3.5	Distributions of normalized principal stresses and PEEQ indices along beam flange width at CJP weld and root of WAH: (a) normalized principal stress at 0.5% rad story drift angle; (b) PEEQ indices at 4% rad story drift angle.....	83
Figure 3.6	Effect of different values of parameter $\beta_j$ and length of tapered part $L_{tap}$ on PEEQ indices at 4% rad story drift angle: (a) at borders of CJP weld; (b) at root of WAH.....	84
Figure 3.7	Effect of length of main tapered flange reinforced part $L_{wl}$ on PEEQ indices at 4% rad story drift angle.....	85
Figure 3.8	Effect of length of tapered flange extension $L_{ext}$ on PEEQ indices along root of WAH between column-tree and link beam at 4% rad story drift angle.....	85
Figure 3.9	Longitudinal plastic strain contours for different configuration of connections during 4% rad story drift angle.....	86
Figure 3.10	Contour plots of plastic equivalent strain for different configurations of connections at 4% rad story drift angle.....	86
Figure 4.1	Connection details of specimen PK.....	87
Figure 4.2	Connection details of specimen W1-L05, W1-L03, W2-L03, and W3-L03.....	88
Figure 4.3	Connection details of specimen B1-L03 and B2-L03.....	89
Figure 4.4	Overall view of test setup.....	90
Figure 4.5	Loading history.....	91

Figure 4.6	The definition of story drift angle for test assembly (FEMA-350 2000)	91
Figure 4.7	Failure mode of typical pre-Kobe specimen PK	92
Figure 4.8	Fracture of beam flange groove weld of specimen W3-L03 at 4% rad story drift angle	92
Figure 4.9	Plastic hinge formation followed by local buckling at 5% rad story drift angle: (a) specimen W1-L05; (b) specimen W1-L03	93
Figure 4.10	Slight cracking at root of weld access hole of specimen B1-L03 at 4% rad story drift angle	94
Figure 4.11	Local buckling of beam flanges and beam web at 5% rad story drift angle: (a) specimen B1-L03; (b) specimen B2-L03	95
Figure 4.12	Hysteresis response of specimen PK: (a) normalized moment at column face versus story drift angle; (b) normalized moment at column face versus total plastic rotation	96
Figure 4.13	Normalized moment versus rotation responses of column-tree tapered flange connection specimens: (a) in terms of story drift angle; (b) in terms of total plastic rotation	97
Figure 4.14	Normalized moment versus rotation responses of web-bolted flange-welded tapered flange connection specimens: (a) in terms of story drift angle; (b) in terms of total plastic rotation	98
Figure 4.15	Ratios of maximum test moment to calculated moment capacity of the specimens PK, W1-L03, and W2-L03 along the length of the beam	99
Figure 4.16	Envelope relationships of normalized moment versus story drift angle: (a) specimens with column-tree connection; (b) specimens with web-bolted flange-welded connection	100
Figure 4.17	Comparison of test specimen energy dissipation	101
Figure 5.1	Comparison of experimental and analytical beam tip load versus beam tip displacement response of specimen W1-L03	101
Figure 5.2	Position of strain gauges: (a) specimen PK; (b) tapered flange specimens	102
Figure 5.3	Verification of longitudinal strain distributions at line F40 for specimen W1-L03	103
Figure 5.4	Verification of longitudinal strain distributions around tapered zone of beam flange for specimen W1-L03	104
Figure 5.5	Von Mises stress contours, equivalent plastic strain contours, and yielding behavior during testing of specimen W1-L03: (a) at 1% rad story drift angle; (b) at 2% rad story drift angle	105
Figure 5.5 (continued)	Von Mises stress contours, equivalent plastic strain contours, and yielding behavior during testing of specimen W1-L03: (c) at 3% rad story drift angle; (d) at 4% rad story drift angle	106
Figure 5.6	Normalized shear stress distributions along beam web depth at 0.5% rad story drift angle	107
Figure 5.7	Normalized shear stress distributions along beam flange width at 0.5% rad story drift angle	108
Figure 5.8	Normalized longitudinal stress distributions along beam web depth at 0.5% rad story drift angle	109
Figure 5.9	Normalized longitudinal stress distributions along beam flange width at 0.5% rad story drift angle	110
Figure 5.10	Normalized shear stress distributions along beam web depth at 4% rad story drift angle	111

Figure 5.11	Normalized shear stress distributions along beam flange width at 4% rad story drift angle. ....	112
Figure 5.12	Normalized longitudinal stress distributions along beam web depth at 4% rad story drift angle. ....	113
Figure 5.13	Normalized longitudinal stress distributions along beam flange width at 4% rad story drift angle. ....	114
Figure 5.14	Distributions of normalized longitudinal strains along beam flange width at line F-40 between specimens PK and W10-L03. ....	115
Figure 5.15	Distributions of normalized longitudinal strains across tapered zone of beam flange for column-tree specimens: (a) specimen W1-L05; (b) specimen W1-L03; (c) specimen W2-L03; (d) specimen W3-L03. ....	116
Figure 5.16	Distributions of normalized longitudinal strains across tapered zone of beam flange for web-bolted flange-welded specimens: (a) specimen B1-L03; (b) specimen B2-L03. ....	117
Figure 6.1	Moment gradient of tapered flange connection .....	118
Figure 7.1	Floor plane view of prototype building. ....	119
Figure 7.2	Design details of prototype buildings: (a) five-story frame; (b) fifteen-story frame. ....	120
Figure 7.3	Analytical models for prototype buildings: (a) model UR-5F; (b) model TF-5F. ....	121
Figure 7.4	Analytical models for connection subassembly: (a) model UR-C; (b) model TF-C. ....	122
Figure 7.5	Properties of pushover hinge for model UR-C used in SAP2000. ....	123
Figure 7.6	Properties of pushover hinge for model TF-C used in SAP2000. ....	124
Figure 7.7	Verification of experimentally cyclic and numerically monotonic responses: (a) model UR-C; (b) model TF-C. ....	125
Figure 7.8	Pushover curves of normalized base shear versus roof drift for five-story frames. ....	125
Figure 7.9	Distribution of plastic hinges for UR-5F at 2.1% rad roof drift. ....	126
Figure 7.10	Distribution of plastic hinges at CP level (3.22% rad roof drift): (a) for UR-5F; (b) for TF-5F. ....	126
Figure 7.11	Pushover curves of normalized base shear versus roof drift for fifteen-story frames. ....	127
Figure 7.12	Distribution of plastic hinges for UR-15F at 1.5% rad roof drift. ....	127
Figure 7.13	Story drift angle of UR-15F at 1.5% rad roof drift. ....	128
Figure 7.14	Distribution of plastic hinges for UR-15F at IO level (0.85% rad roof drift). ....	128
Figure 7.15	Distribution of plastic hinges for TF-15F at IO level (0.85% rad roof drift). ....	129
Figure 7.16	Distribution of plastic hinges for TF-15F at CP level (2.5% rad roof drift). ....	130
Figure 7.17	Distribution of plastic hinges for UR-15F at CP level (2.5% rad roof drift). ....	131
Figure 7.18	Distribution of plastic hinges for TF-15F at 2.7% rad roof drift. ....	132
Figure 7.19	Structural demands at IO and CP performance levels: (a) for five-story frames; (b) for fifteen-story frames. ....	133

# Chapter 1. Introduction

## 1.1 Background

Special moment frames (SMFs) are widely used in middle- and high-rise buildings because the structural systems are highly ductile and able to dissipate energy by developing inelastic deformation during strong ground excitation. Typical connection used in the moment frame is a web-bolted flange-welded moment connection, often called “pre-Northridge connection”. Figure 1.1 presents details of this moment connection. The beam flanges are designed to resist the beam bending moment, with the beam web resisting the beam shear force. Therefore, the beam flanges are field welded to the column flange by complete joint penetration (CJP) single bevel groove welds while the beam webs are field bolted to a shear tab which is shop welded to the column flange. Moreover, weld access holes (WAHs) are required to cut on the beam web for performing the CJP groove welds.

Unfortunately, the 1994 Northridge earthquake in United States and the 1995 Kobe earthquake in Japan caused widespread damage in these SMFs, mainly due to the premature failure in the moment connections. Weld defect is one of the causes that extremely affect the performance of the connections for developing their ductile behavior. Poor field welding practice is by far the most critical that caused some possible defects in the welds.

As an alternative to avoid field welding, a column-tree construction has been used in the steel structural systems. The column-tree is fabricated by welding a short piece of stub beam, generally 600 to 1,000 mm long, to the column in the shop. Unlike the pre-Northridge connection case, the critical welding of the beam-to-column joint

is performed in the shop, which that can provide a better quality control. Those defects caused by the field welding are intentionally reduced because of good quality of welding in the shop. Unavoidably, the column-tree construction should be possible to increase some handling costs.

However, several of the column-tree moment connections were damaged during the 1995 Kobe earthquake. Many brittle fractures of the beam flanges caused by the same failure mode as the pre-Northridge connections were still initiated from the beam-to-column groove welds and the toe of WAHs (Nakashima et al. 1998). The premature failures, therefore, have arisen many questions on the reliability of column-tree moment connections for the seismic application.

## **1.2 Objectives of Research**

The purpose of this study is to develop a ductile column-tree moment connection, achieving by widening the beam flange of the stub beam. A parametric study was conducted to investigate the effects of geometrical variables of the tapered flange on the inelastic behavior of the moment connections. Cyclic behavior of the connections was further verified by the full-scale experiment. A design procedure is recommended based on the results of the parametric and experimental studies.

## **1.3 Scope and Approach of Research**

Many researchers have investigated the performance of moment connections used for SMFs. These investigations mainly focused on connections between H-shaped columns and H-shaped beams. However, column-tree SMFs with welded built-up box columns are very common in Taiwan and Japan design practice. This dissertation, therefore, analytically and experimentally investigates the cyclic behavior of the

column-tree moment connection with a tapered flange. The scope of the research consisted of eight tasks as follows:

1. Develop the tapered flange connection concept and identify design parameters of a tapered flange.
2. Investigate the force transfer mechanism and behavior of the tapered flange connection through nonlinear finite element analyses.
3. Investigate the geometrical variables of the tapered flange that influence the connection behavior.
4. Design and construct seven full-scale specimens on the basis of the results of the parametric study.
5. Conduct the full-scale connection tests.
6. Evaluate the seismic performance of moment connections with and without tapered flanges.
7. Develop preliminary design recommendations for the tapered flange connection used for SMFs.
8. Evaluate the structural behavior of SMFs with and without tapered flange connections.

#### **1.4 Organization of Dissertation**

This dissertation is organized into eight chapters and a list of references. Chapter 2 evaluates the seismic performance of SMFs. Previous experimental and analytical

studies conducted on a variety of connection improvements are summarized in this chapter. Design concept and design parameters of tapered flange moment connections used for column-tree SMFs are also presented.

Chapter 3 presents the analytical program of the nonlinear finite element analyses. Information on the finite element modeling, performance indicators, and material properties are provided. Afterward a parametric study is conducted to investigate the effects of design parameters of the tapered flange on the connection behavior. Chapter 4 presents the experimental program of the full-scale connection tests. The details of the design of test specimens, test setup, and loading procedure are described. Test results are presented through the hysteretic response and failure modes, the connection moment capacity, and energy dissipation of each test specimen. Chapter 5 presents the force transfer mechanism in the tapered flange connection. Information on comparison with simulated and experimental responses of the tapered flange specimen is also mentioned in this chapter. Chapter 6 presents the design procedure for designing the tapered flange. A systematic design example is described in Appendix A.

Chapter 7 presents the designs and analyses of SMFs with tapered flange connections. Both linear elastic analysis and nonlinear static pushover analysis are conducted to evaluate the performance of the five and fifteen-story frames under specified seismic levels. Chapter 8 describes summary and conclusions for beam-to-box column moment connections improved by tapered flanges. References are listed following Chapter 8.

## **Chapter 2. Seismic Performance of Special Moment Frames**

### **2.1 General**

SMF system has been popularly used for modern steel buildings because this structural system is simple and economical. The design philosophy of the moment-resisting system assumes that the frame is highly ductile and is able to dissipate large energy by forming plastic deformation at their connections under strong ground excitation. These connections have to provide significant ductility and sustain a story drift angle of at least 4% rad (AISC 2005a). Nevertheless, the 1994 Northridge and the 1995 Kobe earthquakes caused serious failure in these welded moment connections. Connections developed limited yielding and plastic deformation followed by a brittle fracture at the beam-to-column joints (Miller 1998; Nakashima et. al 1998). While the connections lacked the expected ductility, structural capability could be significantly diminished that caused urgently structural damage.

### **2.2 Review of Previous Work**

Issues concerning the seismic behavior of steel moment connections have been addressed based on extensive analytical and experimental studies since the earthquakes. Some benefits and shortcomings regarding a variety of connection improvements, such as strengthening the connection or weakening the beam section, are summarized in this section.

#### **2.2.1 Unreinforced moment connections with built-up box columns**

The box column can provide a great biaxial bending capacity to resist the irregular



seismic shaking acting in both directions. Therefore, box columns and H-shaped beams have been commonly used for modern steel buildings in some countries such as Taiwan and Japan.

Figure 2.1 illustrates the connection details of a box column in practice. Most box columns used in steel constructions are built-up by welding four steel plates using a full penetration groove weld. Diaphragms (or so called continuity plates) are important to the seismic performance of connections, because they have to transfer effectively the beam forces to the column. However, installing such a diaphragm is inherently difficult. A special welding process must be used to weld the diaphragms inside the box column. First, a penetration groove weld is performed to join the diaphragm to a pair of opposite column plates. Then the SESNET (Simplified Electro Slag Welding Process with Non-consumable Elevating Tip) welding process is used to weld the diaphragm to the other pair of column plates. Figure 2.2 shows a schema of the SESNET welding. A non-consumable nozzle, filled suitable fluxes and wires, is inserted in the narrow gaps between the diaphragm and the column plate. Great heat, arising from a short circuit of a high electric resistance of wires, continuously melts the intersection between base metal and wires to achieve an objective of jointing the diaphragm and the box column.

Only limited test data concerning the beam-to-box column connections are available. Chen et al. (2004) investigated the cyclic behavior of steel moment connections between H-shaped beams and built-up box columns. Six large-scale specimens were designed and fabricated using a built-up  $500 \times 500 \times 35 \times 35$  (mm) box column and an  $H700 \times 300 \times 13 \times 24$  (mm) beam. One of the test specimens was the unreinforced connection using pre-Northridge details, and other test specimens were the reinforced connections using rib plates and wing plates. The unreinforced

connection failed due to fracture at the CJP groove weld and near the WAH region during the cycle of 2.3% rad story drift angle.

Kim et al. (2004) tested two full-scale moment connections to welded box columns fabricated using pre-Northridge connection details. Test results revealed that both specimens failed by a brittle fracture of CJP weld between the beam flange and the column during a story drift angle of less than 1% rad, which resulted in no plastic rotation in the connections.

### **2.2.2 Welded reinforced moment connections**

The intention of welded reinforced moment connections is proposed to reduce stress and strain demands in the vulnerable region near the face of the column, and to relocate the high plastic strains into the beam. Figure 2.3 shows four types of strengthening schemes commonly used for steel moment connections, including cover plates, wing plates, rib plates, and haunches. More details are described in the following.

The approaches of plate-reinforced connections are intended to strengthen the joint by welding cover plates, wing plates or others. Afterward stresses in the CJP groove welds can be reduced because the beam section near the beam-to-column joint is enlarged. Full-scale connection tests of cover plate connections (Engelhardt and Sabol 1998; Kim et al. 2002a, 2002b) showed significant improvement in ductility of the connection. However, some of the test specimens experienced premature failure. An issue based on the experimental research conducted by Engelhardt and Sabol (1998) was raised regarding the presence of weld defects, heat-affected zones (HAZs) due to welding, and the use of excessive reinforcement. A thicker cover plate would result in

the higher potential for weld defects and could cause HAZ problems due to the larger weld area. Figure 2.4 displays the reinforced connections with flat wing plates (陳嘉有 1995). Test results clarified premature crack initiation was observed at the end tips of the weldment between the wing plates and the beam flange, due to the localized stress concentration at the tips of the wing plates.

In a rib-reinforced connection, a tapered triangular rib plate is frequently used. Tests conducted by Engelhardt et al. (1995) and Anderson and Duan (1998) demonstrated that connections reinforced with tapered triangular ribs exhibited sufficient hysteretic behavior with plastic rotation ranging from 2.5% to 3.0% rad. Chen et al. (2005a) tested two connections reinforced by a single triangular rib welded to the centerline of each beam flange. One connection failed owing to a brittle fracture in the beam flange at the rib tip, while the other displayed stable hysteretic behavior. Chen et al. (2003, 2004) and 陳誠直等人 (2003) tested other rib-type connections using modified rib plates. A single lengthened rib is welded to each beam flange in the plane of the beam web. Examining the results from the tests presented, it is obvious that the rib-reinforced connection can provide sufficient ductility during the large deformation, with a story drift angle of at least 4% rad and plastic rotation greater than 3% rad. Hysteretic loops demonstrate this moment connection has stable energy dissipation capacity under cyclic loading.

Another strengthening scheme is to reinforce the beam around a connection by welding a triangular haunch to the beam bottom flange. Ideally, the beam portion within the haunch region would remain elastic during the large inelastic deformation, so that the stresses in the beam flange groove welds are diminished. Because of this strengthening, redundancy for this type of reinforced connection is much more than that

of reduced beam section (RBS) connection. Uang et al. (2000) tested six full-scale specimens using the welded haunch and RBS for rehabilitation of pre-Northridge moment connections; three of them incorporated lightweight concrete slabs. Welding a triangular haunch beneath the beam bottom flange significantly improved the cyclic performance.

### **2.2.3 Reduced beam section moment connections**

The design approach of an RBS connection is similar to that of a reinforced connection. The RBS is intended to control the formation of plastification moving away from the column face, and to diminish a possibility of brittle fracturing at the beam flange groove welds. In RBS moment connections, portions of the beam flanges are trimmed to force plastic hinging to occur at a desirable location of the beam, whereas reinforced moment connections are made stronger than the beam by strengthening the connections with cover plates, ribs or haunches. The fabrication of the RBS is simple and economical, as compared to the connection reinforcement. However, weakening parts of the beam sections may result in reduction in elastic stiffness of SMFs (Engelhardt et al. 1998). An RBS with small reduction in the beam flanges may do negligible to reduce stress levels in the beam-to-column joint. On the other hand, the RBS with excessive reduction in the beam flanges may cause premature lateral-torsional buckling of the beam in the RBS.

Numerous studies and testing have been conducted on RBS moment connections under cyclic loading (Plumier 1997; Chen et al. 1996, 2001; Engelhardt et al. 1998; Popov et al. 1998; Jones et al. 2002; Zhang and Ricles 2006). These investigations primarily focused on three different shapes of RBS cuts such as a constant cut, a radius cut, and a tapered cut (Figure 2.5). The results from laboratory tests demonstrated that

the RBS connection has exhibited acceptable levels of ductility. Nevertheless, small number test data are available about the performance of this type of connection with a welded built-up box column. Chen et al. (1996) conducted successful tests on RBS moment connections with tapered cuts. All specimens were fabricated using a built-up  $\square 500 \times 500 \times 20 \times 20$  (A572 Grade 50) box column and an  $H600 \times 300 \times 12 \times 20$  (A36) beam. The ductility of the test specimens was significantly enhanced without a striking loss of connection capacity, and an enlarged plastic zone was obtained in the tapered area away from the critical CJP groove weld.

#### **2.2.4 Improvements in connection details**

Some critical factors could significantly affect the connection performance, including weld toughness, geometry and size of WAH, and panel zone deformation (Lu et al. 2000). The size and shape of WAH is considered to have dominant effects on the connection behavior. As demonstrated in Figure 1.1, WAHs are needed to be cut on the beam web to perform the CJP flange welding between the beam flange and the column flange. The WAH near the beam top flange is used for placing the steel backing bar whereas the bottom one is used for performing the groove welds. However, the presence of WAH in the beam web causes stress concentration on the center of the beam flange near the root of the WAH region because of the abrupt change in WAH geometry (El-Tawil et al. 2000). As a result, the combination of high stress and strain concentrations results in a brittle fracture at the beam-to-column joints, as documented in laboratory tests (Stojadinović et al. 2000; Chen et al. 2004, 2005a). Figure 2.6 shows two different WAH configurations: one is commonly used in Taiwan; the other is recommended by FEMA-350 (2000). A description of related analytical and experimental studies is presented as follows.

Lu et al. (2000) conducted a series of different WAH configurations using the nonlinear finite element program ABAQUS. Nine various WAH configurations were investigated to evaluate the connection details for fracture potential. The conventional WAH configuration with a circular shape (diameter of 20 mm) was found to have a high concentration of plastic strain in the middle of the beam flange, at the toe of WAH. However, the plastic strain demand of the modified WAH configuration was half that of conventional type, which exhibited the lowest potential for crack initiation among the different WAH configurations.

Ricles et al. (2002) tested eleven full-scale interior and exterior welded unreinforced moment connections. All beams used a W36×150 section. The columns used for the exterior connections were a W14×311 section, while W14×395 and W27×258 column sections were used for the interior connections. Test results demonstrated that connections using a high toughness weld metal and modified connection details, including beam web attachment detail and WAH geometry, responded with good connection performance. No fracture near the WAH region was observed during the testing, with a story drifts angle of up to 5% rad being achieved.

### **2.3 Proposed Column-Tree Structural Systems with Tapered Flange Connections**

A column-tree system is one of the constructional schemes used for the SMF. Figure 2.7 demonstrates the column-tree construction. Short pieces of stub beam are fabricated and welded to the column in the shop, forming a column-tree. After the field erection of these tree-like columns, a mid-portion of the link beam is then spliced to the stub beam with bolted connections. This shop welded and field bolted type of the connection is often called “pre-Kobe connection”. Figure 2.8 illustrates two typical

types of column-tree connection. One is the through-diaphragm connection; the other is the interior-diaphragm connection. Of course, fabricating such column-tree connections should be possible to increase costs.

Unfortunately, the 1995 Kobe earthquake caused serious failure in some of these typical pre-Kobe moment connections used for the steel column-tree buildings. Since the earthquake, Nakashima et al. (1998) investigated and reported that premature brittle fractures of the beam flanges were found in the beam-to-column flange groove welds where it should have been able to achieve better welding quality. Limited yielding and plastic deformation developed between the columns and the beams was observed in the connections. The unexpected failures raised many doubts regarding a vantage of the quality control on these shop welded-field bolted connections.

The use of a widened flange plate (Chen et al. 2006) is one of strengthening schemes to improve the seismic performance of column-tree moment connections. The beam flanges close to the column face are enlarged to reinforce the beam-to-column joint, reducing stress demand at the beam flange groove welds. Figure 2.9 shows the geometry of a widened flange connection used in column-tree SMFs. The details of this connection include a stub beam with widened beam flanges and no weld access hole. Rather than strengthening being provided by a flat triangular stiffener on both sides of the beam flange, a piece of widened flange plate is used to prevent crack initiated in the welding fusion zone between the stiffener and the beam flange. Test results showed that widened flange connections were able to develop satisfactory cyclic performance. Full hysteretic loops of normalized moment versus total plastic rotation, revealed in Figure 2.10, demonstrated this moment connection had stable energy dissipation capacity under cyclic loading.

The purpose of this study is to enhance the ductile behavior of the column-tree moment connection by further improving the geometry of the widened beam flange according to previously related research conducted by Chen et al. (2006).

### 2.3.1 Design concept

Figure 2.11 depicts the configuration of a tapered flange moment connection. The design objective is to develop a large plastic zone in the beam to enhance the ductile behavior of the moment connection. This intention is achieved by tapering the portion of flange plates in the stub beam along the seismic moment gradient, thus a wide portion of yielding in the tapered zone can possibly provide much energy dissipation. Figure 2.12(a) shows the moment gradient of the flexural capacity and seismic moment demand of the beam. Neglecting the effect of gravity load, the seismic moment demand is the required flexural strength assumed a half-span of the cantilever beam in the moment frame under the seismic condition. Unlike previous studies conducted by Chen et al. (2006) shown in Figure 2.12(b), an extent of large yielding in the beam is intended to develop simultaneously at the overlap of two lines of flexural capacity and seismic moment demand. Furthermore, the beam flange close to the column face has to be enlarged more than the tapered zone of the beam flange to ensure the sufficient capacity at the beam-to-column joint.

### 2.3.2 Design parameters

According to the design idea of the improvements in the connection, two primary variables governing the behavior of a tapered flange connection are defined as a reinforcement ratio of the tapered flange  $\beta_j$  and the length of a tapered part  $L_{tap}$ , respectively. Figure 2.11 indicates these design variables. The parameter  $\beta_j$  is a main



reinforcement factor at the beam-to-column joint and is defined as a ratio of the flexural capacity,  $M_{p,j}$ , to the seismic moment demand,  $M_{dem,j}$  (i.e.,  $\beta_j = M_{p,j} / M_{dem,j}$ ), ensuring sufficient safety at the column face. Another primary parameter  $L_{tap}$  represents the length of the tapered region of the beam flange and purposes to provide a larger deformation capacity in the beam.

There are remaining variables: the length of a main reinforced part  $L_{w1}$ , the length of a curved transition part  $L_{w2}$ , and the length of an extension part  $L_{ext}$ .  $L_{w1}$  is used to assure the plastic deformation of the beam moving away from the critical beam-to-column interface. Considering the effect of force transferring from the main reinforced part to the tapered flange smoothly, the curved transition  $L_{w2}$  of 50 mm is used in this study. The tapered flange extension  $L_{ext}$  proposes to reduce the stress and the strain demand on the splice joint between the column-tree and the link beam, preventing the occurrence of the unexpected fracture. Due to the complexity of force transfer mechanism within the connection region, detailed parametric studies are needed to clarify the effect of each design parameter on the behavior of a tapered flange connection, as presented in Chapter 3.

## **Chapter 3. Parametric Study**

### **3.1 General**

Finite element analysis is currently in widespread use in not only aeronautic structures but also mechanical and civil engineering structures. Analytical results would become more authentic through an assumption of realistic material properties and a validation of analytical modeling. A previous analytical study conducted by Chen et al. (2005b) had shown that both global and local responses of the connection subassemblage could be simulated accurately using nonlinear finite element models. Accordingly, the general-purpose nonlinear finite element analysis program ANSYS (2002) was utilized to model the varied configurations of the tapered flange connection and further to study the effects of design variables on the connection behavior.

### **3.2 Analytical Model Description**

#### **3.2.1 Finite element modeling**

The finite element models of connection subassemblage, consisting of three-dimensional structural solid elements with 24 nodal degrees of freedom (Figure 3.1), were used in the analytical study. The connection subassemblage represents an exterior T-shaped connection isolated from a moment frame. Figure 3.2 shows the finite element meshes and boundary conditions of the typical analytical model. For a SMF under a lateral loading, the inflection points of the column and the beam are generally assumed to occur at the mid-height of the column and the half-span of the beam. So that in the finite element analysis roller and pinned supports were modeled at each end of the column, as well as a monotonic incremented displacement was applied to the beam

tip. Furthermore, due to the structural symmetry with respect to the mid-plane at the beam web and the column section, only half of the connection subassembly was modeled to decrease the computational effort.

Each of models consist of a H-shaped H700×300×13×24 (dimensions in mm for depth, width, web thickness, and flange thickness, respectively) beam, having a length of 3,600 mm from the beam end to the column face, and a box □550×550×28×28 column, 3,000 mm long between the hinged supports at the ends of the column. The conventional WAH configuration with a quarter-circular shape, as shown in Figure 3.3, was included in the models to evaluate the local effect of the connection details. Meanwhile, the root of the CJP single bevel groove welds located on the interior sides of both top and bottom flange was modeled to simulate the pre-Kobe connection details. However, backing bars and runoff tabs did not include in the models.

A series of seventeen finite element models was designed and selected for detailed evaluation, as listed in Table 3.1. An unreinforced connection was modeled to represent the pre-Kobe column-tree moment connection, to clarify the improvement of the tapered beam flange on the connection behavior. Other finite element models with different configurations were designed to reveal other design variables. A control model of tapered flange connection used the following design properties:

- (1)  $\beta_j = 1.2$ ;
- (2)  $L_{tap} = 0.3 d_b$  (210 mm length);
- (3)  $L_{w1} = 0.5 b_f$  (150 mm length from the column face);
- (4)  $L_{w2} = 50$  mm;

(5)  $L_{ext}=0.5 d_b$  (350 mm length from the end of the stub beam)

where  $b_f$  is the width of the beam flange; and  $d_b$  is the depth of the beam section.

The remaining models changed one parameter at a time from among parameters to eliminate the interactive effects between these parameters. Table 3.1 tabulates dimensions of the tapered flange used in the models that had the width of the flange enlargement ranging from 372 to 530 mm and the length of the stub beam ranging from 410 to 1110 mm.

### 3.2.2 Performance indicators

The potential for cracking is evaluated through a tendency of stress and strain states at different levels of a story drift angle. Hence, the principal stress is used to assess the stress distribution in the elastic range, as well as the plastic equivalent strain (PEEQ) is also employed to criticize the local plastic strain demand in the inelastic range. The plastic equivalent strain is defined as

$$PEEQ = \sqrt{\frac{2}{3} \varepsilon_{ij} \varepsilon_{ij}} \quad (3.1)$$

where  $\varepsilon_{ij}$  represents plastic strain components in directions  $i$  and  $j$ . Undoubtedly, higher PEEQ reveals a higher demand for plastic strain. Meanwhile, these two stress and strain indicators are normalized for the purpose of indicating their inclination clearly: the principal stress is normalized by the yield strength  $F_y$ , while the PEEQ is divided by the yield strain  $\varepsilon_y$  defined as the PEEQ index.

Two critical sections of the connection, along the beam flange width at the locations of the CJP groove weld and the root of the WAH, are selected to study the

stress and strain statuses based on the fracturing locations in the pre-Kobe moment connections reported in Nakashima et al. (1998). Figure 3.4 displays these critical sections, presented by lines running across the width of the beam flange. Besides, story drift angles of 0.5% and 4% rad are chosen to study the elastic behavior and high plastic deformation state of the connection subassemblage, respectively.

### **3.2.3 Material properties**

Nominal yield stress of A572 Grade 50 steel used to model the beam and column was set equal to 345 MPa. The expected material overstrength factor  $R_y$ , recommended in AISC (2005a) was also considered to simulate the realistic material properties of the steel. For simplification, a bilinear isotropic hardening behavior was used for simulating the stress-strain relations of the structural steel and the weld; a rate-independent plasticity model was especially used in the inelastic behavior. The modulus in the strain-hardening range of the steel and the weld adopted 3% and 1.5% of the modulus of the elasticity, respectively. Besides, to determine the plastification of the analysis models, von Mises yielding criterion with the associated flow rule and the isotropic hardening rule was used.

### **3.3 Parametric Study of Tapered Flange Connection**

Finite element analysis can provide better preliminary evaluation of stress and strain states in tapered flange connections and to compare behaviors of connection configurations relative to different design parameters. A set of parametric analyses, therefore, was conducted to investigate the effectiveness of the tapered flange connection.

### 3.3.1 Effect of tapered flange on connection behavior

Figure 3.5 demonstrates the normalized principal stresses at 0.5% rad story drift angle and PEEQ indices at 4% rad story drift angle along the width of the beam flange, at the CJP groove weld and the root of the WAH. It should be noticed that the tapered flange connection model was a control model using parameters that had been mentioned previously. Both connections show high stress concentration at the tips of the groove weld during a story drift angle of 0.5% rad, owing to the distribution of stiffness contributed from the cross section of the box column. An identical phenomenon was observed in the middle of the beam flange, at the root of the WAH, because of the unevenly geometry of the WAH shape. However, when the tapered flange connection model proceeded to the inelastic range of 4% rad story drift, 62.5% and 42.4% reduction rates of the maximum PEEQ indices at the edges of the groove weld and at the root of the WAH were obtained, respectively, compared to the pre-Kobe connection model. Certainly, the presence of the enlarged beam flange considerably reduced the high concentration of plastic strain at the beam-to-column interface and the WAH region, diminishing the potential fracture at these locations.

### 3.3.2 Effects of parameter $\beta_j$ and length of tapered zone $L_{tap}$

Four different values of  $\beta_j$  were studied to elucidate the effect of the reinforcement ratio of the tapered flange on the response of the connection subassembly. The reinforcement ratios were set equal to 1.05, 1.10, 1.20, and 1.25, with the width of the flange enlargement in the range of 344 to 530 mm. Additionally, to clarify the influence of the plasticity capacity in the tapered zone of the beam flange on the connection performance, design parameter  $L_{tap}$  was varied by changing the

region in the tapered zone from  $0.3 d_b$  to  $0.8 d_b$  (dimensions ranging from 210 to 560 mm). The analytical results are summarized in Figure 3.6, where the values of the PEEQ indices at 4% rad story drift angle were captured from the critical locations of the beam flange groove weld and the root of the WAH. The PEEQ index is shown to be largest for the traditional pre-Kobe column-tree connection. It is obvious that the higher flange reinforcement causes the lower plastic strain demand; furthermore, using the larger tapered zone can also result in lower PEEQ index. With the value of  $\beta_j$  larger than 1.2, increasing the length of the tapered zone from  $0.3 d_b$  to  $0.8 d_b$  has a slight variation in the improvement of the local plastic strain demands. Overall, higher parameter  $\beta_j$  increasing the deformation capacity of the groove welds results in higher margin of safety at the junction of the beam-to-column connection.

### 3.3.3 Effect of main reinforced part $L_{wl}$

Considering a plastic hinge formed a sufficient distance away from the column face, the lengths of a main reinforced part are set equal to  $0.17 b_f$ ,  $0.33 b_f$ , and  $0.5 b_f$  for the models, with the corresponding lengths are 50 mm, 100 mm, and 150 mm, respectively. Figure 3.7 demonstrates the effects of the different values  $L_{wl}$  on PEEQ indices at a story drift angle of 4% rad. Results show that the model with smaller  $L_{wl}$  have higher PEEQ index at the root of the WAH, compared with the model with larger  $L_{wl}$ ; the maximum PEEQ index decreases from 15.4 to 12.5, a decrease of 18.8%, as the main reinforced zone  $L_{wl}$  increase from 50 mm to 150 mm. However, a reverse tendency was noted in the CJP groove weld; an increase of 15.4 % of the maximum PEEQ index was observed (increased from 9.1 to 10.5). In sum, the larger tapered

flange reinforced zone  $L_{w1}$  results in lower plastic strain demand at the WAH region.

### 3.3.4 Effect of tapered flange extension $L_{ext}$

Three different lengths of a tapered flange extension,  $0.25 d_b$ ,  $0.5 d_b$  and no extension part, were used for prospecting the influence of the splice, at the joint of the column-tree and the link beam, on the tapered flange connection. The distributions of PEEQ index across the beam flange at the tip of the WAH are presented in Figure 3.8. The largest value of the PEEQ index occurred at the root of the WAH (pointed at Figure 3.8) for the model without the extension part because the vicinity of the tapered zone also had high deformation demand. Nevertheless, a reduction of 38.9% in the PEEQ index of the model with  $L_{ext}=0.5 d_b$  was observed at the same location. It is expected that larger flange extension  $L_{ext}$  can ensure higher safety capacity at the interface of the column-tree and the link beam.



### 3.3.5 Plastification of tapered flange connection

Figure 3.9 and Figure 3.10 present the contours of the longitudinal plastic strain and the plastic equivalent strain at a story drift of 4% rad, respectively, to clarify the spread of the plasticity around the connection. Remarkably, the tapered flange connection demonstrated extensive plastification and significant yielding beyond the tapered region, whereas the localized plastic hinge formation took place close to the beam-to-column interface was observed in the pre-Kobe connection. Based on these observations shown in figures, indeed, tapering part of the flange plate following the seismic moment demand conducted to the formation of the extensive plasticity in the beam section away from the column face.



## Chapter 4. Full-Scale Connection Tests

### 4.1 General

The analytical program in Chapter 3 presented the investigation concerning the connections with different configurations of the tapered flange. However, such analyses have some limitations such as residual stresses and HAZ problems in beams that cannot be modeled perfectly. Seven full-scale exterior beam-to-column connections were, therefore, designed and tested to clarify the cyclic behavior and failure modes of tapered flange connections.

### 4.2 Design of Test Specimens

The designs of all specimens followed the current AISC specification (2005b) and the Taiwanese seismic code. The specimens had identical sections of the beam and the column to eliminate the influence of the member size on the connection behavior. The beam and the column were ASTM A572 Grade 50 H-shaped H700×300×13×24 (mm) and box □550×550×28×28 (mm) sections, respectively. Table 4.1 presents the mechanical properties of the steel used for specimens, which were obtained from tensile coupon tests. The CJP groove welds between the column flange and the beam flanges for all specimens were done by the gas metal arc welding (GMAW) process, using an electrode of ER70S-G filler metal.

Table 4.2 tabulated the design parameters of the specimens. Tests began with a specimen with a traditional pre-Kobe moment connection, to examine the performance of the welded column-beam connection. Figure 4.1 depicts the connection details of specimen PK. Specimens W1-L05, W1-L03, W2-L03 and W3-L03 were constructed

following pre-Kobe design practice, whereas various beam web attachment details were designed for specimens B1-L03 and B2-L03 to reflect pre-Northridge design practice. In the labeling of the specimens, the first character, W, presents fillet welded beam web and the second character, B, represents bolted shear tab. Specimen fabrications in Series W and Series B are described in following two sections in detail.

### Specimens of Series W

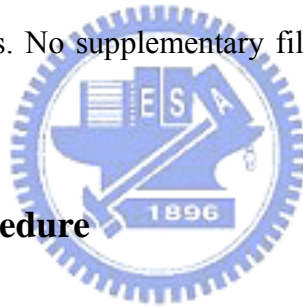
Figure 4.2 illustrates the details of the tapered flange specimens of Series W. Specimens' designation with W1, W2, and W3 indicates  $\beta_j=1.20, 1.10,$  and  $1.05,$  respectively, which results in a different width of beam flange at the beam-to-column interface. Especially, the narrower flange enlargement of specimen W3-L03 was conducted to represent a more critical state. To clarify the plastic deformation capacity, the lengths of the tapered flange  $L_{tap}$  were set to  $0.3 d_b$  and  $0.5 d_b$ , and the corresponding specimens were designated as "L03" and "L05", respectively. The tapered beam flanges were fabricated by a thermal cutting process from a steel plate, to avoid crack initiation in the fusion zone of the groove welds between the wing plates and the beam flanges (Chen et al. 2004). It is noted that the splice between the stub beam and the link beam was fully welded in the laboratory to prevent the slippage effect of the bolted splice.

The width/thickness ratios  $b_f / 2t_f$  of tapered flanges are checked for compacted sections used for beams in a SMF. The maximum  $b_f / 2t_f$  ratio of the beam flange in the tapered zone is 7.2, which is less than the limiting value  $\lambda_p$  ( $=171 / \sqrt{F_y(\text{MPa})} = 65 / \sqrt{F_y(\text{ksi})} = 8.9$ ) of the AISC specification (2005b) for compression members,

being capable of achieving the large plastic strain without local buckling occurred.

### **Specimens of Series B**

The geometry and size of the tapered flange in specimens B1-L03 and B2-L03 are the same as those in specimens W1-L03 and W2-L03 except the beam web attachment. Figure 4.3 shows the specimen configurations of Series B that the beam was connected to the column with the web-bolted flange-welded connection. A short piece of tapered flange beam was built up in the shop and was further spliced to the remaining beam to make one piece of the beam. Afterward a shear tab and beam flange groove welds were used to connect the beam and column together: the CJP groove welds were connected the beam flange to the column flange; the beam web was connected to the shear tab by F10T M24 high-strength bolts. No supplementary fillet weld was placed around the edges of the shear tab.



### **4.3 Test Setup and Procedure**

Tests were conducted in structural laboratory of the National Chiao Tung University. Figure 4.4 illustrates the test setup which simulated the seismic condition of a connection subassembly in a moment frame. A hydraulic actuator, which has the capacity of the maximum load of 980 kN and stroke of 400 mm, was used to proceed this cyclic routine.

As shown Figure 4.5, a cyclic predetermined loading sequence with augmented displacement amplitudes specified in the AISC seismic provisions (2005a) was used during the tests. The test history began with six cycles of  $\pm 0.375$ ,  $\pm 0.5$ , and  $\pm 0.75\%$  rad story drift angle. Subsequently, four cycles of  $\pm 1\%$  rad story drift angle and two cycles with amplitudes of over  $\pm 1.5\%$  rad story drift angle were succeeded

until either the specimens failed or the excursion limitation of the test equipment was reached. It should be noted that the story drift angle is calculated by dividing the beam tip displacement by the distance from the beam tip to the column centerline, as shown in Figure 4.6.

## **4.4 Observed Behavior of Test Specimens**

### **4.4.1 Specimen PK**

Specimen PK was a typical pre-Kobe column-tree moment connection. Flaking of the whitewash originated from the sides of the beam flanges near the groove welds during a story drift of 0.5% rad, and significantly concentrated on this location at the following cycles. This clearly evidences that the beam flange close to the column face develops high local strain concentration, as observed in the finite element analysis. Afterward the slight cracks were noticed in the fusion zone of the borders of the CJP groove weld at the cycles of 3% rad story drift angle. Eventually, specimen PK failed during the negative excursion of the first 4% rad cycle because of a brittle flange fracture, which initiated at the root of WAH cut on the inside of the beam flange surface, as presented in Figure 4.7.

### **4.4.2 Specimens of Series W**

Excluding specimen W3-L03, the failure mechanisms of all tapered flange specimens were almost identical regardless of the various configurations of the flange enlargement, as listed in Table 4.3. All of four specimens exhibited approximately linear behavior before a story drift angle of 0.75% rad because slight powdering of the whitewash was observed in these states. During the cycles of 1% rad story drift angle, the whitewash was noticed on the beam flanges within the tapered part and near the CJP

groove welds. The following cycles of 1.5% rad story drift angle caused flaking further expanding into the tapered flange extension. After that, the whitewash began to spread in the beam web at the 2% rad cycles. Evidenced by the excessive flaking of the whitewash, the overall beam tapered flanges and the beam web developed striking inelastic behavior during the cycles of 3% rad story drift angle. Unexpectedly, minor cracks, either at the sides of beam flange groove welds or at the root of WAH, were observed during the 3% rad cycles of specimen W3-L03; however, no cracking occurred in the other specimens at the same cycle. The sign of cracks apparently revealed that the specimen W3-L03, with  $\beta_j = 1.05$ , provided very margin of the reinforcement at the beam-to-column joint. Afterward, sustained crack propagation led to the fracture of the beam bottom flange, starting at the fusion area of the groove weld as shown in Figure 4.8, during the positive excursion of the second 4% rad cycle.

The ultimate strength of the specimens was achieved during the cycles of 4% rad story drift angle, which simultaneously accompanied slight crack initiation from the end of the built-up weld fusion line between the beam flange and web at the root of WAH. Excessive local buckling of the beam section, developed at approximately ranged from one-half to three-quarter the beam depth from the column face, resulted in gradual deterioration of the strength during the following cycles of 5% rad story drift angle. Figure 4.9 shows local buckling of the beam flange and the beam web of specimens W1-L05 and W1-L03 at a story drift angle of 5% rad. Test was terminated at a story drift angle of 5% rad because of the excursion limitation of the actuator. To sum up, for the properly designed specimens, the plastic hinge formation of the beam was expectably spread around the tapered flange, developing the satisfactory plastic rotation of the connection.

#### **4.4.3 Specimens of Series B**

Both specimens performed the same patterns of global behavior with each cycles until at 3% rad story drift angle. The flaking of the whitewash was noticed on the tips of the shear tab near the WAH, accompanied a metallic grating noise caused by the shear tab slippage. During 4% rad story drift angle, the ultimate resisting force of the connection was reached while minor cracking was observed at the root of WAH, as shown in Figure 4.10. At the same time, the progressive augmented buckling of the beam section, stemming from the tapered part of the beam flange, caused strength degradation in specimen capacity during subsequent cycles. Figure 4.11 exhibits the yielding and local buckling patterns of specimens B1-L03 and B2-L03 during 5% rad story drift angle. The presence of the shear tab not only assisted in forming the plastic deformation in the beam away from the column face but also resisted the occurrence of the severe web local buckling. Finally, testing was stopped at 5% rad story drift angle due to the displacement limit of the test apparatus. No weld fracture was observed in the specimens except a small crack, which was located in the HAZ at the edges of the beam top flange, at the end of the test of specimen B2-L03.

#### **4.5 Test Results and Discussion**

Test results of the specimens are inspected for the hysteretic response, the failure modes, the connection moment capacity, the envelope response, and energy dissipation. Table 4.3 tabulates the test results of the specimens.

##### **4.5.1 Hysteretic response and failure modes**

###### **Specimen PK**

Figure 4.12 presents the hysteresis relationships of specimen PK in terms of both the story drift angle and the total plastic rotation. Herein, the test moment was calculated by multiplying the beam tip load by the distance from the free end of the cantilever beam to the box column face, and this moment was normalized by the plastic moment capacity of the stub beam based on the measured material strengths. The maximum total plastic rotation of specimen PK was 2.6% rad, which the total plastic rotation was determined by subtracting the elastic rotation from the total angle of rotation. The failure was caused by the fracture of the beam flange initiated at the junction of WAH and the beam flange groove weld. Although the ductility of this specimen was improved, compared to the pre-Northridge specimens tested by Chen et al. (2004), using column-tree design practice in the connection has insignificant effect on the prevention of the beam flange fracture originated from the WAH region.

### **Specimens of Series W**



The hysteresis responses of the normalized moment to the story drift angle and the total plastic rotation for the all column-tree tapered flange specimens are presented in Figure 4.13. As summarized in Table 4.3, specimens W1-L05, W1-L03, and W2-L03 developed approximately 4% rad of maximum total plastic rotation, which contributed mainly from the inelastic deformation of the beam. The beam plastic rotation was determined by subtracting the plastic rotations of the column and the panel zone from the total plastic rotation of the connection. The primary failure mode of these specimens was the significant local buckling of the beam flanges and web, which was followed by the degradation of connection strength, during the cycles of 5% rad story drift angle. The post-peak strength capacity of specimens W1-L05, W1-L03, and W2-L03 were reduced by 15.6% (an average of +13.5% and -17.6%), 17.3% (an

average of +18.8% and -15.8%), and 17.1% (an average of +16.8% and -17.4%), respectively, compared to those at the 4% rad cycles, where '+' represents the positive excursion cycle and '-' represents the negative excursion cycle.

As shown in Figure 4.13(a), specimen W3-L03 failed in a brittle mode caused by the fracturing of the beam bottom flange during the cycles of 4% story drift angle. After that, the negative excursion of monotonic loading was applied to identify the failure mode in the beam top flange. In the end, not only local buckling of the beam bottom flange was noticed within the tapered zone of the beam flange, but also notable cracks either at the root of WAH or at the both sides of the beam flange groove welds were observed at the end of the testing.

### **Specimens of Series B**

The cyclic behavior of the specimens B1-L03 and B2-L03 behaved much like those column-tree connections regardless of their various connection details. A graph of the hysteresis relationships for specimens B1-L03 and B2-L03 is shown in Figure 4.14. Both specimens developed reliable inelastic behavior with a maximum story drift angle of 5% rad, absorbing a remarkable amount of the energy. The final failure was owing to striking local buckling at the beam flanges and web, and accompanied gradual deterioration in the flexural strength of the connection. However, the strength still exceeded the plastic flexural strength of the beam. In brief, the pre-Northridge specimens improved by the tapered flange behaved excellent ductile performance, although the extra cost for fabricating such built-up tapered flange connection is relatively high, compared to those typical web-bolted flange-welded moment connection.



#### 4.5.2 Connection moment capacity and envelope response

In general, high levels of localized inelastic deformation with strain-hardening behavior would result in premature local buckling. However, using a uniform yielding zone to average the local strain demand may delay local buckling occurred. Figure 4.15 illustrates the ratios of the maximum test moment to calculated plastic moment capacity of the specimens along the horizontal direction of the beam length. This ratio represents the strain-hardening level of the beam section. It can be noticed that the tapered flange had provided a flattop level of larger uniform inelastic deformation in the beam away from the column face and stressed the tapered zone of the beam into 1.15 times of the plastic moment capacity. Specimen W1-L03 with  $\beta_j=1.2$  give the more conservative design at the column face than specimen W2-L03 with  $\beta_j=1.1$ . Consequently, the moment demand at the beam-to-column joint is reduced intentionally with the introduction of the flange enlargement, compared to the pre-Kobe connection specimen PK.

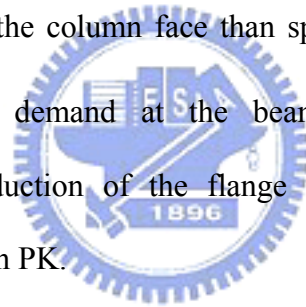


Figure 4.16 shows the hysteretic envelopes relationship for the all six tapered flange specimens. As demonstrated in this figure, the global behavior of the connection subassembly, either strength capacity deterioration or local buckling occasion, was also very similar. It was found that local buckling of the beam section in each specimen did not commence until the 4% story drift cycle.

#### 4.5.3 Energy dissipation

Figure 4.17 compares energy dissipation of specimens to confirm the effectiveness of the tapered flange. Specimen PK dissipated a smallest amount of energy because of a brittle fracture of the beam flange occurred at a story drift angle of

4% rad. On the contrary, the successful tapered flange specimens dissipated a higher amount of energy about 2.4 times than that of specimen PK, due to the stable and full hysteretic loops of the specimens. A comparison of specimen W1-L03 with W1-L05 indicates very similar energy dissipation for the two test specimens. Increasing the length of the tapered flange from  $0.3 d_b$  to  $0.5 d_b$  has a slight effect on the connection behavior. Furthermore, although different connection details of the beam web attachment were used, each tapered flange specimen also dissipated a similar amount of energy. This clearly shows that the ductility of the specimens, either the tapered flange column-tree connection or the web-bolted flange-welded connection, can significantly improve by the application of the tapered flange.



## **Chapter 5. Evaluation of Analytical and Experimental Response**

### **5.1 General**

In general, the yield of a specimen can superficially judge by flaking of the whitewash on the surface of the test specimen. It is common to use the numerical simulation to comprehend the progressive growth of the yielding and plastification in the specimen. This chapter presents a detailed evaluation of numerical and experimental response of the tapered flange specimen and force transfer mechanism within the connection region.

### **5.2 Evaluation of tapered flange connection subassembly**

Numerical simulations of the tapered flange specimen were compared with the experimental results for both global and local responses to evaluate the accuracy of the finite element modeling. Only specimen W1-L03 was used for numerical simulation because all the tapered flange specimens performed the similar connection behavior. In the numerical simulation, the measured material properties of the beam and column listed in Table 4.1 were used. Furthermore, the kinematic hardening behavior of the structural steel was assumed for cyclic analyses.

#### **5.2.1 Global response**

Global behavior of tapered flange connection subassembly is presented in terms of the hysteretic loops. Figure 5.1 presents the numerical hysteresis curves of the beam tip load versus the corresponding displacement for specimen W1-L03, with the experimental curves superimposed. A close examination of the figure showed that the

predicted stiffness and the ultimate load at each cycles well matched those of the test specimen up to a story drift angle of 4% rad. However, the predicted responses during the unloading status were somewhat wider than the experimental ones, possibly because the bilinear strain-hardening behavior of material was applied in the analysis. Overall, the global load-displacement hysteretic response demonstrates good correlation between the numerical and the experimental work.

### 5.2.2 Local response

Strains recorded during the testing were examined to clarify the local behavior of the specimens. Accordingly, four critical lines running across the beam flange are selected as the concerned location. Figure 5.2 presents these strain gauge locations: Line F40 is located at a distance of 40 mm from the column face, to evaluate the potential of flange fracture at the CJP groove welds; Lines TF1, TF2 and TF3 are located at a distance of 200 mm (at the end of the tapered zone), 305 mm (at the middle of the tapered zone) and 410 mm (at the beginning of the tapered zone) from the column face, subsequently, to examine the force transfer within the tapered part of the beam flange.

The local behavior was examined by comparing the predicted strains with test data at various loading steps. Figure 5.3 shows the normalized longitudinal strain distributions on the beam flange at line F40 between the story drift angles of 0.5% and 4% rad. Each strain is normalized by a measured yield strain  $\varepsilon_y$  of the beam flange material in the stub beam. Because residual stresses and HAZ problems were not considered in the analysis, the predicted strains in the vicinity the beam flange groove weld were lower than the test strains. Figure 5.4 presents both the predicted and

measured strains across the beam flange within the tapered zone until 4% rad story drift angle. The elastic response of the test specimen can be precisely simulated, as well as the inelastic response envelope of the numerical results shows the same trend as test data. A reasonable agreement between the numerical results and the experimental tests was generally achieved. Based on the satisfactory performance, this finite element model was then used to better understand states of stress and strain in the moment connection with a tapered flange.

### **5.3 Stress and strain distribution in connection**

The numerical investigation comprehended the von Mises stress distribution, the equivalent plastic strain distribution, and the transference of the beam forces. In addition, the measured strains in the test specimens were also presented in this section to verify the effectiveness of the proposed tapered flange.

#### **5.3.1 Distributions of von Mises stress and equivalent plastic strain**

As indicated by previously works (Popov et al. 1998; El-Tawil et al. 2000; Mao et al. 2001; Chen et al. 2003; Kim et al. 2004; Chen et al. 2005a; Chen et al. 2005b), von Mises stress and equivalent plastic strain were utilized as an indicator of the potential for plasticity, when considering ductile materials. Accordingly, herein the results of the simulation are plotted in the form of such stress and strain distributions to elucidate the connection behavior. A story drift angle of 1% rad was chosen to represent the beginning of the inelastic stage, because specimen W1-L03 performed in elastic behavior before the 0.75% rad cycles. Furthermore, a story drift angle of 4% rad was used to elucidate the connection performance under higher levels of strained states, because ultimate capacity of specimen W1-L03 was achieved at this drift level.

Figure 5.5(a)-(d) shows the progressive contours of the von Mises stress and the equivalent plastic strain for the finite element model of specimen W1-L03 at 1, 2, 3 and 4% rad story drift angles. Notably, yielding of the beam occurred initially at the sides of the beam flange near the groove weld during 1% rad story drift angle. After that, distinct yielding in the tapered zone of the beam flange shown in Figure 5.5(b) was noticed. During a story drift angle of 3% rad, the extensive yielding zone strikingly expanded into the entire beam tapered flange and the nearby flange extension. Note that the equivalent plastic strains in the yielding zone are approximately 9.7 times the yielding strain. Afterward, an appreciable amount of yielding spread toward the middle part of the flange enlargement near the WAH region, as shown in Figure 5.5(d). Such highly stressed and strained states could lead to premature crack initiation at the root of the WAH, as evidenced by the full-scale testing.

According to above figures, notably, these observations indicate that the moment connection with a tapered flange forms extensive yielding and plastification in the beam section away from the beam-to-column interface. An enlarged plastic zone, with uniform plastic strains, can be obtained in not only the tapered zone of the beam flange but also the flange extension.

### **5.3.2 Force transfer in beam**

Traditionally, the design of moment connections is assumed following classical beam theory. Using this simplification approach, shear force is primarily resisted by the beam web while bending moment is resisted by the entire beam section. No interaction of shear and moment is supposed. However, the application of such traditionally designed approach at beam-to-column joints leads to drastic variations because of the effect of boundary conditions imposed by the column. Remarkable amounts of shear

force are transferred across the connection through the beam flanges that has been documented in the literature (Goel et al. 1997; Goel et al. 2000). With the interaction of shear force and flexural moment in the vicinity of the joint, accordingly, the predictions of force transfer from the beam flanges to the column could be underestimated.

The delivery of beam forces to the column is presented in the forms of the normalized shear stress and the normalized longitudinal stress. The shear stress,  $\tau$ , is normalized by the shear yield stress,  $\tau_y$ , which is defined as

$$\tau_y = \frac{F_y}{\sqrt{3}} \quad (5.1)$$

where  $F_y$  is the yield stress of the beam material. Also, the longitudinal stress,  $\sigma_{11}$ , represented the normal stress is normalized by the yield stress.

#### **At elastic response**

Figures 5.6 and 5.7 shows the distributions of the normalized shear stress along the depth of the beam web and the width of the beam flange, respectively, in four different sections during a story drift angle of 0.5% rad. Note that such stress data are captured from a transverse line through the one-half thickness of the beam flange (or the beam web). For tapered flange moment connections, it is clear from Figure 5.6 that symmetrically uniform shear stress profiles are found at the adjacent regions of the tapered zone and the splice joint. Nevertheless, the inverse parabolic stress distribution is found at a cross section 20 mm away from the column face, due to the influence of boundary restraint provided by the column flange. Evidently, the force transfer in the connection may not follow the beam theory, especially at the critical section near the face of the column, because a significantly greater part of the beam shear force is

transferred through the beam flanges, as shown in Figure 5.7.

Figures 5.8 and 5.9 shows the normalized longitudinal stress profiles along the beam web and beam flange at 0.5% rad story drift angle. The presence of the WAHs between the column-tree and the link beam created localized stress concentration on the sides of the beam web at the splice joint (see Figure 5.8). In the meantime, the similar concentration behaviors shown in Figure 5.9 at either the beam flange groove weld or the end of the tapered zone were observed. The reason for such stress flow is primarily attributed to the stiffness of the column web on both sides, as presented in the previous analyses (Roeder 2000; Chen et al. 2004; Kim et al. 2004).

#### **At ultimate response**

On the basis of the experimental results, 4% rad story drift angle was considered to represent the ultimate status of the analytical model. The normalized shear stress distributions shown in Figure 5.10 demonstrated 35% of the reverse shear force in the middle of the beam web at a cross section 20 mm away from the column face, while the constant shear flow was noticed in other cross sections. Similar analytical results were observed by Lee (2002). Figure 5.11 plots the resulting normalized shear stress profiles along the beam flange width at a story drift angle of 4% rad. The beam flanges took the majority of the beam shear in both the elastic and inelastic state, when connecting to the face of the column.

The distributions of the normalized longitudinal stress transferred through the beam web and beam flange to the column flange is presented in Figures 5.12 and 5.13, respectively. Larger yielding of the beam web in the beam tapered zone was found during 4% rad story drift angle, whereas the other cross sections, located at either the



vicinity of the beam-to-column connection or the splice joint, were performed in elastic behavior. As plotted in Figure 5.12, only slight yielding was observed at the edges of the beam web near the flange-web junction. It is evident from Figure 5.13 that the entire stub beam attains a yielding moment,  $M_y$ , with highly uniform longitudinal stresses (averagely 1.2 times yield stress) developed in the tapered zone of the beam flange.

### **Percentage of shear force in beam**

By integrating the shear stresses shown in Figures 5.6 and 5.10 with the area of the beam web, the beam shear in the beam web at each cross section can be calculated. The shear force transferred by the beam flanges, in addition, was obtained by subtracting the beam web shear from the applied beam tip load in each case. Table 5.1 tabulates the percentage of the beam shear in the tapered flange connection with increasing the distance from the column face at story drift angles of 0.5 and 4% rad. Much of the shear force transferred through the beam flanges in the vicinity of the joint extremely disobeyed assumptions of the beam theory. However, with increasing the distance (approximately 0.3 times beam depth) away from the column face, the distribution of the shear force in the beam section commenced following the beam theory in either the elastic (0.5% drift) or the inelastic (4% drift) range. Therefore, when designing a splice joint between the column-tree and the link beam, it is reasonable to assume that the beam web takes the entire beam shear.

### **5.3.3 Strain response around connection**

The proposed moment connection has two important improvements. First, enlarging the beam flanges near the column face functions as a reinforcement to prevent fracture at the CJP groove welds. Second, tapering a portion of the beam

flanges following the seismic moment gradient forms an enlarged uniform yielding zone to augment more sufficient ductility in the connection. Consequently, to verify the design idea of the proposed connection, the strain states recorded in strain gauges attached on the test specimens at these locations had to be examined.

Figure 5.14 shows the normalized measured longitudinal strain distributions at line F40 between specimens PK and W1-L03. From this figure, it can be seen that the strains of specimen PK are several times larger than those of specimen W1-L03, with an opposite strain trend. The maximum normalized longitudinal strain for specimen PK is 45 at the border of beam flange (during 3% drift), whereas the maximum normalized longitudinal strain for specimen W1-L03 is 20 at the middle of beam flange (during 4% drift). This outcome clearly evidences that the enlarged beam flange effectively assists in lowering strain levels near the CJP groove welds. Fracture of the beam flange in the region of the WAH could be avoided with the flange enlargement.

The distributions of the normalized longitudinal strains across the tapered zone of the beam flange for the column-tree specimens are shown in Figure 5.15. It is found that both the elastic and inelastic responses of the strains in each specimen were almost similar. Such strains were equally increased and averaged about 9.9 times of the yield strain at a story drift angle of 4% rad. The strain trends for specimens B1-L03 and B2-L03 shown in Figure 5.16 also match those in Figure 5.15. However, an average of strains in specimen W3-L03 during 4% rad story drift angle was 7.7 times yield strain, owing to local buckling of the beam section occurred. To sum up, the tapering of the beam flanges provides an enlarge yielding pattern in the beam tapered zone, performing the satisfactory inelastic deformation in the beam.

## Chapter 6. Design Recommendation

### 6.1 General

This chapter presents the design approach of the moment connections with a tapered flange. The foundations for the design of the tapered flange connections are based on the results of the parametric study in Chapter 3 and the full-scale tests in Chapter 4. A step-by-step example for designing the tapered flange is also presented in Appendix A to express the design procedure more clearly and systematically.

### 6.2 Design Procedure

As demonstrated from the results of the experiment and finite element analysis, tapered flange connections exhibited excellent advantages of seismic performance for SMFs. Design procedure for the tapered flange connection, on the basis of the capacity design concept, is provided and describes as follows.

The expected plastic flexural capacity of the beam,  $M_{pr}$ , i.e. at the beginning of the tapered zone of the flange enlargement, is first calculated as

$$M_{pr} = C_{pr} R_y F_y Z_b \quad (6.1)$$

where  $C_{pr}$  represents a factor accounted for strain-hardening behavior,  $C_{pr}$  equal to 1.2 may be used for most connection types as recommended in FEMA-350 (2000);  $R_y$  is an adjustment factor of expected material overstrength;  $F_y$  denotes the nominal yield strength of the beam material; and  $Z_b$  represents the plastic section modulus of the beam.

Second, design the width of the beam flange at the end of the tapered part,  $b_{f,tap}$ .

For design purposes, the uniform plastic deformation capacity is assumed to develop simultaneously at the tapered zone. Hence, the design flexural capacity at the end of the tapered flange,  $M_{p,tap}$ , can be determined from the moment gradient diagram shown in Figure 6.1.

$$M_{p,tap} = \frac{L_b - (L_{w1} + L_{w2})}{L_b - (L_{w1} + L_{w2} + L_{tap})} M_{pr} \quad (6.2)$$

where  $L_b$  is the length of the half clear span of the beam. Based on the results of the experiment and finite element analysis, the design parameters of  $L_{w1} = 0.5b_f$ ,  $L_{w2} = 50$  mm, and  $L_{tap} = 0.3d_b$  can be used for practical purposes, where  $b_f$  is the beam flange width;  $d_b$  is the beam depth. Thus, the required flange width can be calculated by

$$b_{f,tap} = \frac{Z_{b,tap} - Z_{web}}{(d_b - t_f) t_f} \quad (6.3)$$

and

$$Z_{b,tap} = \frac{M_{p,tap}}{C_{pr} R_y F_y} \quad (6.4)$$

where  $Z_{b,tap}$  represents the plastic section modulus of the beam at the end of the tapered zone;  $Z_{web}$  is the plastic section modulus of the beam web; and  $t_f$  is the thickness of the beam flange.

Third, design the width of the flange enlargement at the beam-to-column interface,

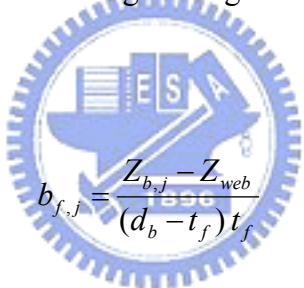
$b_{f,j}$ , by setting the parameter  $\beta_j$  as 1.2 or greater to prevent failure occurring at the beam flange groove weld. Accordingly, the design flexural capacity at this location,  $M_{p,j}$ , can be determined as

$$M_{p,j} = \beta_j M_{dem,j} \quad (6.5)$$

where  $M_{dem,j}$  denotes the moment demand of the beam at the column face, which can be calculated as

$$M_{dem,j} = \frac{L_b M_{pr}}{L_b - (L_{w1} + L_{w2} + L_{tap})} \quad (6.6)$$

Therefore, the required width of the flange enlargement can be calculated by using the equations, as



$$b_{f,j} = \frac{Z_{b,j} - Z_{web}}{(d_b - t_f) t_f} \quad (6.7)$$

and

$$Z_{b,j} = \frac{M_{p,j}}{C_{pr} R_y F_y} \quad (6.8)$$

where  $Z_{b,j}$  represents the plastic section modulus of the beam at the beam-to-column joint.

Fourth, select the appropriate radius of the curved transition of  $R = L_{w1}$  to supply the corners adjacent to the tapered zone with smooth force transferring. In addition, select the tapered flange extension of  $L_{ext}$  at least  $0.5d_b$  or larger for providing

sufficient margin of safety at the stub beam-to-link beam interface.

Final, because the beam flange enlargement increases the flexural strength of the beam, the seismic design requirements for a strong column-weak beam criterion should be checked for designing the tapered flange connection.

$$\frac{\sum M_{pc}}{\sum M_{p,j}} > 1.0 \quad (6.9)$$

where  $M_{pc}$  denotes the sum of the flexural strength in the column above and below the beam-to-column joint.



## **Chapter 7. Inelastic Structural Analysis for SMFs with Tapered Flange Connections**

### **7.1 General**

Inelastic structural analyses for steel SMFs were performed to examine the effects of tapered flange connection on the structural behavior. Two types of steel SMFs were modeled: one was with unreinforced connections (lack of ductility); the other was designed to have tapered flange (TF) connections. Moreover, five- and fifteen-story buildings were designed for each type of SMFs in order to evaluate the effects of different rises of buildings. The design of the tapered flange connection followed the proposed design procedure as described in Chapter 6. The structural analyses composed both linear elastic analysis and nonlinear static pushover analysis by using the computer program SAP2000 (Habibullah and Wilson 2004). The performance of the frames is evaluated in terms of nonlinear pushover behavior as well as plastic hinge distribution under specified seismic levels.

### **7.2 Design of Prototype Buildings**

#### **7.2.1 Prototype building configuration**

Figure 7.1 sketches a typical floor plane of the prototype office building comprised a special moment-resisting structural system with welded built-up box columns and H-shaped beams. The buildings are designed to be symmetric so that vertical and horizontal irregularity is avoided. The building has identical floor plans with four bays by four bays. The bay spacing is 9.5 meters from column centerline to column centerline. Figure 7.2 illustrates the elevation view of the five- and fifteen-story SMFs. First story is 5 meters high and the remaining stories are 3.5 meters.

It is noted that all frames in the prototype buildings are designed to be the primary lateral resisting frames; hence, all beam-to-column connections are moment connections.

The designs of the prototype buildings are in compliance with the AISC-LRFD specifications (1999) and the 1997 Uniform Building Code (UBC 1997). Table 7.1 tabulates the details of the design gravity loads imposed on the prototype buildings. The slab is assumed to have a thickness of 15 centimeters lightweight concrete on a 7.5 centimeters deep metal deck. The floors in each story level use raised floor, except that the roof is assumed to be asphalt paving. Eventually, the dead loads of  $3,532 \text{ N/m}^2$  ( $360 \text{ kgf/m}^2$ ) and  $4,120 \text{ N/m}^2$  ( $420 \text{ kgf/m}^2$ ) are imposed at the roof and floors, respectively. The live loads of  $2,943 \text{ N/m}^2$  ( $300 \text{ kgf/m}^2$ ) and  $3,924 \text{ N/m}^2$  ( $400 \text{ kgf/m}^2$ ) are assumed for office occupancy at the roof and floors, respectively, as listed in Table 7.2. All structural members are made of A572 Grade 50 steel with nominal yield stress of 345 MPa and nominal ultimate stress of 450 MPa.

### **7.2.2 Elastic analysis of prototype buildings**

A general-purpose structural analysis program SAP2000 was used as a tool for performing the linear elastic analysis of the prototype buildings. The assumptions made in the modeling and analyses of the frames are as follows.

1. Only one of the lateral resisting frames in the prototype building is considered. All SMFs investigated in the structural analysis are modeled as two-dimensional frame structures.
2. Beam and column rigid end zones are included and elastic panel zone models are



applied.

3. The lateral displacements of columns at each floor level are constrained together using a diaphragm connected all nodes on the same floor level.
4. Mass is lumped at beam-to-column joints.
5. Rayleigh damping for mass and stiffness is used with 5% viscous damping in the first two modes.
6. Accidental torsion is not considered.

In the linear static analysis, the pseudo lateral earthquake loads should be conducted to respond the typical distribution of inertial forces in the frame structure subjected to the ground shaking excitation. An estimate of the seismic masses of the structure has to be made for purposes of determining the lateral earthquake forces. The masses of 5,101 N/m<sup>2</sup> (520 kgf/m<sup>2</sup>) at the floors and 3,532 N/m<sup>2</sup> (360 kgf/m<sup>2</sup>) at the roof (added up the dead loads from Table 7.1 and the partition load from Table 7.2) are specified only in a horizontal direction of the building. The seismic force specified in the Building Seismic Design Provisions of Taiwan code (內政部營建署 2005), presented in Appendix B, is used to estimate the lateral earthquake loads on the structure.

### **SMFs with unreinforced connections**

In the case of the unreinforced five-story SMF (UR-5F), the approximate fundamental period can be calculated by the experienced equation of  $T_{\text{exp}} = 0.085h_n^{3/4} = 0.085(19)^{3/4} = 0.77$  seconds for steel construction, where  $h_n$  is the

height of the building from the base to the roof level. Meanwhile, the final design of the UR-5F building conduces the computed fundamental period  $T_{comp}$  equal to 1.05 seconds. As a result, the design fundamental period for calculating the seismic force is obtained with  $T = \min(C_U T_{exp}, T_{comp}) = 1.0$  seconds, where  $C_U$  is 1.3 for  $S_{D1} = 0.3$ . This results in the parameter  $S_{aD}$  equal to 0.6. Finally, the seismic base shear,  $V$ , can be obtained using Equation B.1:

$$V = \frac{I}{1.4\alpha_y} \left( \frac{S_{aD}}{F_u} \right)_m W = \frac{1.0}{1.4 \times 1.2} \left( \frac{0.6}{2.19} \right) W = 0.163 W$$

Considering the structural performance of yielding in the low (medium) ground shaking, the design seismic force,  $V^*$ , can be calculated as:

$$V^* = \frac{I F_u}{3.5\alpha_y} \left( \frac{S_{aD}}{F_u} \right)_m W = \frac{1.0 \times 2.19}{3.5 \times 1.2} \left( \frac{0.6}{2.19} \right) W = 0.143 W$$

Considering the structural performance of collapse prevention in MCE hazard level, the design base shear,  $V_M$ , is computed as:

$$V_M = \frac{I}{1.4\alpha_y} \left( \frac{S_{aM}}{F_{uM}} \right)_m W = \frac{1.0}{1.4 \times 1.2} \left( \frac{0.8}{2.93} \right) W = 0.163 W$$

At last, the final design base shear of the building is equal to  $0.163 W$  that is the largest one among  $V$ ,  $V^*$  and  $V_M$ . This seismic force is then applied at each floor level with the vertical distribution consisting with the first mode response. The lateral earthquake load at floor level  $x$ ,  $F_x$ , is determined from the following equation:

$$F_x = \frac{(V - F_t)W_x h_x}{\sum_{i=1}^n W_i h_i} \quad (7.7)$$

and

$$F_t = 0.07TV \quad (7.8)$$

where  $F_t$  indicates concentrated lateral load additionally input at the roof;  $W_x$  and  $W_i$  are the portion of  $W$  assigned to floor level  $x$  or  $i$ ;  $h_x$  and  $h_i$  are the height from the base to floor level  $x$  or  $i$ . The five-story building is designed for an effective seismic weight of 34,565 kN and the design base shear per frame is 1,127 kN. Table 7.3 lists the results of the distribution of seismic forces imposed on the floors of the UR-5F building.

For the unreinforced fifteen-story SMF building (UR-15F), the same design procedure had carried out to design column and beam members. The experienced fundamental period  $T_{exp}$  and the computed fundamental period  $T_{comp}$  are 1.69 and 2.35 seconds, respectively. The design fundamental period of 2.20 seconds is, therefore, employed to calculate the seismic force determined from Equation B.1. The parameters  $S_{aD} = 0.436$  and  $S_{aM} = 0.582$  are respectively calculated from Equation B.3 of  $S_{DS}(T_0^D / T)$  and Equation B.4 of  $S_{MS}(T_0^M / T)$ . Meanwhile, the structural system reduction factor  $F_u$  takes the same 2.9 as the parameter  $R_a$  because the design fundamental period is larger than  $T_0^D = 1.6$  seconds. Based on these parameters, the design base shear of the UR-15F building can be calculated as  $0.104W$  from the maximum value of the following equations:

$$V = \frac{I}{1.4\alpha_y} \left( \frac{S_{aD}}{F_u} \right)_m W = \frac{1.0}{1.4 \times 1.2} \left( \frac{0.436}{2.9} \right) W = 0.09 W$$

$$V^* = \frac{I F_u}{3.5\alpha_y} \left( \frac{S_{aD}}{F_u} \right)_m W = \frac{1.0 \times 2.9}{3.5 \times 1.2} \left( \frac{0.436}{2.9} \right) W = 0.104 W \quad (\text{Control})$$

$$V_M = \frac{I}{1.4\alpha_y} \left( \frac{S_{aM}}{F_{uM}} \right)_m W = \frac{1.0}{1.4 \times 1.2} \left( \frac{0.582}{4.8} \right) W = 0.072 W$$

Consequently, the design base shear per frame for the fifteen-story building is 2,251 kN, correlated with an effective seismic weight of 108,226 kN. The lateral earthquake forces for each floor as applied to the design of the UR-15F building are tabulated in Table 7.3.

The final designs of member sizes for UR-5F and UR-15F are shown in Figure 7.2, respectively. All structural members in the same story level had identical column and beam sizes, controlled by the 1997 UBC story drift limitations. Moreover, strong column-weak beam criterion was also applied to the design of prototype buildings to assure that columns will not develop plastic hinges before beams.

### **SMFs with tapered flange connections**

Table 7.4 tabulates the resulting sizes of tapered flanges used for the TF frames. The TF frames are designated as TF-5F and TF-15F for the five- and fifteen-story frames, respectively. A similar design procedure that used to design the UR frames was also employed to design the TF frames. It should be noted that all beams and columns used in the TF frames have the same member sizes as those used in the UR frames. Since the sizes of beam members have been decided, the dimensions of tapered flange

plates can be designed according to the design recommendation in Chapter 6. Two primary design variables of  $\beta_j$  and  $L_{tap}$  are set to 1.2 and  $0.3d_b$ , respectively, in designing the tapered flange connection.

### 7.3 Nonlinear Static Pushover Analysis

The pushover analysis documented in FEMA-273 (BSSC 1997) has become a standard procedure for seismic performance evaluation of structures. The building models are pushed to some predetermined target displacements those are intended to represent the maximum roof deformation probably to be experienced during the design earthquakes. With this nonlinear static analysis, the possible performance of the structure shall be estimated with either strength or deformation demands at performance levels of interest. Furthermore, failure modes of the structure can be found by means of the monotonically increasing lateral loading.

#### 7.3.1 Frame modeling and validation

The SMFs subjected to a combination of a triangular lateral load and gravity loads are modeled in SAP2000. The details of frame modeling are shown in Figure 7.3. The dead load and half of live load are included in the analyses. P-M interactive effect is particularly used to all column elements, because these members sustain large axial forces. It is also considered that all panel zones of the column behave elastic response. In addition, pushover hinges in all beam elements have to be assigned for performing the pushover analysis of SAP2000.

The definitions of properties for plastic hinges can directly react on the response of the pushover analysis. Because of this, two typical subassembly models shown in

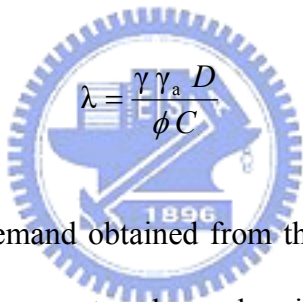
Figure 7.4, designated as UR-C and TF-C, are developed to reflect the performance of moment connections used in the UR and TF frames. The tested response of specimen PK is selected to represent the character of an unreinforced connection, while specimen W1-L03 is picked out to stand for the connection with a tapered flange. Note that plastic hinge on UR-C locates at the beam beyond the rigid end zone, whereas plastic hinge on TF-C is lumped at the tapered zone of the beam as conformed to the location in the test. Figures 7.5 and 7.6 exhibit the plastic hinge properties of models UR-C and TF-C respectively, in which five points labeled A, B, C, D, and E are used to define the moment-rotation relation of the hinge. Specifically, an asymmetric force-deformation behavior is defined for the unreinforced connection to consider the different failure modes of the beam top and bottom flanges. However, the degradation of connection strength resulted from local buckling of beam section is not considered in both models. For simulating a brittle fracture of the connection, it is assumed that UR-C has negligible strength beyond the maximum strength. On the other hand, it is considered that the post-peak strength of TF-C can sustain 20% yield strength. Figure 7.7 shows comparisons between experimentally hysteresis response and numerically monotonic envelope for models UR-C and TF-C. Reasonable correlation between the predictions and the test results was obtained.

Based on these analytical results, 2.5% and 2% strain-hardening ratios of beam members are then used in the UR and TF frames, respectively. All columns use 3% strain-hardening ratio and P-delta effect associated with the gravity system is considered in the analysis. The capacity of the beam-to-column connection is set to 3% rad story drift angle for an unreinforced connection and 5% rad story drift angle for a tapered flange connection. Besides, the span of the beam used in the studied

frame is twice of that used in the subassemblage, hence the value of the specified inelastic rotation should be modified as half that used in the subassemblage to receive the identical connection response.

### 7.3.2 Evaluation methodology

FEMA-350 (2000) provides a performance-based design procedure for seismic performance evaluation of steel SMFs. By estimating a confidence level of the structure under specific performance objectives, the probable seismic performance of the building shall be obtained. This evaluation methodology is used for the frame analysis. The confidence level is determined through the calculation of a confidence parameter,  $\lambda$ , given by the equation:

$$\lambda = \frac{\gamma \gamma_a D}{\phi C} \quad (7.9)$$


where  $D$  is the calculated demand obtained from the structural analysis;  $C$  is the capacity of the structure;  $\gamma$  represents a demand variability factor;  $\gamma_a$  represents an analysis uncertainty factor; and  $\phi$  is a resistance factor that account for uncertainty and variation inherent in the structural capacity. These uncertainty parameters based on the probabilistic basis were determined by Cornell et al. (2002) and Yun et al. (2002).

The values of the parameter  $\lambda$  are dependent on the character of the site-specified probabilistic earthquake hazard. For the building located in Taipei basin, the hazard parameter,  $k$ , shall be modified and calculated as follows:

$$k = \frac{\ln\left(\frac{H_{S_{1(10/50)}}}{H_{S_{1(2/50)}}}\right)}{\ln\left(\frac{S_{1(2/50)}}{S_{1(10/50)}}\right)} = \frac{1.65}{\ln\left(\frac{0.5g}{0.35g}\right)} = \frac{1.65}{0.357} = 4.62$$

where  $k$  is the slope of the hazard curve at the hazard level of interest and  $S_{1(2/50)}$  and  $S_{1(10/50)}$  represent the spectral amplitude for 2% and 10% probabilities of exceedance in 50 years, respectively. Accordingly, the approximately values of  $\lambda$  can be obtained from Table 7.5 and adopted in the following performance evaluation procedure.

### 7.3.3 Discussion of analytical results

Two structural performance levels, Immediate Occupancy (IO) and Collapse Prevention (CP), are used for evaluating the seismic behavior of the studied frames. As defined in FEMA-350 (2000), the performance levels of IO and CP represent the performance for earthquake hazards with 50% and 2% probabilities of occurrence in 50 years, respectively. The target displacements for specified earthquake hazards are estimated using the procedures described in FEMA-273 (1997). The corresponding IO and CP target roof drifts (defined as the target displacement over the frame height) are 0.83% and 3.22% rad for the five-story frames, and 0.85% and 2.5% rad for the fifteen-story frames, respectively.

#### Nonlinear performance of five-story frames

Figure 7.8 shows the pushover results of normalized base shear versus roof drift for the five-story frames, in which the base shear is normalized by the effective seismic weight of the frame. With introducing the tapered flange connections in the frame, the



initial stiffness of TF-5F is 4% greater than that of UR-5F. The post-yielding strength of TF-5F is average 4% greater than that of UR-5F. In addition, according to this figure, TF-5F can perform a stable post-yielding behavior up to 4.2% rad roof drift, whereas UR-5F subjects the abrupt strength degradation at 2.1% rad roof drift. To identify this failure mode, the plastic deformation distribution during 2.1% rad drift level was illustrated in Figure 7.9. As indicated in Figure 7.9, most of plastic hinges formed between the first floor and the third floor and one exterior connection at the first floor failed. Both frames formed a similar plastic mechanism at the performance level of IO. Figure 7.10 indicates the formation of the plastic hinges for UR-5F and TF-5F at the roof drift of 3.22% rad (i.e. at the CP performance level). The significant damage on the connections of UR-5F caused 17% reduction from its maximum strength.

### **Nonlinear performance of fifteen-story frames**

The results of the pushover analyses for the fifteen-story frames are illustrated in Figure 7.11. TF-15F has 5.2% increase of the initial stiffness and 3.5% increase of the post-yielding strength from UR-15F. It is clear that for UR-15F significant degradation of frame strength (29.6% reduction in ultimate strength) is observed during 1.5% rad roof drift. Figure 7.12 shows the distribution of plastic hinges of UR-15F at the roof drift of 1.5% rad. It indicates that many damaged connections, concentrated at lower stories of frame between the second floor and the fourth floor, result in notable changes in the story drift angle of each floor, as shown in Figure 7.13. With the introduction of these damaged connections, the maximum story drift angle at the weakest floor was respectably increased from 2.5% to 3% rad.

Figures 7.14 to 7.15 show the distribution of plastic hinges for the fifteen-story frames at the IO performance level. During 0.85% rad roof drift, plastic hinges with

minor rotation distributed between the second floor and the seventh floor for both UR-15F and TF-15F. However, only TF-15F can sustain such high plastic deformation demand until 2.7% rad roof drift. Figure 7.16 show the distribution of plastic hinges for TF-15F at 2.5% rad roof drift, with many ductile connections between the first floor and the fifth floor experiencing the plastic rotation larger than 3% rad. During the CP performance level of UR-15F, a large number of damaged connections located within the low rise of the frame, especially between the first floor and the sixth floor as illustrated in Figure 7.17, resulted in the striking degradation of frame strength (75% reduction in ultimate strength) below the design base shear. The strength degradation of TF-15F is observed during the roof drift of 2.7% rad, because the localized story drift demand exceeded the predefined connection capacity of 5% rad story drift angle. Figure 7.18 indicates the distribution of plastic hinges for TF-15F at this roof drift.

### **Confidence levels of studied frames**

Table 7.6 tabulates the results of performance evaluation for the five- and fifteen-story frames. Figure 7.19 illustrates the structural demands used in the analytical procedure at the IO and CP performance levels. For the five-story frames, TF-5F provides the sufficient confidence levels for hazards with 2% and 50% probabilities of exceedance in 50 years. However, UR-5F has the unsatisfied confidence levels of only 13% for the local collapse performance. For the fifteen-story frames, the acceptable confidence levels for TF-15F are observed for the global and local performance for each hazard level. The frame with UR connections has only 67% and 1% confidence levels for the global and local collapse performance, respectively. This is because the fracture of the beam-to-column connections increases the demand of the UR frame. To sum up, the presence of tapered flange connections

abounds in the expected ductility of SMFs and suspends critically structural damage caused by the connection failure. The buildings constructed with UR connections demonstrate the poor confidence levels for satisfying the IO and CP performance levels.



## Chapter 8. Summary and Conclusions

### 8.1 Summary

Column-tree buildings with welded built-up box columns are one of a popular choice of structural systems used for steel special moment frames (SMFs) in Taiwan and Japan. The schemes of column-tree construction result in those critical welding of beam-to-column joints fabricated in the shop where it is believed to have better quality control than the field welding. Nevertheless, a number of column-tree connections failed during the 1995 Kobe earthquake. To achieve the desired ductility of the column-tree moment connection, this research developed a new type of a tapered flange connection for column-tree SMFs and particularly evaluated their performance through numerical and experimental investigations.

The approach of the tapered flange connection is intended to develop an enlarge plastification in the beam to improve the ductility of the moment connection. It can achieve by tapering portions of beam flanges according to the seismic moment gradient. A series of seventeen finite element models was designed and selected for parametric evaluations. The cyclic behavior of seven specimens was examined through full-scale subassemblage tests. Tests began with a specimen with a pre-Kobe column-tree connection, and followed six tapered flange connection specimens, using the different web attachment details to reflect applications of the pre-Kobe and pre-Northridge design practice. A cyclic predetermined displacement history was applied at the tip of the beam following the prequalification test procedure in AISC. Good observed performance of these tapered flange connections was found. A design procedure, therefore, was proposed based on the results of the analytical and experimental studies.

Analytical evaluations of five and fifteen-story SMFs with tapered flange connections were conducted. Not only linear elastic but also nonlinear pushover analyses were conducted with the objective of providing a simple performance evaluation of tapered flange frames.

## 8.2 Conclusions

The main objectives of this research are to identify and clarify the design variables of a tapered flange, to investigate the behavior of the connection under cyclic loading, and to provide design recommendations for tapered flange moment connections. The following summarizes the major observations and findings in this dissertation:

### Performance of pre-Kobe connection

1. Localized principle stresses and plastic equivalent strains, concentrated at either the tips of the beam flange groove welds or the root of the WAH, were noticed in a finite element model of the pre-Kobe connection. This observation can be attributed to the cross section of the column and the geometry of the WAH configuration, respectively. The potential for crack initiation at these locations are very high, probably causing the beam flange to fracture.
2. The WAHs significantly affect the ductility of a connection. Test of the pre-Kobe connection specimen demonstrated appropriate ductile behavior of 2.6% rad plastic rotation but failed in brittle flange fracture at a story drift angle of 4% rad. Cracks were observed in the fusion zone of the sides of the beam flange groove weld during the 3% rad cycles; the other crack initiated in the toe of the WAH during the 4% rad cycles. The primary account dominating the failure of this specimen is the presence of the WAHs in the beam web. Using column-tree

design practice in the connection has little effect on the prevention of the flange fracture originated from the WAH region.

### **Effects of tapered flange geometry**

1. The behavior of a tapered flange connection is mainly influenced by the length of a tapered zone in the beam and a flange reinforcement ratio at the beam-to-column interface, along with the length of a main tapered flange enlargement and tapered flange extension.
2. Results of the analytical parametric study revealed the following: (1) higher flange reinforcement increases the capacity of the CJP groove welds and results in higher margin of safety at the beam-to-column joint; (2) the larger tapered zone of the beam flange causes lower plastic strain demand at the CJP welds and the WAH region; and (3) using the larger tapered flange enlargement can move away the plastic deformation from the column face.

### **Performance of tapered flange connections**

1. Analytical examinations of the tapered flange connection exhibited extensive plastification spread around the tapered region of the beam away from the column face.
2. Experimental investigations demonstrated that only one of total six tapered flange connections (specimen W3-L03) took place unexpected crack initiation and propagation starting at the fusion zone of the CJP groove weld. No weld fracture was observed in all of other test specimens. This indicates that using the adequate width of the tapered flange at the beam-to-column joint can remarkably prevent

premature flange fracture in welds.

3. Test results also show that local buckling occasion of the specimens could be delayed because the tapered beam flange provided an extensive uniform yielding in the beam. These specimens sustained a sufficient rotation of 5% rad story drift angle, satisfying the requirements for connections used in SMFs. The ductility of the moment connection is successfully improved by the application of the tapered flange.
4. The extra cost for fabricating such built-up tapered flange connection is relatively high, compared to the traditional unreinforced connection. However, this new style of moment connections, using either the column-tree or the pre-Northridge design practice in the connection, can perform good ductile behavior and result in the stable energy dissipation.

#### **Implication of frame analysis**



1. The nonlinear static pushover analyses performed in both frames demonstrate that the globally structural behaviors of steel SMFs, such as strength degradation and yield sequences, are reasonably evaluated by using the verified connection models. The pushover analysis, as a result, can be used as an efficient design procedure for the performance evaluation of buildings under some concerned performance levels.
2. SMFs with unreinforced connections exhibited limited inelastic behavior with the amount of connections failed, which caused 17% and 75% strength reduction in five- and fifteen-story frames, respectively, at the CP performance level. On the contrary, large inelastic deformation with a steady post-yielding behavior is

observed in the TF frames. Significantly, the ductile capability of the TF frames is larger than that of the UR frames.





## References

- AISC (2005a), *Seismic provisions for structural steel buildings*, American Institute of Steel Construction, Inc., Chicago, IL.
- AISC (2005b), *Specification for structural steel buildings*, ANSI/AISC 360-05, American Institute of Steel Construction, Inc., Chicago, IL.
- Anderson, J. C., and Duan, X. (1998), "Repair/upgrade procedures for welded beam to column connections." *Rep. No. PEER 98/03, Pacific Earthquake Engineering Research Center*, Richmond, California.
- ANSYS (2002), *User Manual*, Swanson Analysis Systems, Inc.
- BSSC (1997), *NEHRP guidelines for seismic rehabilitation of buildings*, FEMA-273, Federal Emergency Management Agency, Washington, DC.
- Chen, S. J., Yeh, C. H., and Chu, J. M. (1996), "Ductile steel beam-to-column connections for seismic resistance." *Journal of Structural Engineering*, ASCE, Vol. 122, No. 11, pp 1292-1299.
- Chen, S. J., Tsao, Y. C., and Chao, Y. C. (2001), "Enhancement of ductility of existing seismic steel moment connections." *Journal of Structural Engineering*, ASCE, Vol. 127, No. 5, pp 538-545.
- Chen, C. C., Lee, J. M., and Lin, M. C. (2003), "Behaviour of steel moment connections with a single flange rib." *Engineering Structures*, Vol. 25, pp 1419-1428.
- Chen, C. C., Lin, C. C., and Tsai, C. L. (2004), "Evaluation of reinforced connections between steel beams and box columns." *Engineering Structures*, Vol. 26, No. 13, pp 1889-1904.
- Chen, C. C., Chen, S. W., Chung, M. D., and Lin, M. C. (2005a), "Cyclic behaviour of unreinforced and rib-reinforced moment connections." *Journal of Constructional Steel Research*, Vol. 61, No. 1, pp 1-21.
- Chen, C. C., Lu, C. A., and Lin, C. C. (2005b), "Parametric study and design of rib-reinforced steel moment connections." *Engineering Structures*, Vol. 27, No. 5, pp 699-708.
- Chen, C. C., Lin, C. C., and Lin, C. H. (2006), "Ductile moment connections used in steel column-tree moment-resisting frames." *Journal of Constructional Steel Research*, Vol. 62, No. 8, pp 793-801.
- Cornell, C. A., Jalayer, F., Hamburger, R. O., and Foutch, D. A. (2002), "Probabilistic basis for the 2000 SAC Federal Emergency Management Agency steel moment frame guidelines." *Journal of Structural Engineering*, ASCE, Vol. 128, No. 4, pp 526-533.

- El-Tawil, S., Vidarsson, E., Mikesell, T., and Kunnath, S. K. (1999), "Inelastic behavior and design of steel panel zones." *Journal of Structural Engineering*, ASCE, Vol. 125, No. 2, pp 183-193.
- El-Tawil, S., Mikesell, T., and Kunnath, S. K. (2000), "Effect of local details and yield ratio on behavior of FR steel connections." *Journal of Structural Engineering*, ASCE, Vol. 126, No. 1, pp 79-87.
- Engelhardt, M. D., Sabol, T. A., Aboutaha, R. S., and Frank, K. H. (1995), "Testing connections." *Modern Steel Construction*, AISC, Vol. 35, No. 5, pp 36-44.
- Engelhardt, M. D., and Sabol, T. A. (1998), "Reinforcing of steel moment connections with cover plates: benefits and limitations." *Engineering Structures*, Vol. 20, No. 4-6, pp 510-520.
- Engelhardt, M. D., Winneberger, T., Zekany, A. J., and Potyraj, T. J. (1998), "Experimental investigation dogbone moment connections." *Engineering Journal*, Fourth Quarter AISC, pp 128-139.
- FEMA (2000), *Recommended seismic design criteria for new steel moment-frame buildings*, FEMA-350, Federal Emergency Management Agency, Washington, DC.
- Habibullah, A. and Wilson, E. (2004). "SAP2000: Integrated finite element analysis and design of structures." Computers and Structures, Inc., Berkeley, CA.
- Jones, S. L., Fry, G. T., and Engelhardt, M. D. (2002), "Experimental evaluation of cyclically loaded reduced beam section moment connections." *Journal of Structural Engineering*, ASCE, Vol. 128, No. 4, pp 441-451.
- Kim, T., Whittaker, A. S., Gilani, A. S. J., Bertero, V. V., and Takhirov, S. M. (2002a), "Cover-plate and flange-plate steel moment-resisting connections." *Journal of Structural Engineering*, ASCE, Vol. 128, No. 4, pp 474-482.
- Kim, T., Whittaker, A. S., Gilani, A. S. J., Bertero, V. V., and Takhirov, S. M. (2002b), "Experimental evaluation of plate-reinforced steel moment-resisting connections." *Journal of Structural Engineering*, ASCE, Vol. 128, No. 4, pp 483-491.
- Kim, T., Stojadinovic, B., and Whittaker, A. S. (2004), "Seismic performance of US steel box column connections." *Proceedings, 13th World Conference on Earthquake Engineering (13WCEE)*, Canada; Paper No. 981.
- Lee, C. H. (2002), "Seismic design of rib-reinforced steel moment connections based on equivalent strut model." *Journal of Structural Engineering*, ASCE, Vol. 128, No. 9, pp 1121-1129.
- Lu, L. W., Ricles, J. M., Mao, C., and Fisher, J. W. (2002), "Critical issues in achieving ductile behaviour of welded moment connections." *Journal of Constructional Steel Research*, Vol. 55, pp 325-341.

- Miller, D. K. (1998), "Lessons learned from the Northridge earthquake." *Engineering Structures*, Vol. 20, No. 4-6, pp. 249-260.
- Nakashima, M., Inoue, K., and Tada, M. (1998), "Classification of damage to steel buildings observed in the 1995 Hyogoken-Nanbu earthquake." *Engineering Structures*, Vol. 20, No. 4-6, pp 271-281.
- Plumier, A. (1997), "The dogbone: back to the future." *Engineering Journal*, Second Quarter AISC, pp 61-67.
- Popov, E. P., Yang, T. S., and Chang, S. P. (1998), "Design of steel MRF connections before and after 1994 Northridge earthquake." *Engineering Structures*, Vol. 20, No. 12, pp 1030-1038.
- Ricles, J. M., Mao, C., Lu, L. W., and Fisher, J. W. (2002), "Inelastic cyclic testing of welded unreinforced moment connections." *Journal of Structural Engineering*, ASCE, Vol. 128, No. 4, pp 429-440.
- Roeder, C. W. (2002), "General issues influencing connection performance." *Journal of Structural Engineering*, Vol. 128, No. 4, pp 420-428.
- Stojadinović, B., Goel, S. C., Lee, K. H., Margarian, A. G., and Choi, J. H. (2000), "Parametric tests on unreinforced steel moment connections." *Journal of Structural Engineering*, ASCE, Vol. 126, No. 1, pp 40-49.
- Uang, C. M., Kent Yu, Q. S., Noel, S., and Gross, J. (2000), "Cyclic testing of steel moment connections rehabilitated with RBS or welded haunch." *Journal of Structural Engineering*, ASCE, Vol. 126, No. 1, pp 57-68.
- UBC (1997), "*Uniform Building Code*." International Conference of Building Officials, Whittier, California.
- Zhang, X., and Ricles, J. M. (2006), "Experimental evaluation of reduced beam section connections to deep columns." *Journal of Structural Engineering*, ASCE, Vol. 132, No. 3, pp 346-357.
- Yun, S. Y., Hamburger, R. O., Cornell, C. A., and Foutch, D. A. (2002), "Seismic performance evaluation for steel frames." *Journal of Structural Engineering*, ASCE, Vol. 128, No. 4, pp 534-545.
- 陳嘉有 (1995), 「韌性鋼骨梁柱接頭行為研究」, 國立台灣大學土木工程學系碩士論文。
- 陳誠直、呂正安、王亭復 (2003), 「以加長型單肋板提昇鋼構造梁柱接頭之耐震性能」, 結構工程, 第十八卷, 第三期, 19-34 頁。
- 內政部營建署, (2005), 「建築物耐震設計規範及解說」。

Table 3.1 Parameters used in finite element analysis

Model No.	Parameter				Geometry		Note
	$\beta_j$	$L_{wl}$ ( $b_f$ )	$L_{tap}$ ( $d_b$ )	$L_{ext}$ ( $d_b$ )	Max. width of beam flange (mm)	Length of stub beam (mm)	
1	1.00	—	—	—	300	1000	Pre-Kobe type
2	1.05	0.50	0.30	0.50	372	760	
3			0.50		394	900	
4			0.80		430	1110	
5	1.10	0.50	0.30	0.50	395	760	
6			0.50		416	900	
7			0.80		455	1110	
8	1.20	0.50	0.30	0.50	440	760	Control model
9				0.25	440	585	
10				—	440	410	
11			0.50	0.50	463	900	
12			0.80		505	1110	
13		0.33	0.30		430	710	
14		0.17			422	660	
15	1.25	0.50	0.30	0.50	460	760	
16			0.50		486	900	
17			0.80		530	1110	

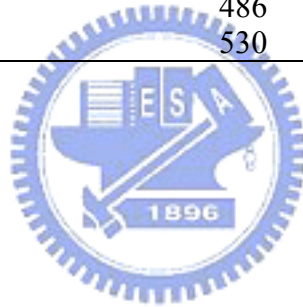


Table 4.1 Material properties of test specimens

Member	Coupon	Yield strength, $F_y$ (MPa)	Tensile strength, $F_u$ (MPa)
Link beam	Beam flange	387	507
	Beam web	429	529
Stub beam	Beam flange	371	511
	Beam web	373	494
Column	Column flange and web	431	578

Table 4.2 Details of test specimens

Specimen*	$\beta_j$	$L_{lap}$ ( $d_b$ )	Beam web joint detail
PK	—	—	Fillet welded web
W1-L05	1.20	0.5	Fillet welded web
W1-L03	1.20	0.3	Fillet welded web
W2-L03	1.10	0.3	Fillet welded web
W3-L03	1.05	0.3	Fillet welded web
B1-L03	1.20	0.3	Bolted shear tab
B2-L03	1.10	0.3	Bolted shear tab

\*All specimens consist of an H-shaped H700×300×13×24 beam (dimensions in mm for depth, width, web thickness, and flange thickness, respectively) and a built-up box 550×550×28×28 column.

Table 4.3 Overview of test results

Specimen	Total story drift rotation (% rad)	Total plastic rotation (% rad)	Beam plastic rotation (% rad)	Failure mode
PK	+4.0	+2.6	+2.4	Brittle fracture
	-3.0	-1.7	-1.4	
W1-L05*	+5.0	+3.9	+3.9	Local buckling
	-5.0	-4.0	-4.0	
W1-L03*	+5.0	+4.0	+4.0	Local buckling
	-5.0	-4.0	-4.0	
W2-L03*	+5.0	+4.0	+3.9	Local buckling
	-5.0	-4.0	-3.9	
W3-L03	+4.0	+2.7	+2.6	Brittle fracture
	-5.0	-3.9	-3.8	
B1-L03*	+5.0	+4.0	+3.9	Local buckling
	-5.0	-4.0	-3.9	
B2-L03*	+5.0	+3.9	+3.9	Local buckling
	-5.0	-4.0	-4.0	

\*Test was stopped due to the stroke limitation of the actuator.

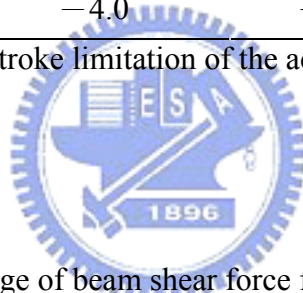


Table 5.1 Percentage of beam shear force for specimen W1-L03

Drift level	Shear component	Distance from column face (mm)			
		20	200	410	760
0.5% rad	Beam web (%)	52	91	95	95
	Beam flanges (%)	48	9	5	5
4% rad	Beam web (%)	58	93	95	98
	Beam flanges (%)	42	7	5	2

Table 7.1 Dead loads for studied buildings

Description	Equivalent uniform load		
	(N/m <sup>2</sup> )	(kgf/m <sup>2</sup> )	
Slab (15 cm deep, lightweight concrete)	1,766	180	
Metal deck (thickness of 1.2 cm, ALK 12)	147	15	
Ceiling	245	25	
Mechanical/Electrical	491	50	
Fireproofing	98	10	
Raised floor	589	60	
Asphalt paving (only impose at roof)	785	80	
Curtain wall	785	80	
Total	Roof	3,532	360
	Floors	4,120	420

Table 7.2 Live loads for studied buildings

Description	Equivalent uniform load		
	(N/m <sup>2</sup> )	(kgf/m <sup>2</sup> )	
Office occupancy	2,943	300	
Partitions	981	100	
Total	Roof	2,943	300
	Floors	3,924	400

Table 7.3 Distribution of design seismic forces for studied frames

Model name	Floor level	Lateral earthquake forces (kN)	Story shear forces (kN)
UR-5F	5	333	333
	4	300	633
	3	232	865
	2	165	1030
	1	97	1127
UR-15F	15	514	514
	14	226	740
	13	210	950
	12	195	1144
	11	179	1323
	10	163	1486
	9	148	1634
	8	132	1766
	7	116	1882
	6	101	1983
	5	85	2068
	4	69	2137
	3	54	2191
	2	38	2229
	1	22	2251

Table 7.4 Tapered flanges used in studied frames

Model name	Beam size	Tapered flange size			
		$b_{f,j}$ (mm)	$L_{tap}$ (mm)	$L_{w1}$ (mm)	$L_{w2}$ (mm)
TF-5F	H500×300×10×20	407	150	150	50
	H600×300×12×25	413	180	150	50
TF-15F	H600×300×12×25	414	180	150	50
	H700×300×13×24	425	210	150	50
	H750×350×14×25	500	225	175	50



Table 7.5 Confidence levels for different confidence parameters  $\lambda$  with hazard parameter  $k=4.62$ 

Uncertainty $\beta_{UT}$	Confidence level												
	2%	5%	10%	20%	30%	40%	50%	60%	70%	80%	90%	95%	99%
0.1	1.26	1.21	1.16	1.11	1.08	1.05	1.02	1.00	0.97	0.94	0.90	0.87	0.81
0.2	1.65	1.52	1.42	1.30	1.22	1.15	1.10	1.04	0.99	0.93	0.85	0.79	0.69
0.3	2.28	2.02	1.81	1.58	1.44	1.33	1.23	1.14	1.05	0.96	0.84	0.75	0.61
0.4	3.29	2.79	2.42	2.03	1.78	1.60	1.45	1.31	1.17	1.03	0.87	0.75	0.57
0.5	4.97	4.06	3.38	2.71	2.32	2.02	1.78	1.57	1.37	1.17	0.94	0.78	0.56
0.6	7.87	6.16	4.96	3.81	3.15	2.67	2.30	1.97	1.68	1.39	1.06	0.86	0.57

Example:

For the case of TF-15F at the global CP performance level, given

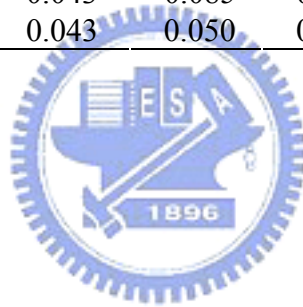
Uncertainty coefficient  $\beta_{UT}=0.5$

Confidence parameters  $\lambda=0.96$

Using linear interpolation between 0.94 (the corresponding confidence level=90%) and 1.17 (the corresponding confidence level=80%), the confidence level of 89% can be found.

Table 7.6 Confidence level evaluation for studied frames

Model name	Performance level	$D$	$C$	$\lambda$	Confidence level (%)	
					Analysis	Code
UR-5F	IO (Global)	0.011	0.020	1.12	46	50
	IO (Local)	0.011	0.020	1.24	49	50
	CP (Global)	0.045	0.100	0.63	98	90
	CP (Local)	0.045	0.030	1.98	13	50
TF-5F	IO (Global)	0.010	0.020	1.02	64	50
	IO (Local)	0.010	0.020	1.13	61	50
	CP (Global)	0.045	0.100	0.63	98	90
	CP (Local)	0.045	0.050	1.19	62	50
UR-15F	IO (Global)	0.013	0.020	1.24	28	50
	IO (Local)	0.013	0.020	1.38	36	50
	CP (Global)	0.064	0.085	1.43	67	90
	CP (Local)	0.064	0.030	3.38	1	50
TF-15F	IO (Global)	0.011	0.020	1.05	58	50
	IO (Local)	0.011	0.020	1.16	58	50
	CP (Global)	0.043	0.085	0.96	89	90
	CP (Local)	0.043	0.050	0.97	56	50



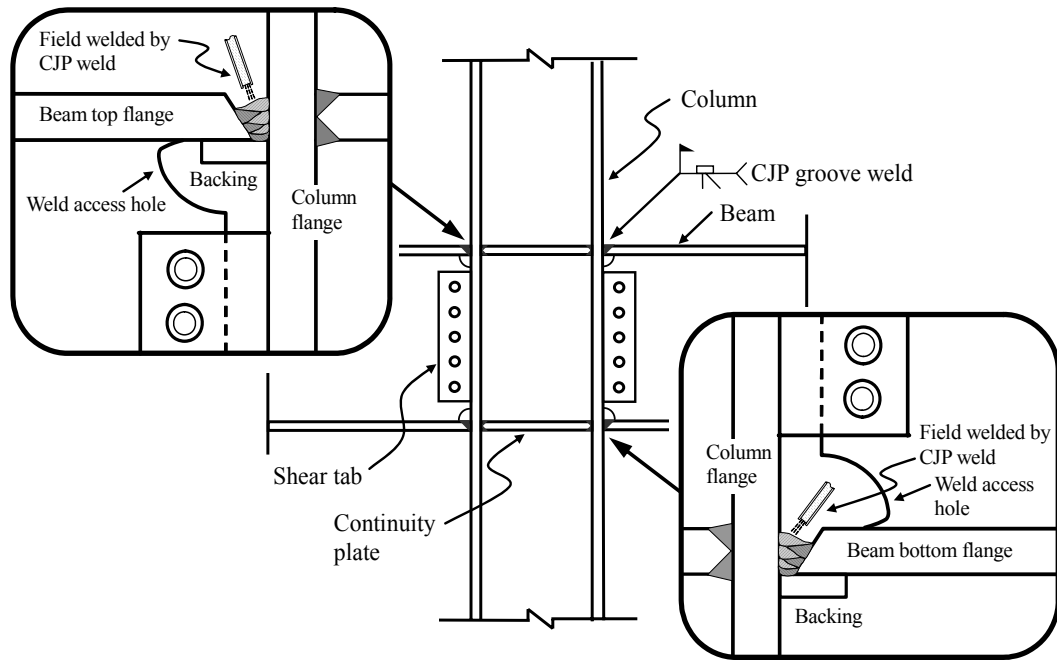


Figure 1.1 Connection details of web-bolted flange-welded pre-Northridge moment connection.



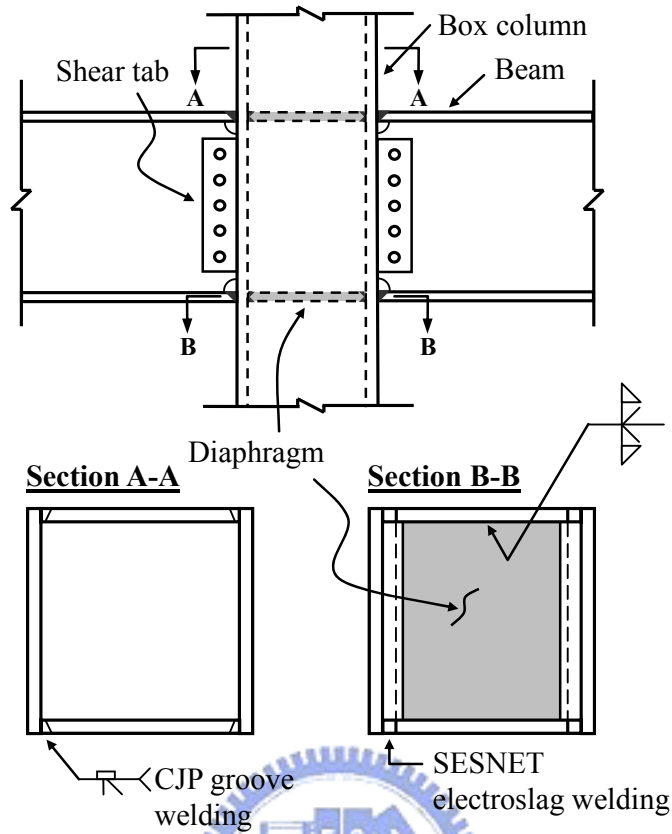


Figure 2. 1 Connection details between H-shaped beam and welded built-up box column.

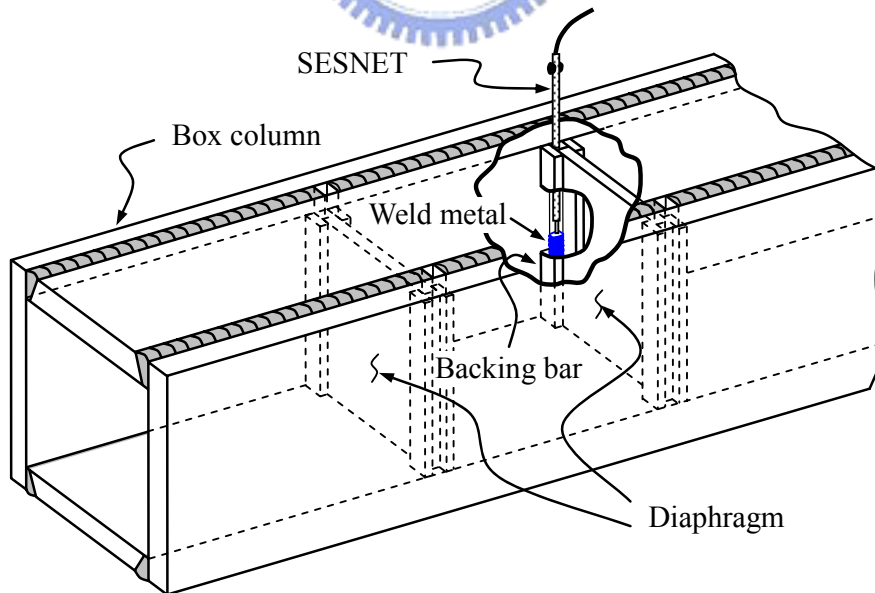


Figure 2.2 A schema of SESNET electroslag welding.

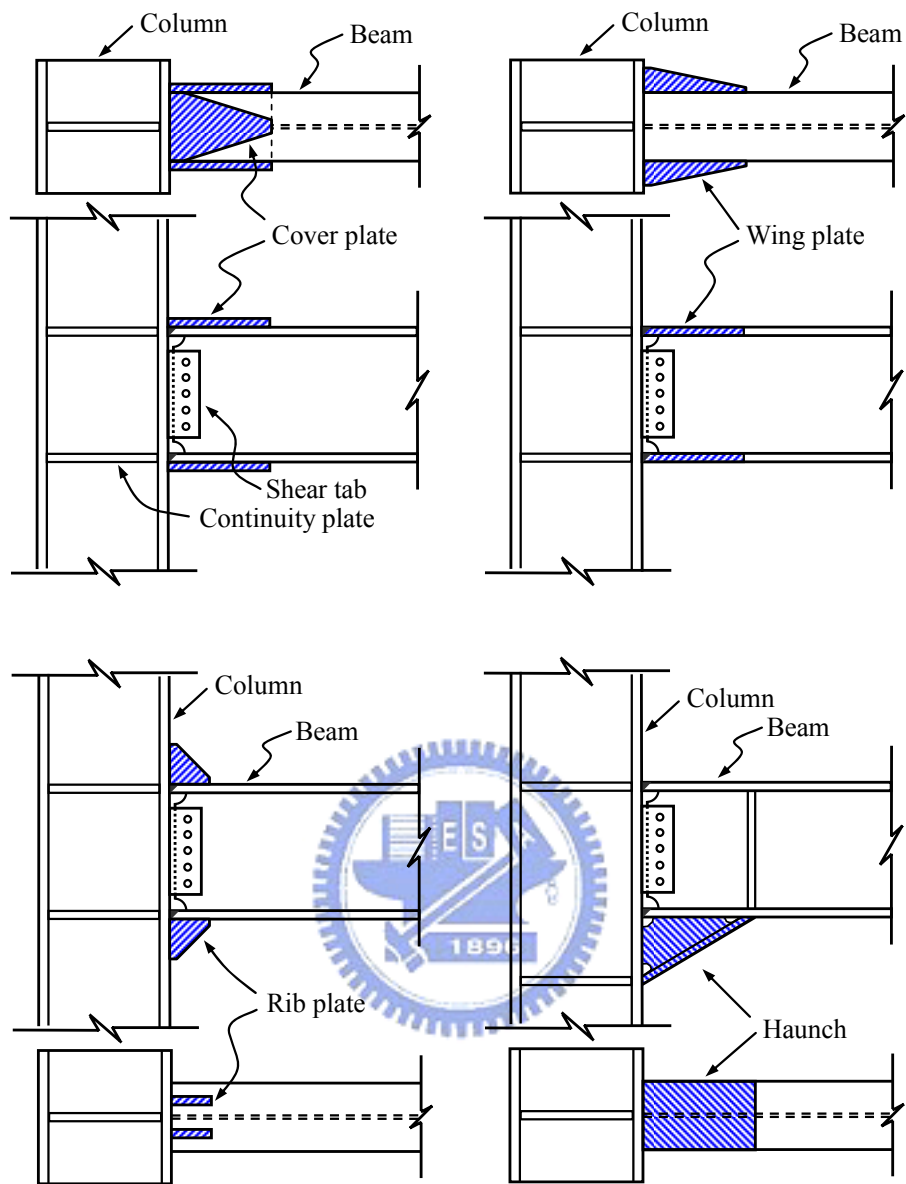


Figure 2.3 Examples of reinforced moment connections.

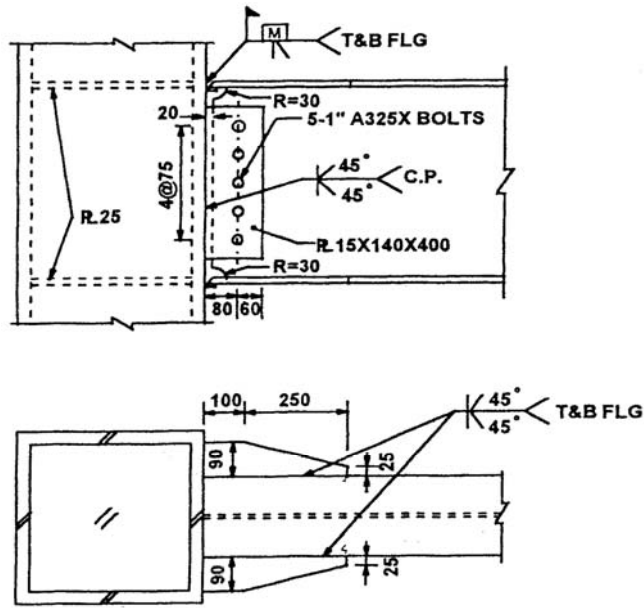


Figure 2.4 Reinforced moment connection with wing plates. (陳嘉有 1995)

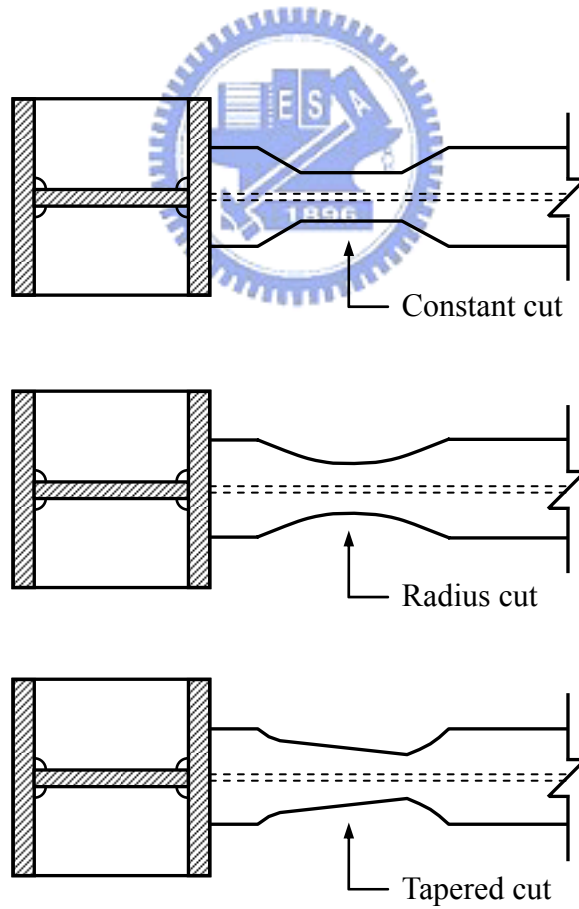


Figure 2.5 Different RBS configurations

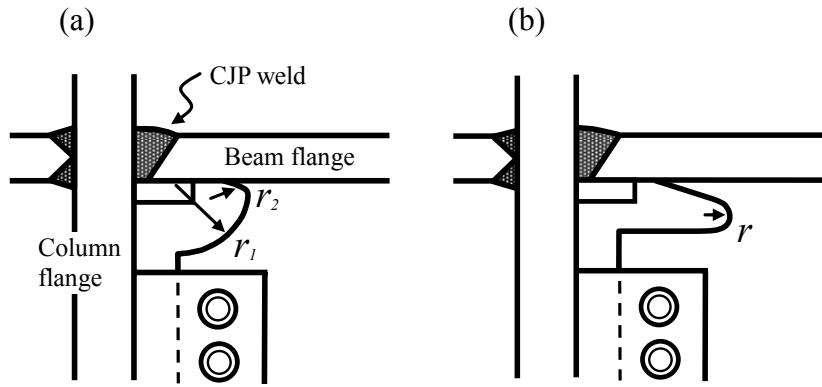


Figure 2.6 Weld access hole configurations: (a) a quarter-circular shape; (b) a modified shape recommended by FEMA-350.

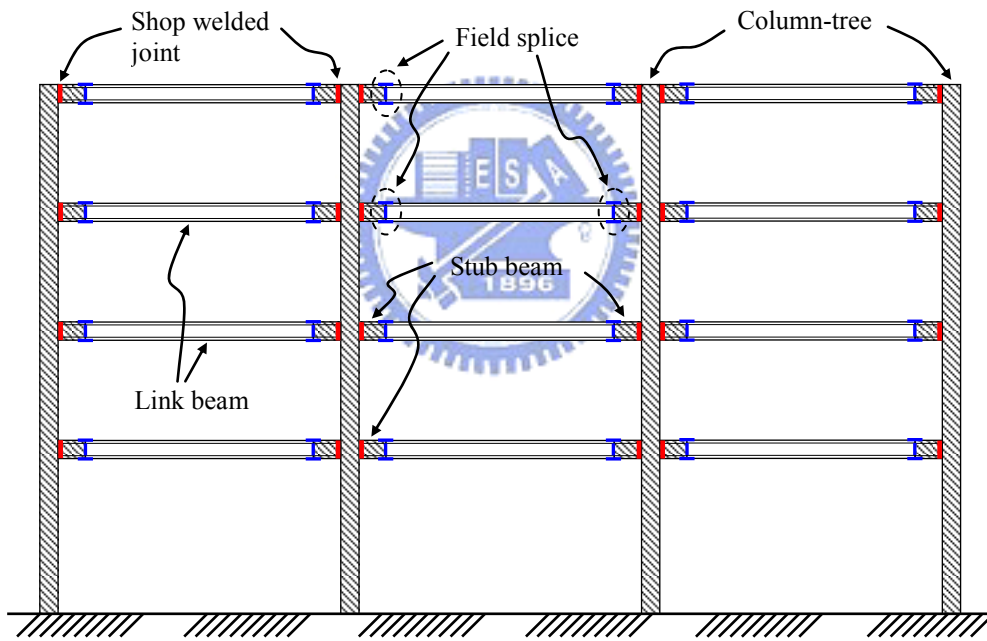


Figure 2.7 Steel column-tree moment frame

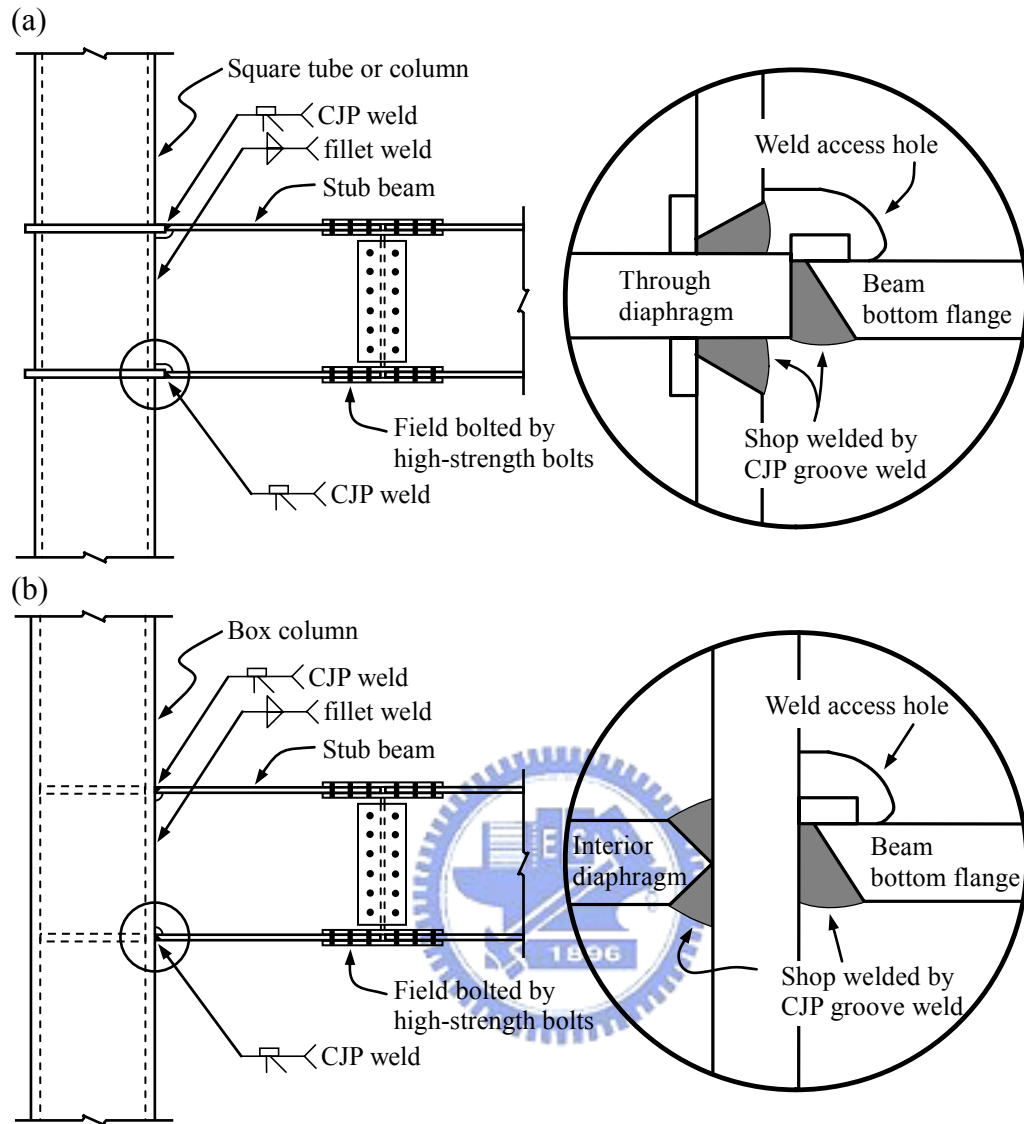


Figure 2.8 Typical pre-Kobe column-tree connections: (a) Through-diaphragm connection; (b) Interior-diaphragm connection.



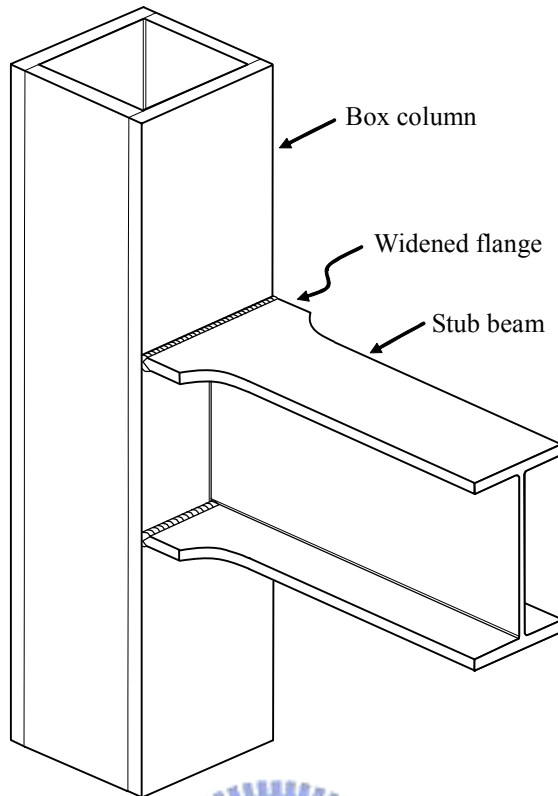


Figure 2.9 Widened flange connection configuration. (Chen et al. 2006)

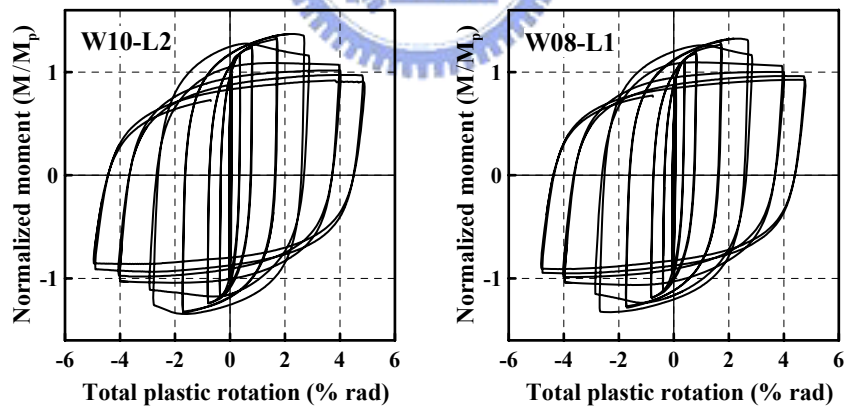


Figure 2.10 Normalized moment versus total plastic rotation curves for specimens W10-L2 and W08-L1. (Chen et al. 2006)

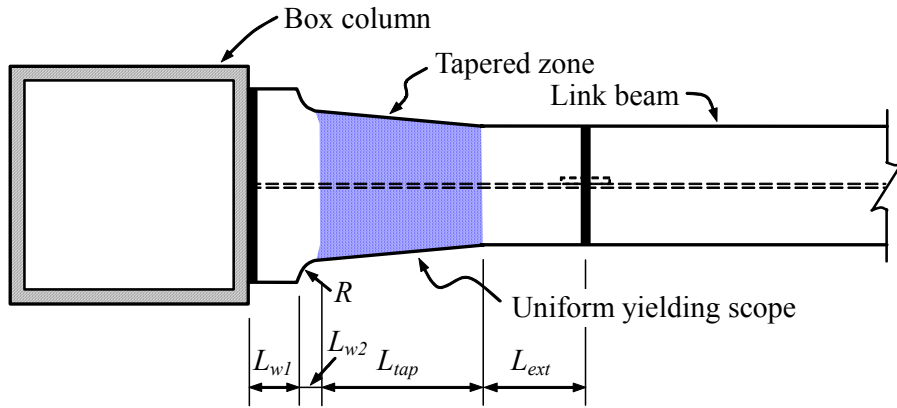


Figure 2.11 Geometry of tapered flange connection

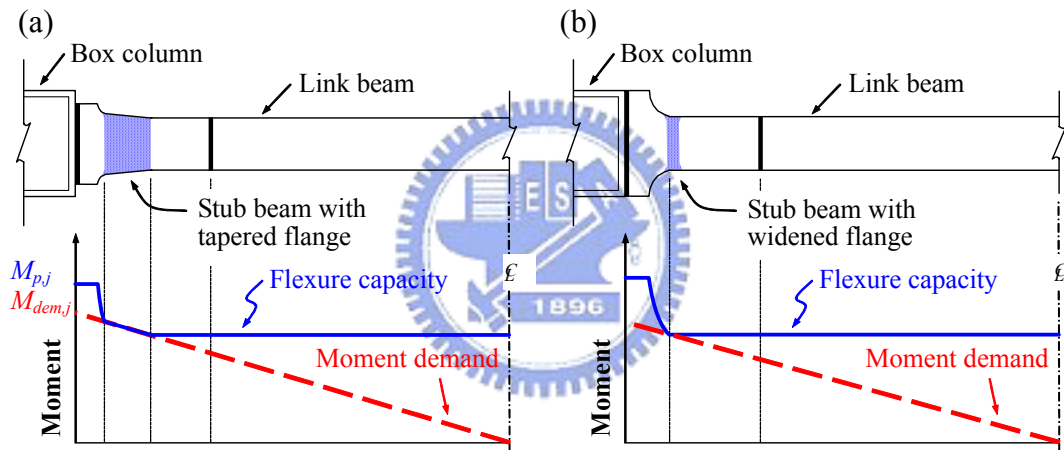


Figure 2.12 Comparison with seismic moment demand and flexure capacity: (a) for tapered flange connections; (b) for widened flange connections.

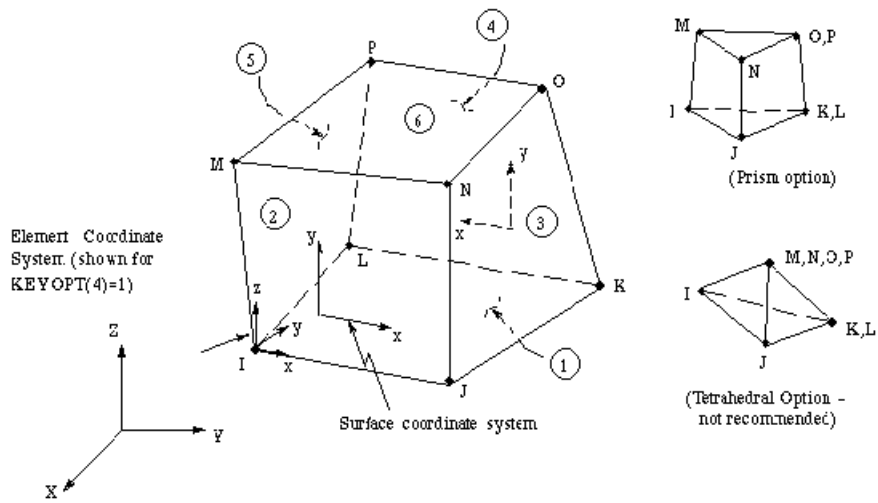


Figure 3.1 Geometry of 3-D structural solid element SOLID45 (ANSYS 2002)

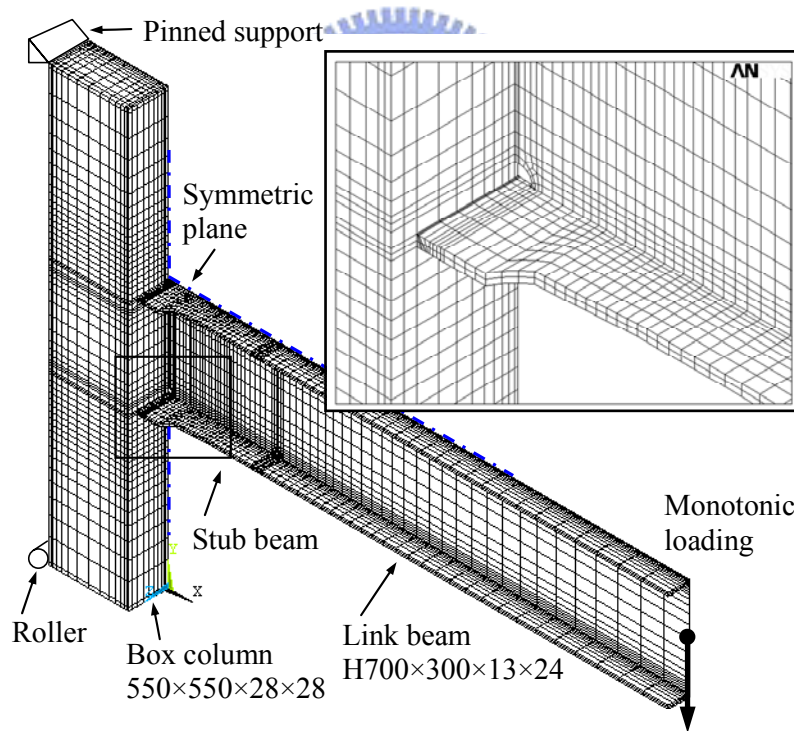


Figure 3.2 Boundary conditions and meshes of finite element model.

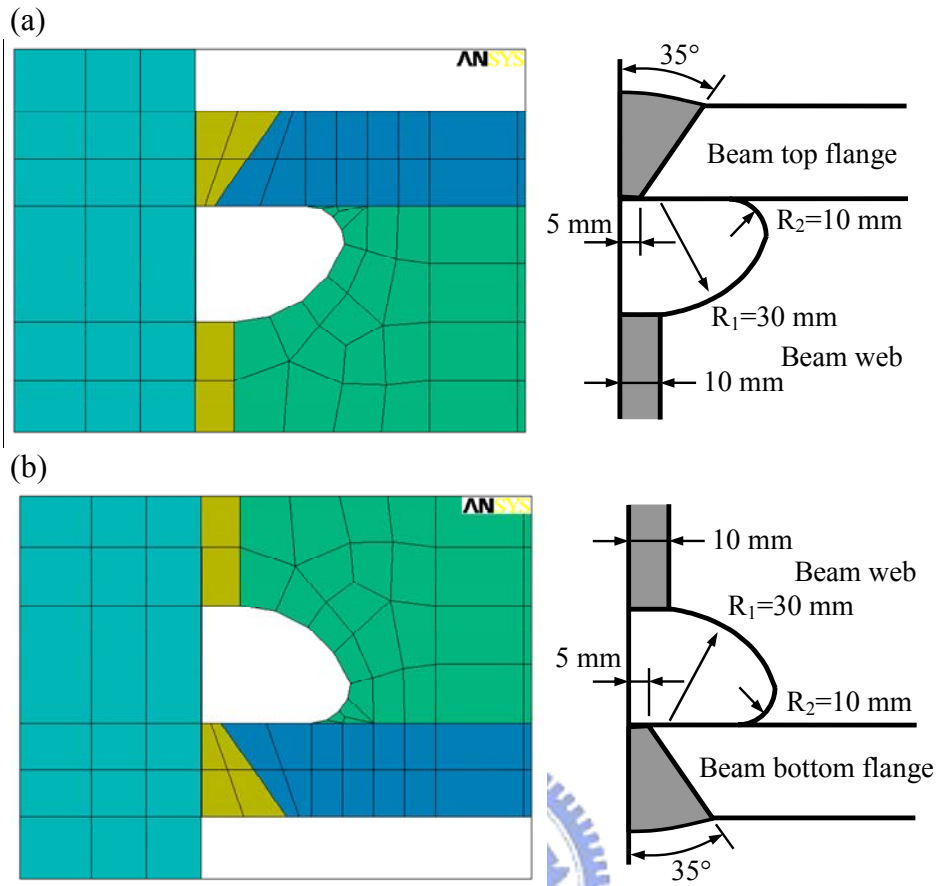


Figure 3.3 Details of weld access hole.

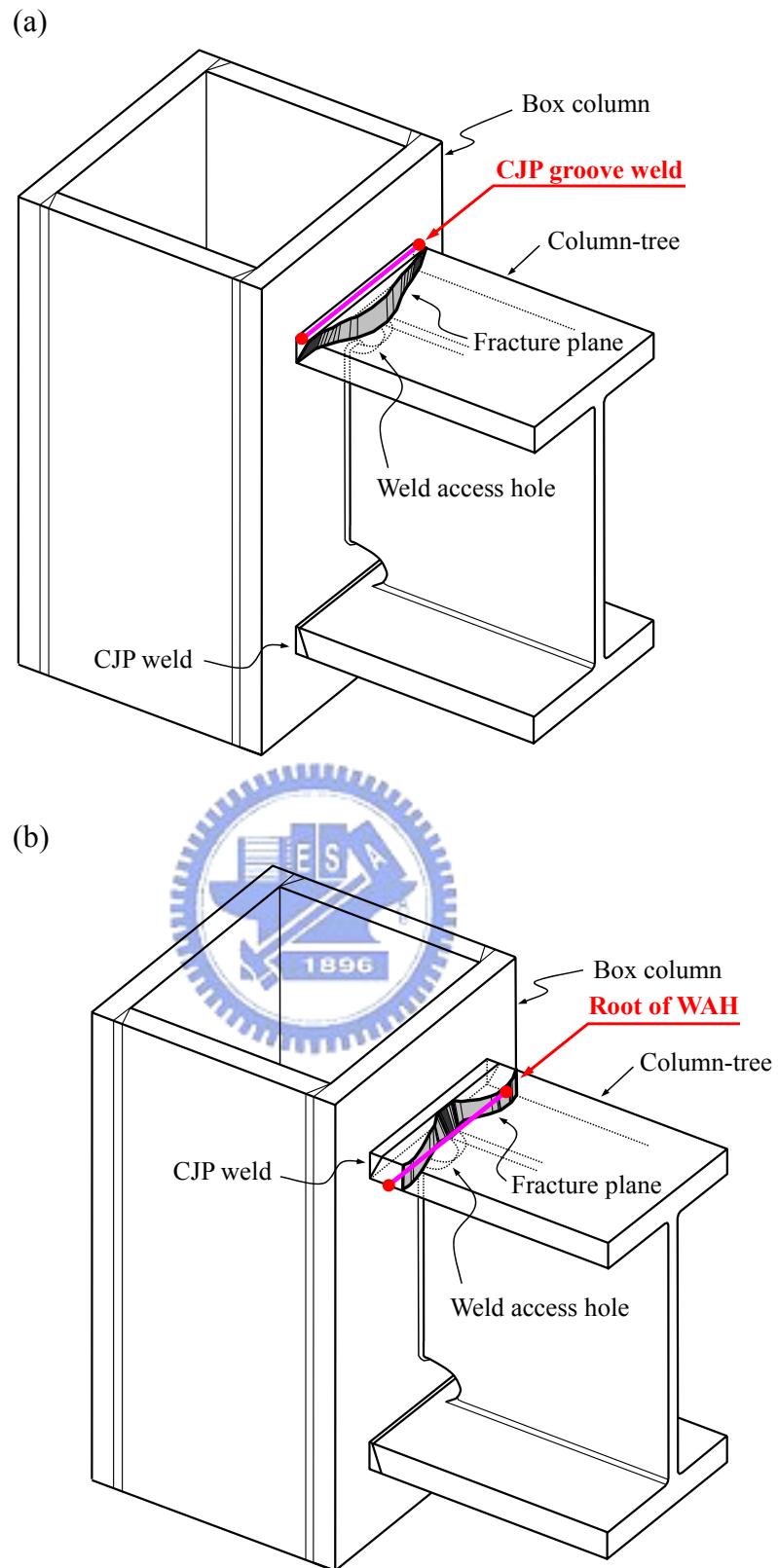


Figure 3.4 Critical sections of pre-Kobe connection: (a) at CJP groove weld; (b) at root of WAH.

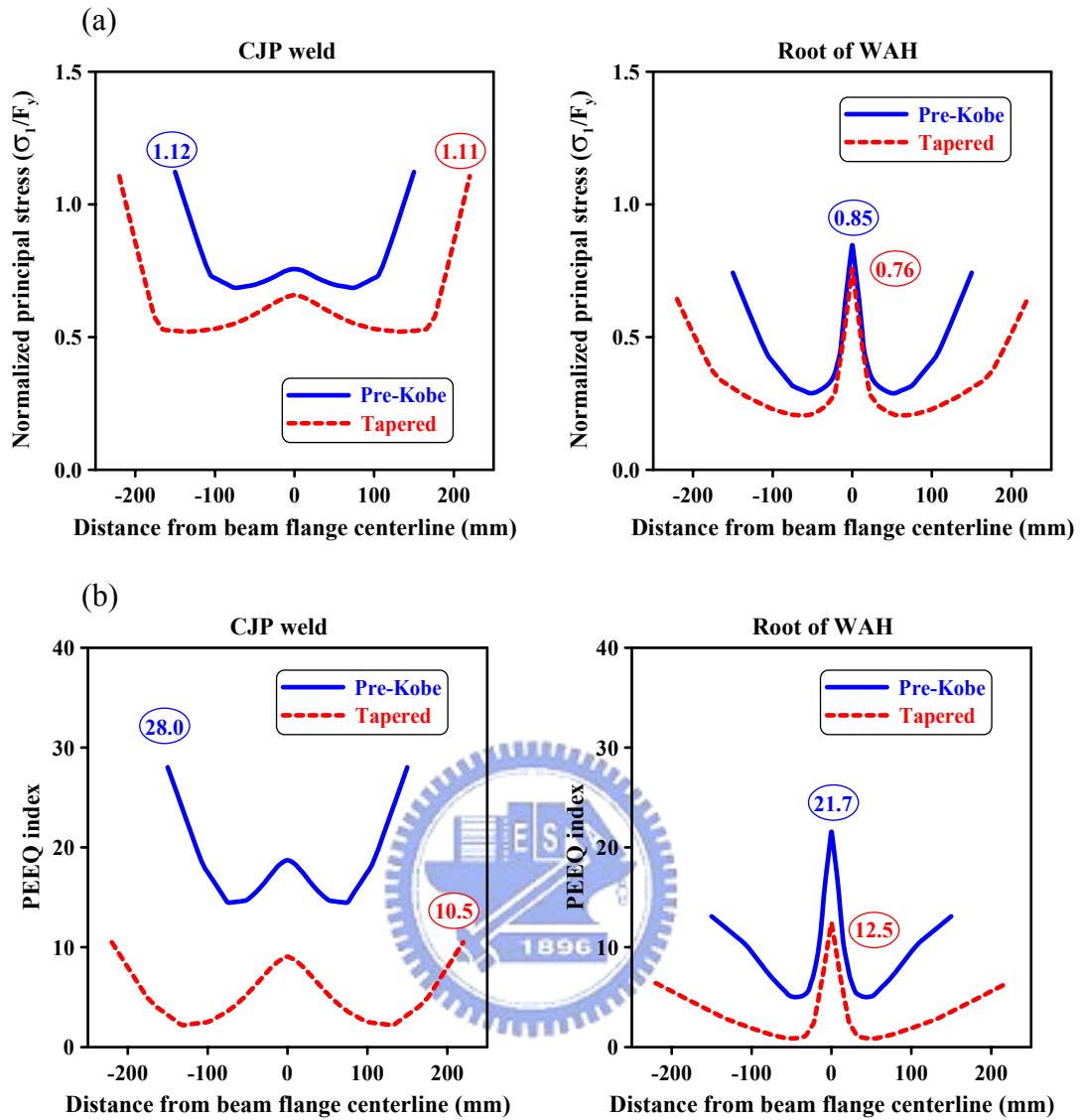


Figure 3.5 Distributions of normalized principal stresses and PEEQ indices along beam flange width at CJP weld and root of WAH: (a) normalized principal stress at 0.5% rad story drift angle; (b) PEEQ indices at 4% rad story drift angle.

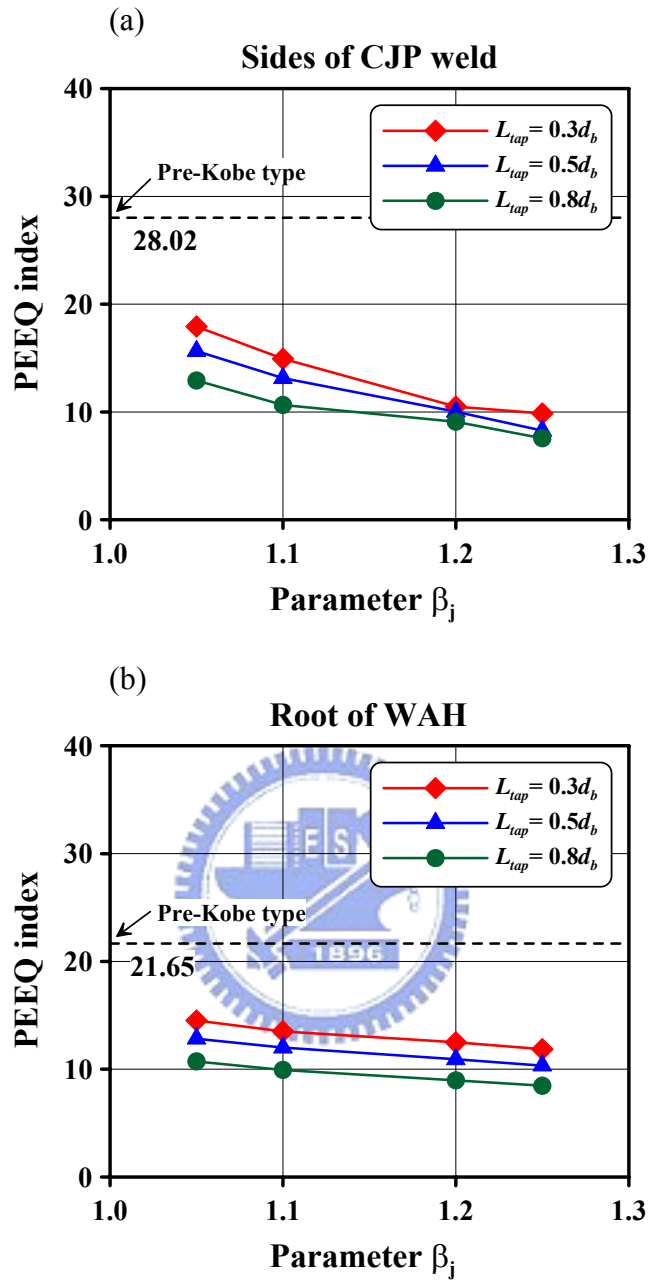


Figure 3.6 Effect of different values of parameter  $\beta_j$  and length of tapered part  $L_{tap}$  on PEEQ indices at 4% rad story drift angle: (a) at borders of CJP weld; (b) at root of WAH.

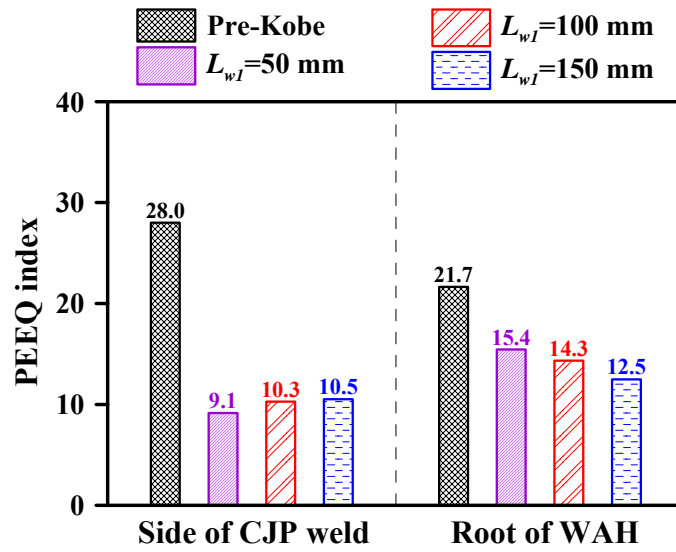


Figure 3.7 Effect of length of main tapered flange reinforced part  $L_{wl}$  on PEEQ indices at 4% rad story drift angle.

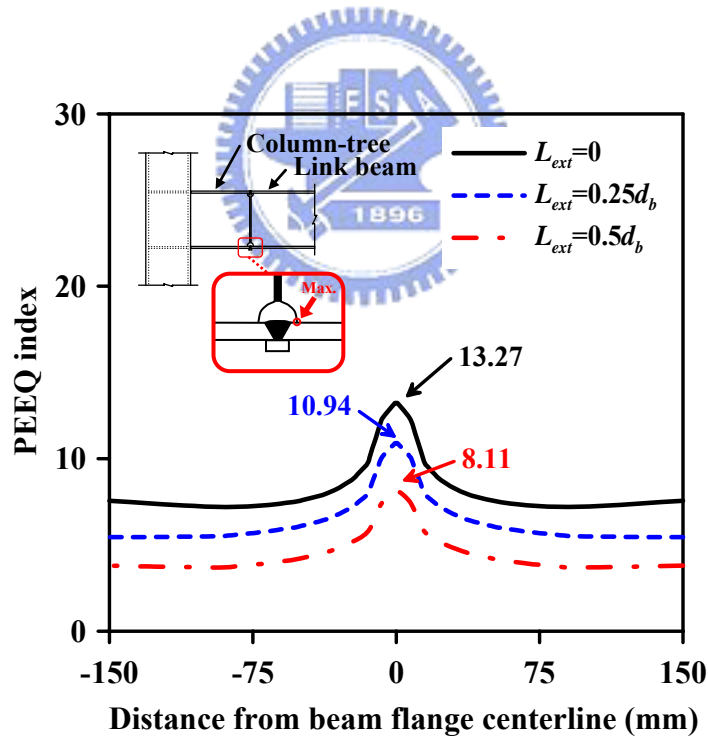


Figure 3.8 Effect of length of tapered flange extension  $L_{ext}$  on PEEQ indices along root of WAH between column-tree and link beam at 4% rad story drift angle.



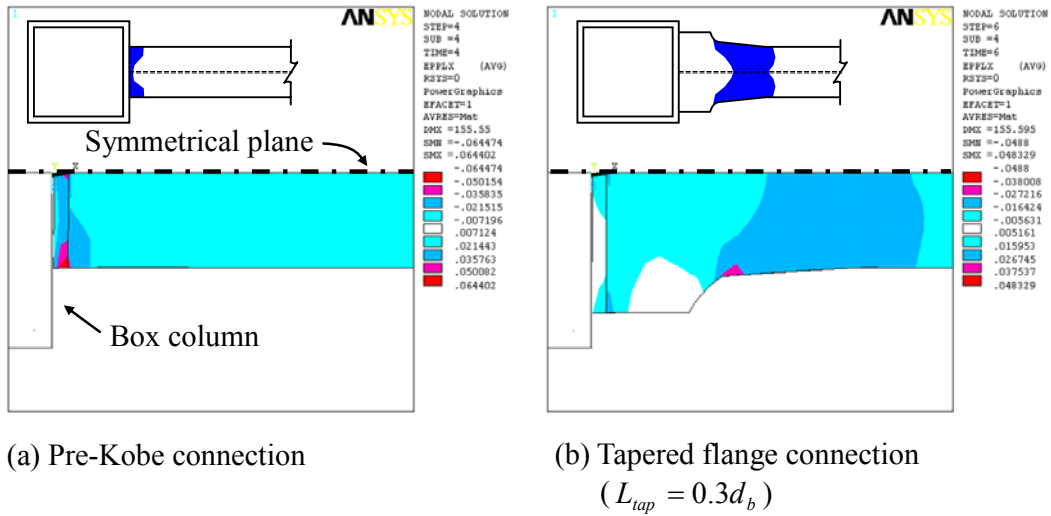


Figure 3.9 Longitudinal plastic strain contours for different configuration of connections during 4% rad story drift angle.

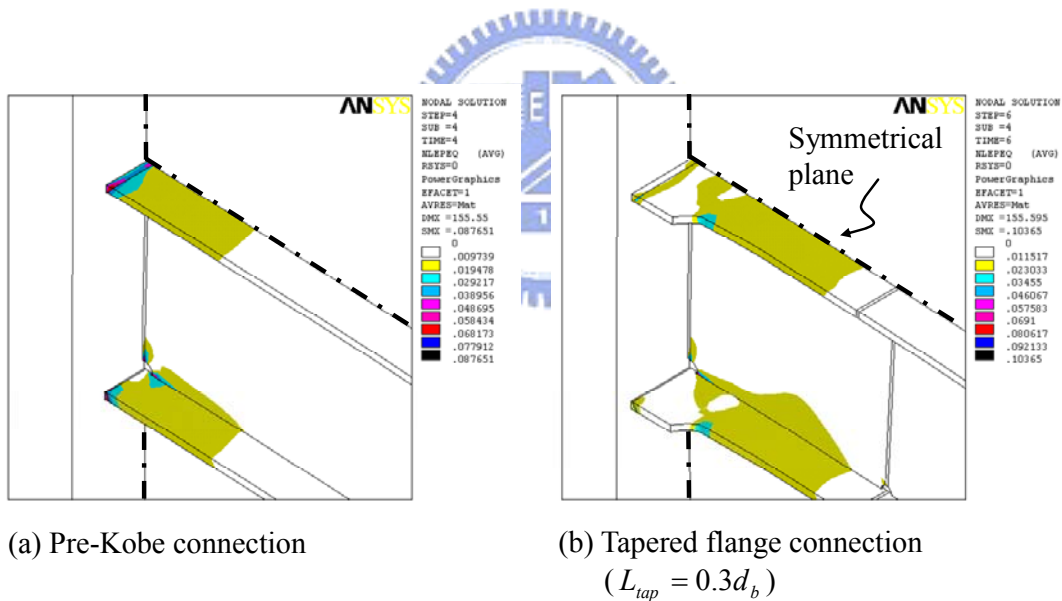


Figure 3.10 Contour plots of plastic equivalent strain for different configurations of connections at 4% rad story drift angle.



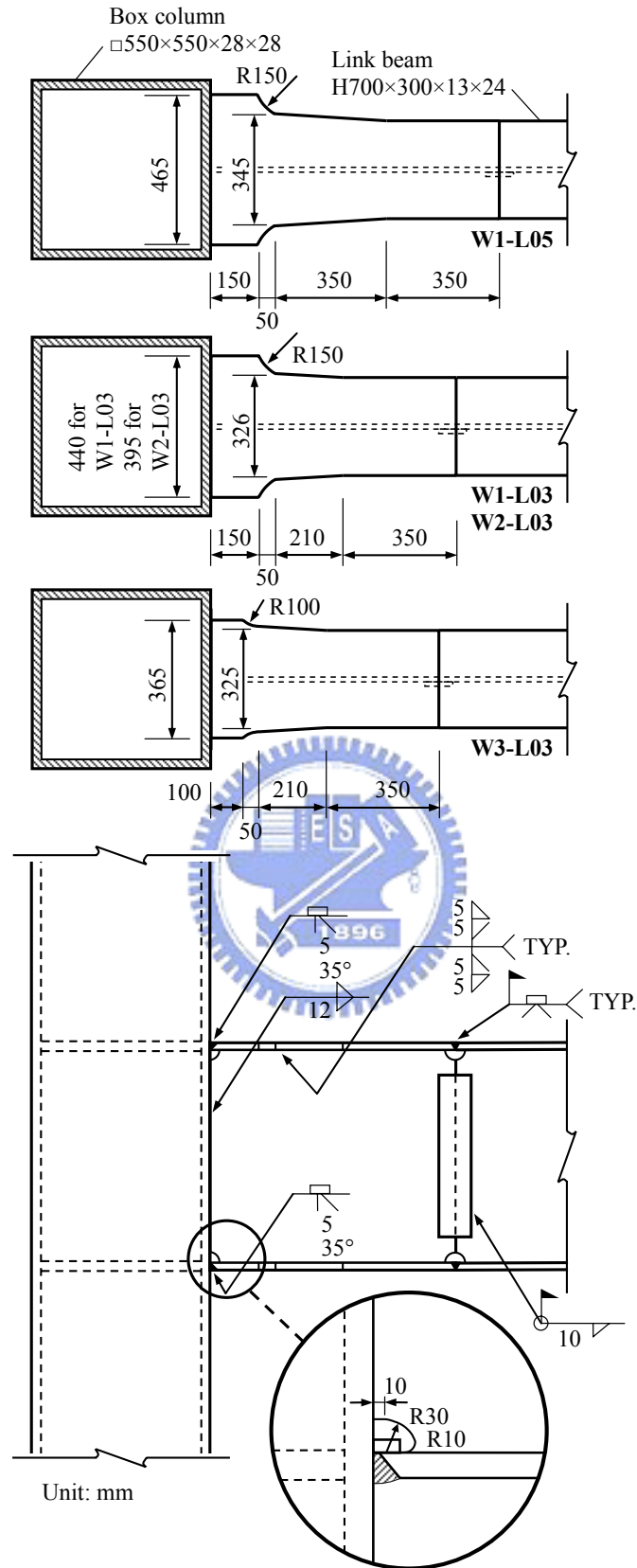


Figure 4.2 Connection details of specimen W1-L05, W1-L03, W2-L03, and W3-L03.

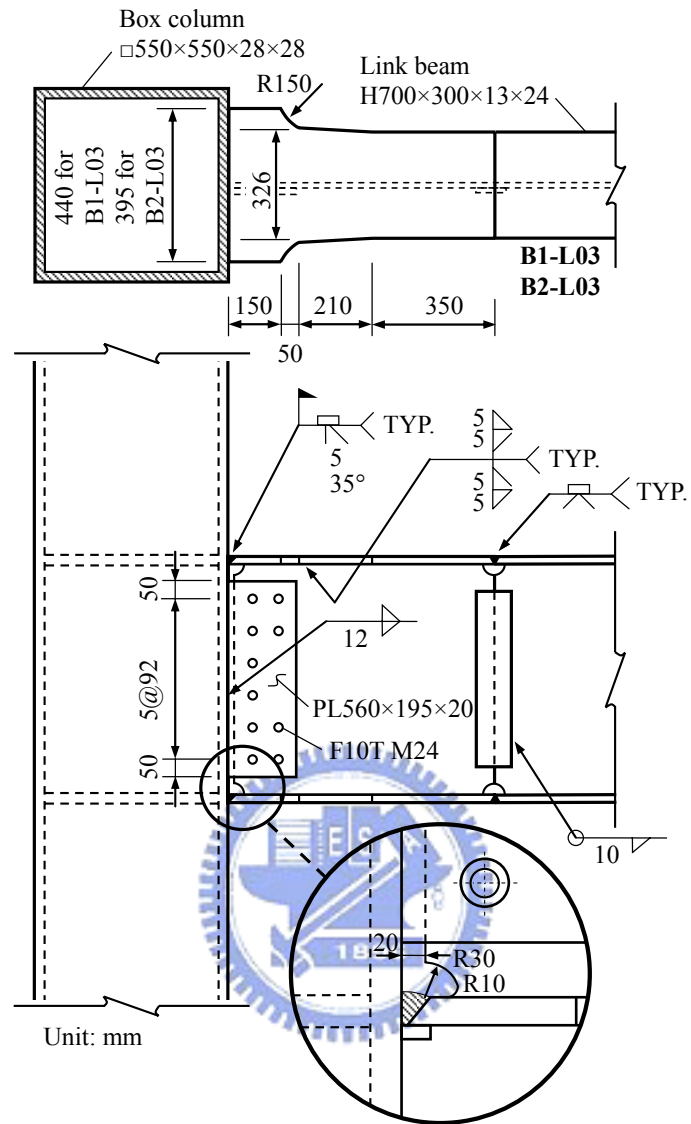


Figure 4.3 Connection details of specimen B1-L03 and B2-L03.

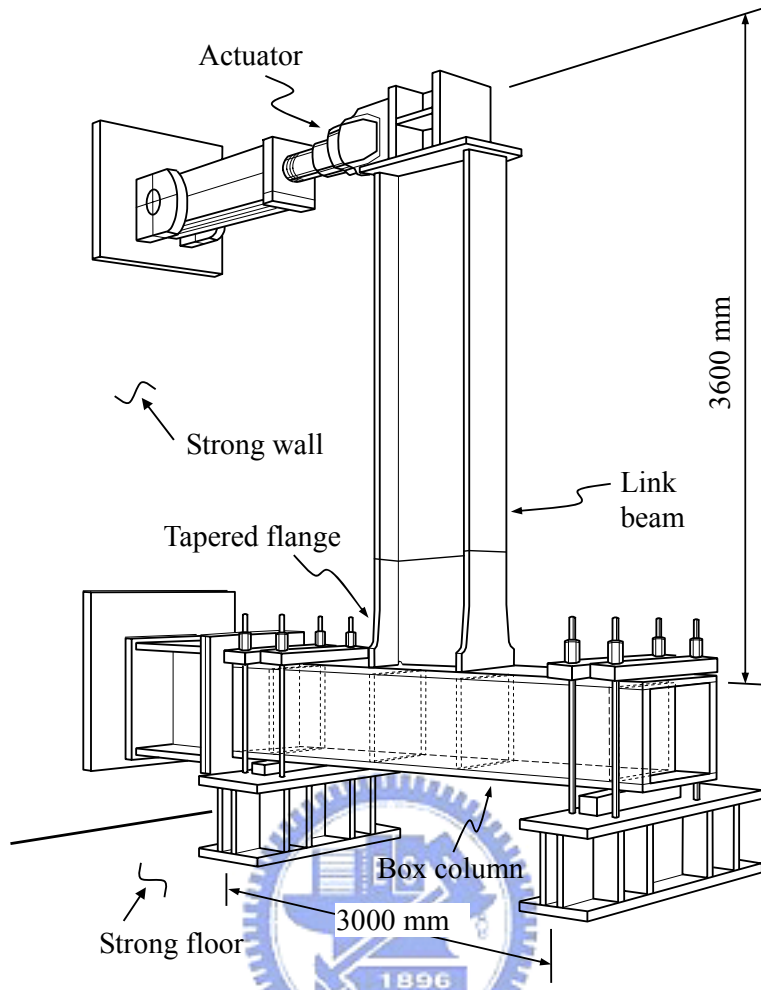


Figure 4.4 Overall view of test setup

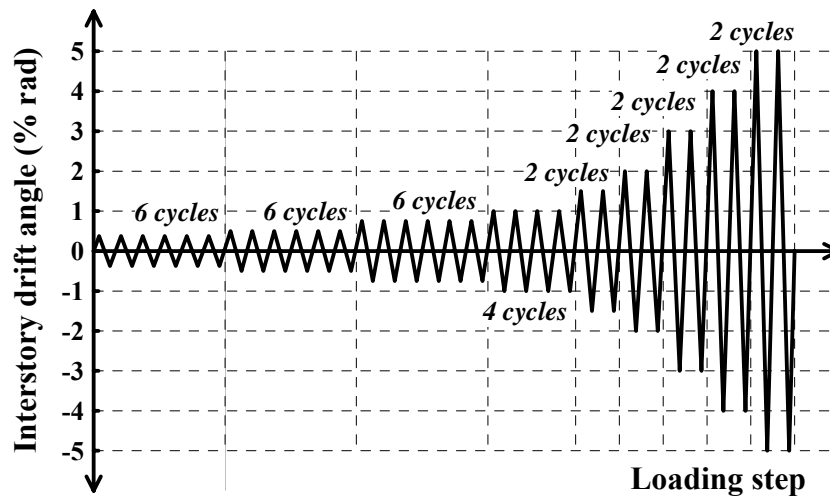


Figure 4.5 Loading history

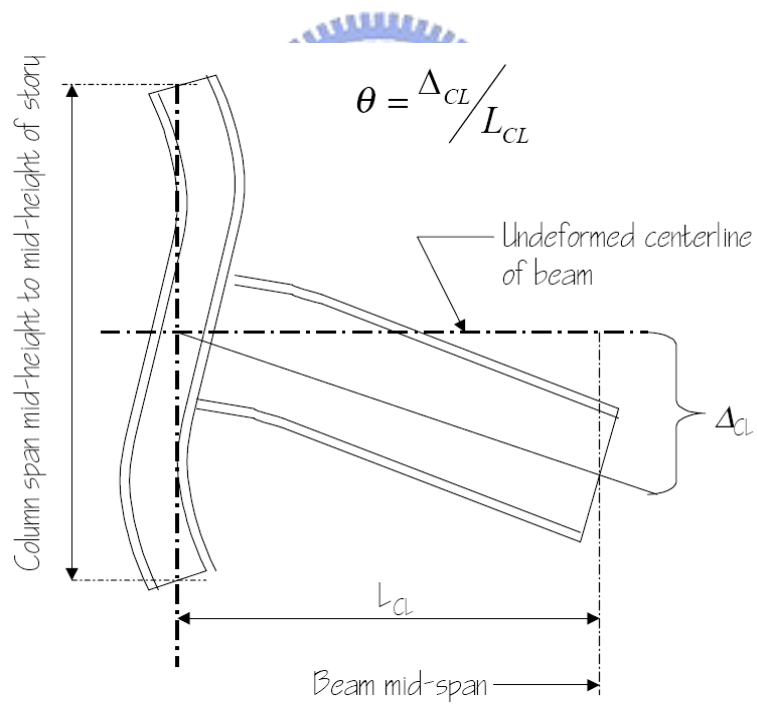


Figure 4.6 The definition of story drift angle for test assembly (FEMA-350 2000)

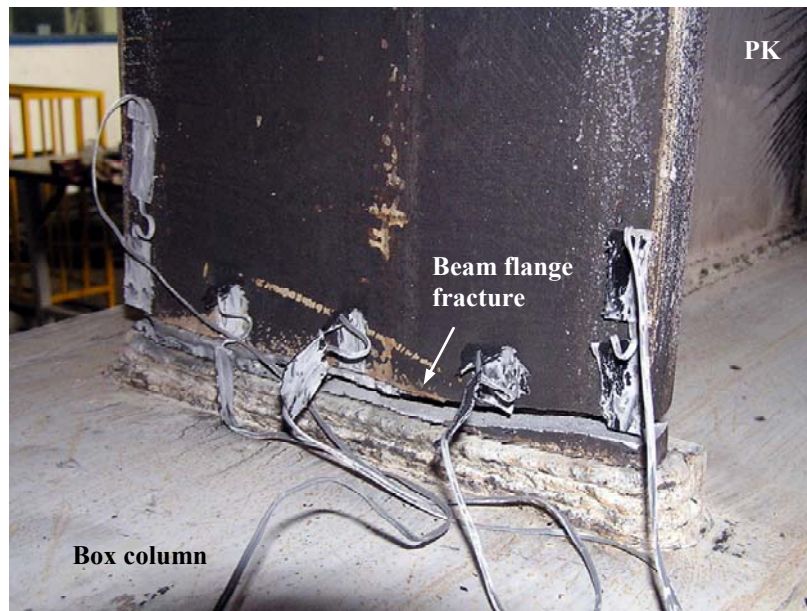


Figure 4.7 Failure mode of typical pre-Kobe specimen PK.

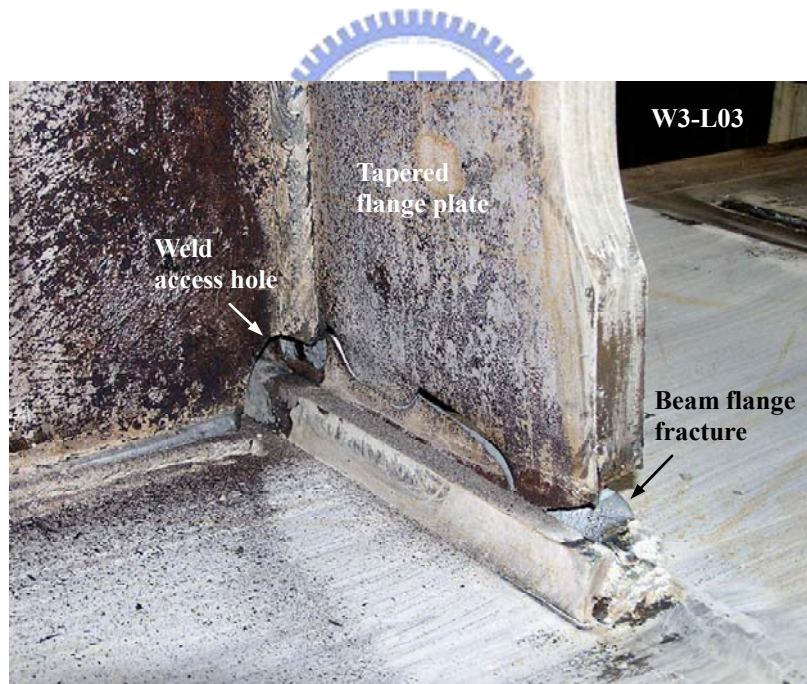


Figure 4.8 Fracture of beam flange groove weld of specimen W3-L03 at 4% rad story drift angle.



Figure 4.9 Plastic hinge formation followed by local buckling at 5% rad story drift angle: (a) specimen W1-L05; (b) specimen W1-L03.



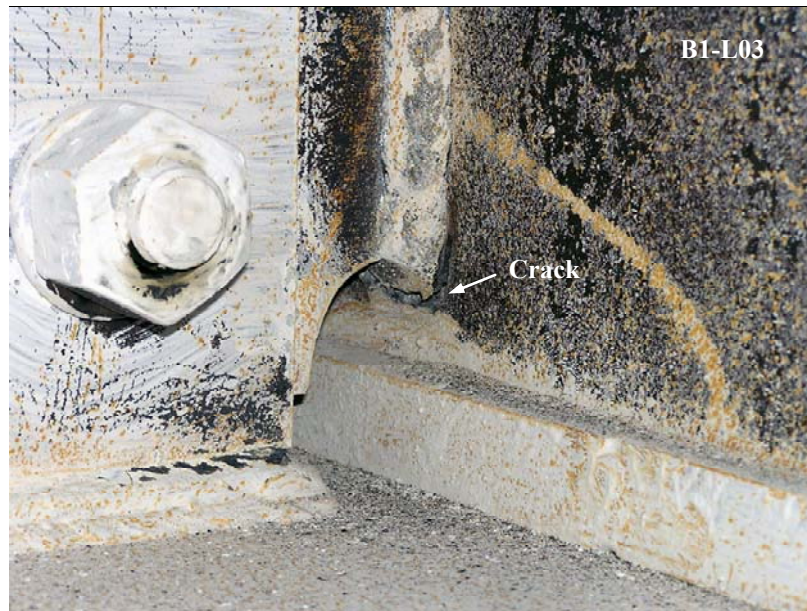
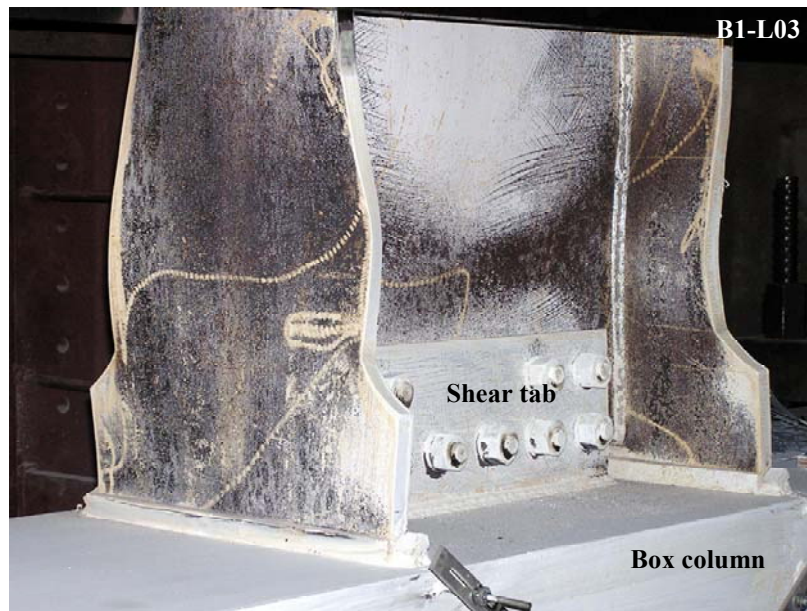


Figure 4.10 Slight cracking at root of weld access hole of specimen B1-L03 at 4% rad story drift angle.



(a)



(b)

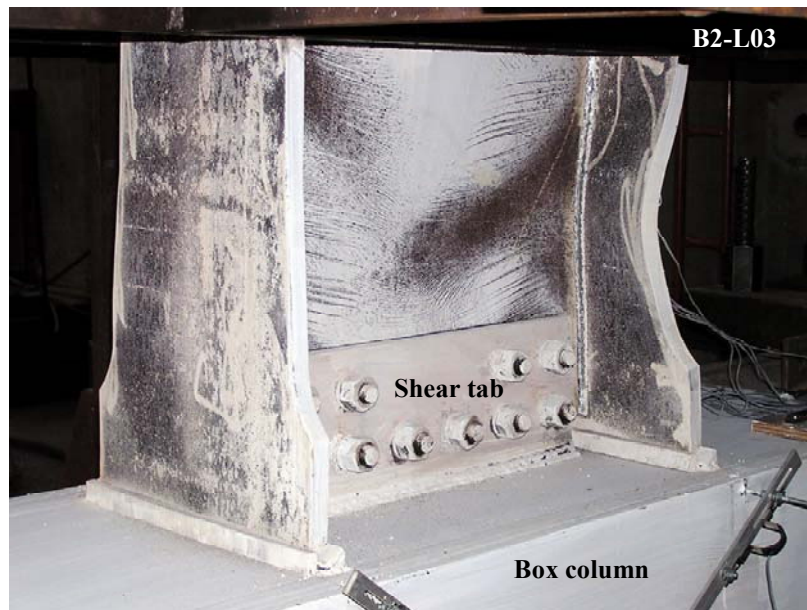


Figure 4.11 Local buckling of beam flanges and beam web at 5% rad story drift angle: (a) specimen B1-L03; (b) specimen B2-L03.

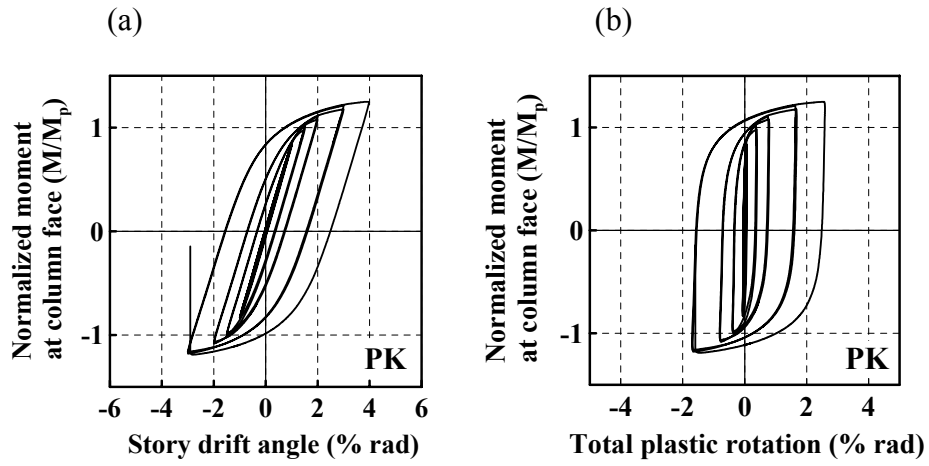


Figure 4.12 Hysteresis response of specimen PK: (a) normalized moment at column face versus story drift angle; (b) normalized moment at column face versus total plastic rotation.



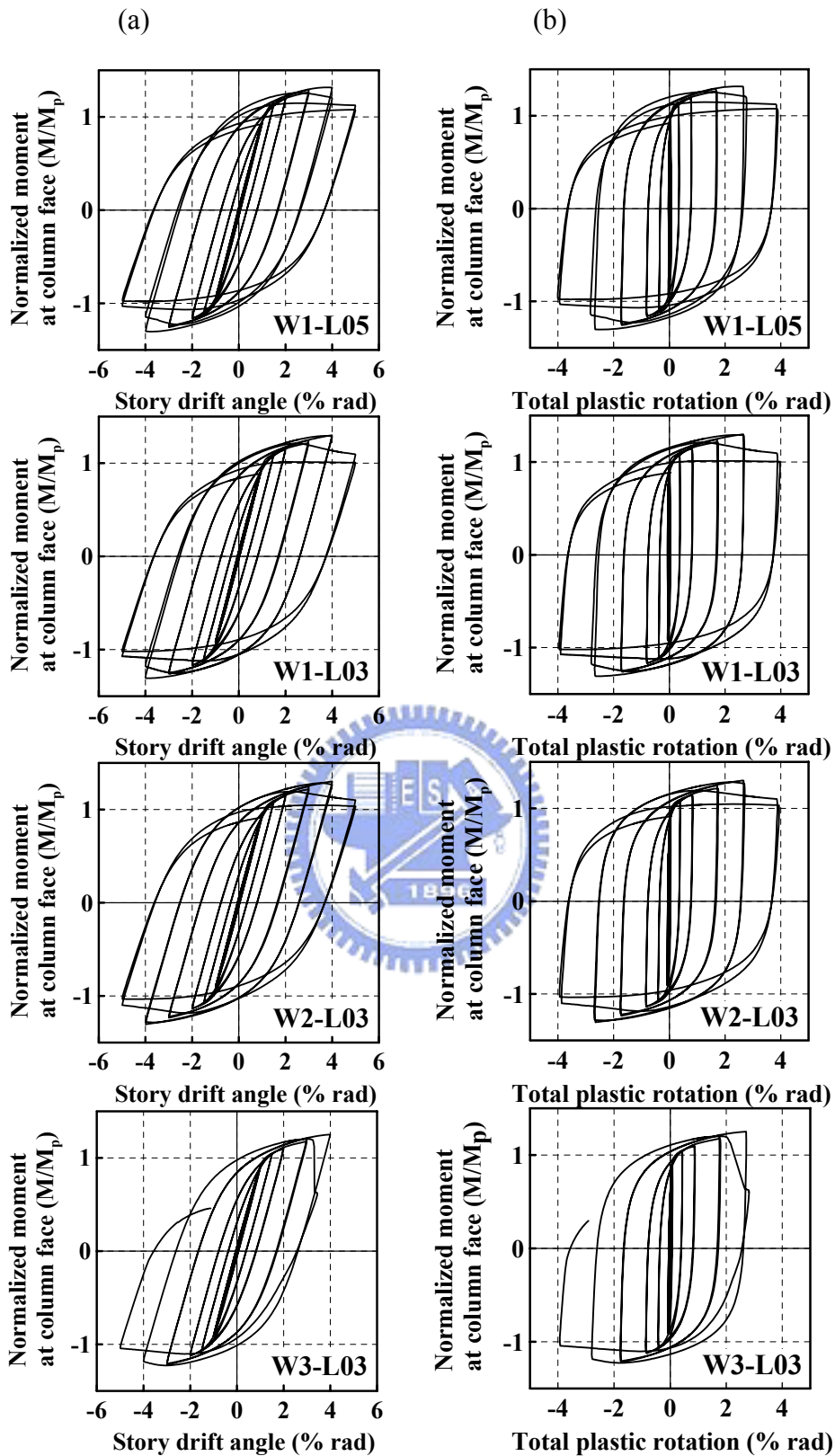


Figure 4.13 Normalized moment versus rotation responses of column-tree tapered flange connection specimens: (a) in terms of story drift angle; (b) in terms of total plastic rotation.

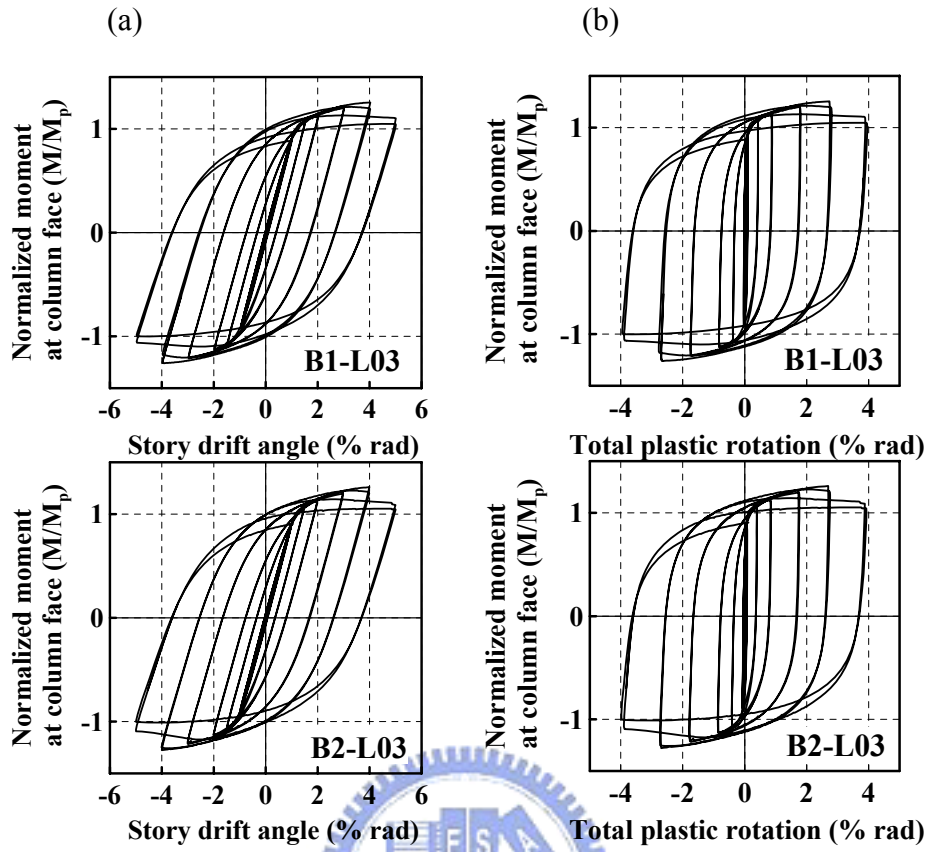


Figure 4.14 Normalized moment versus rotation responses of web-bolted flange-welded tapered flange connection specimens: (a) in terms of story drift angle; (b) in terms of total plastic rotation.

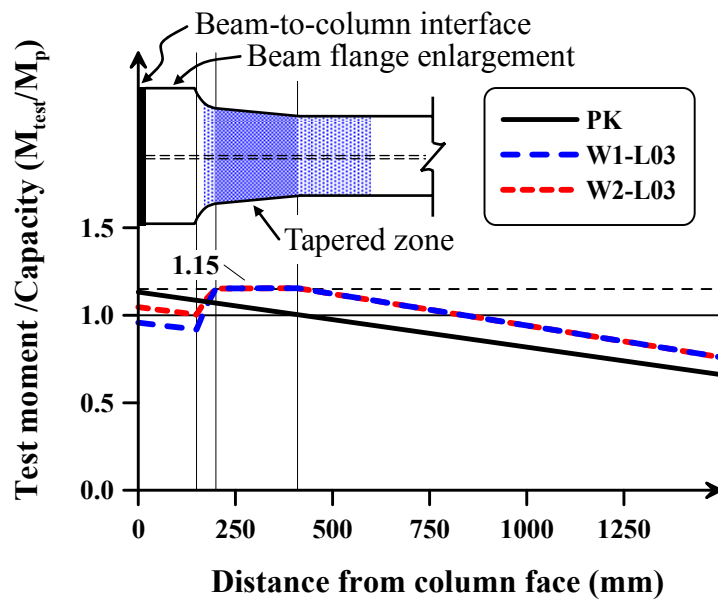


Figure 4.15 Ratios of maximum test moment to calculated moment capacity of the specimens PK, W1-L03, and W2-L03 along the length of the beam.



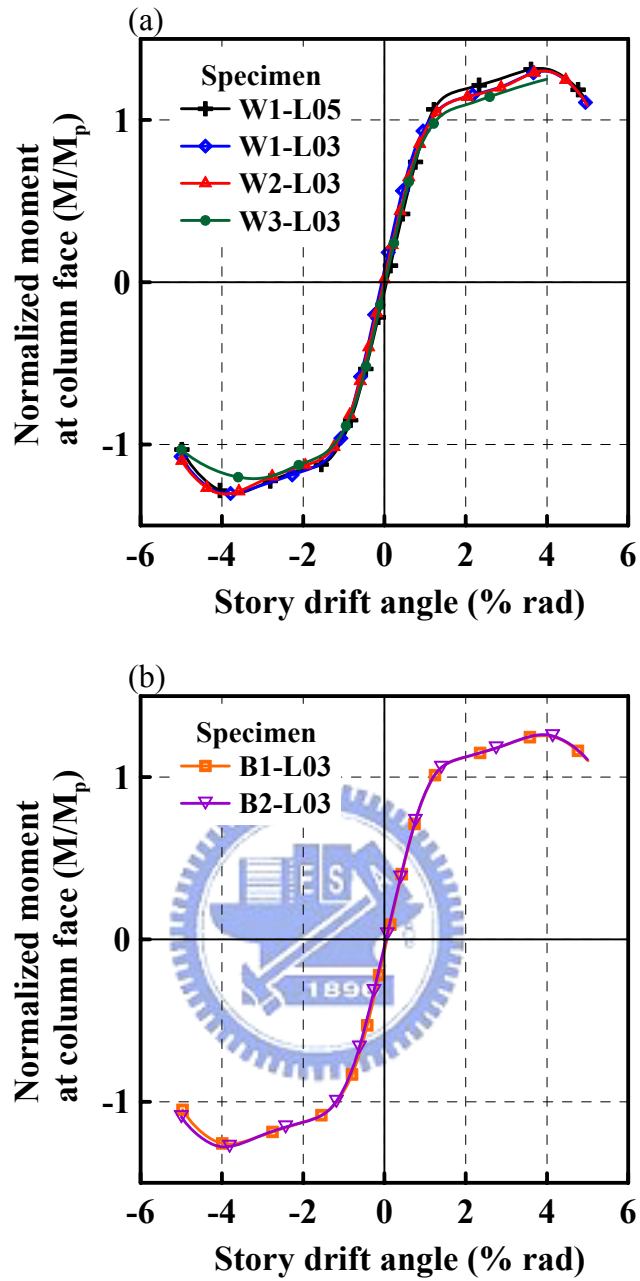


Figure 4.16 Envelope relationships of normalized moment versus story drift angle: (a) specimens with column-tree connection; (b) specimens with web-bolted flange-welded connection.

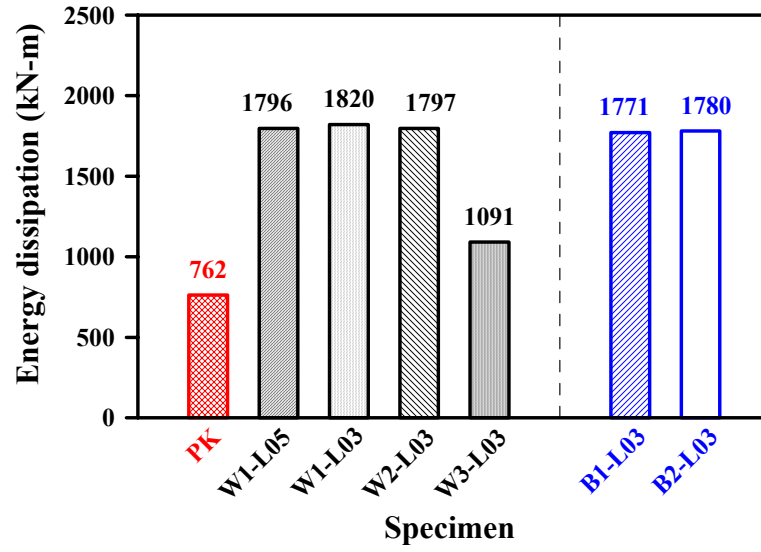


Figure 4.17 Comparison of test specimen energy dissipation.

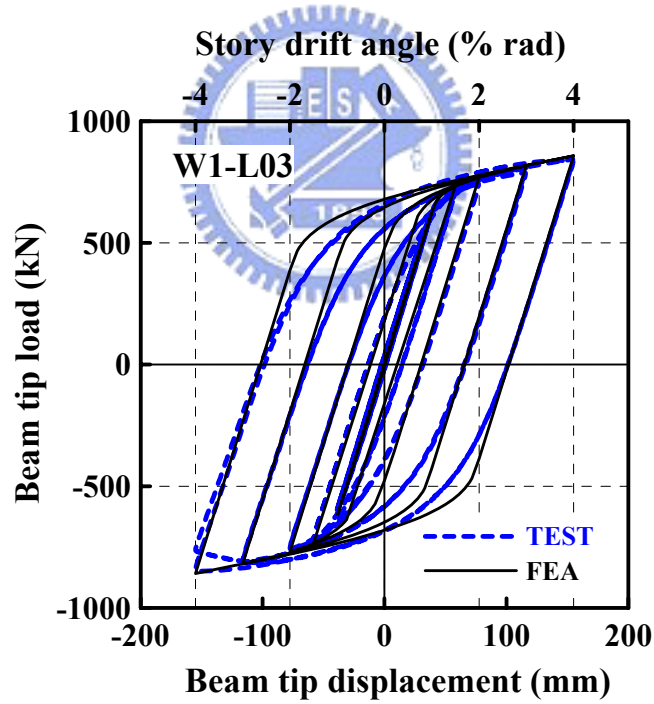


Figure 5.1 Comparison of experimental and analytical beam tip load versus beam tip displacement response of specimen W1-L03.



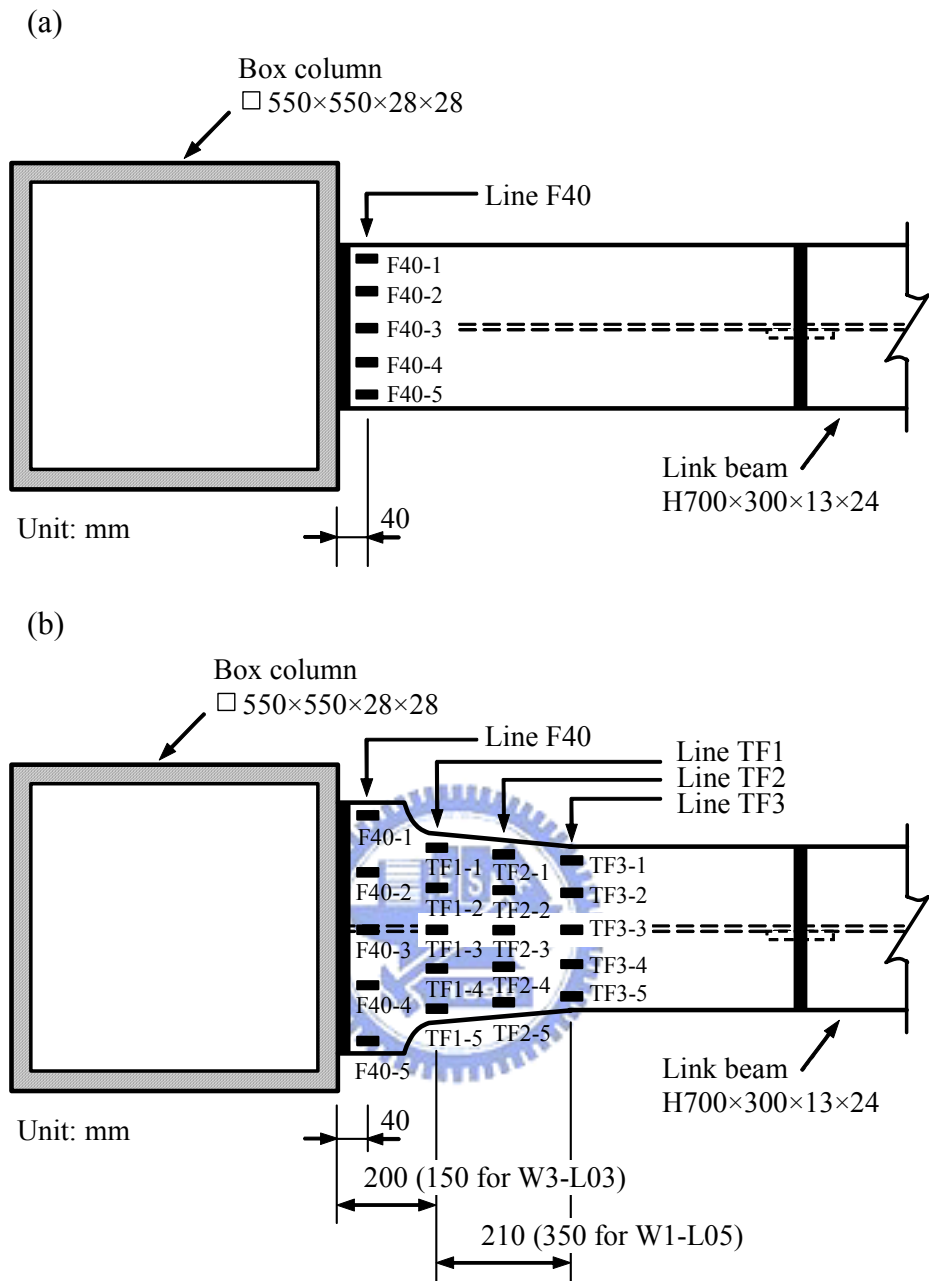


Figure 5.2 Position of strain gauges: (a) specimen PK; (b) tapered flange specimens.

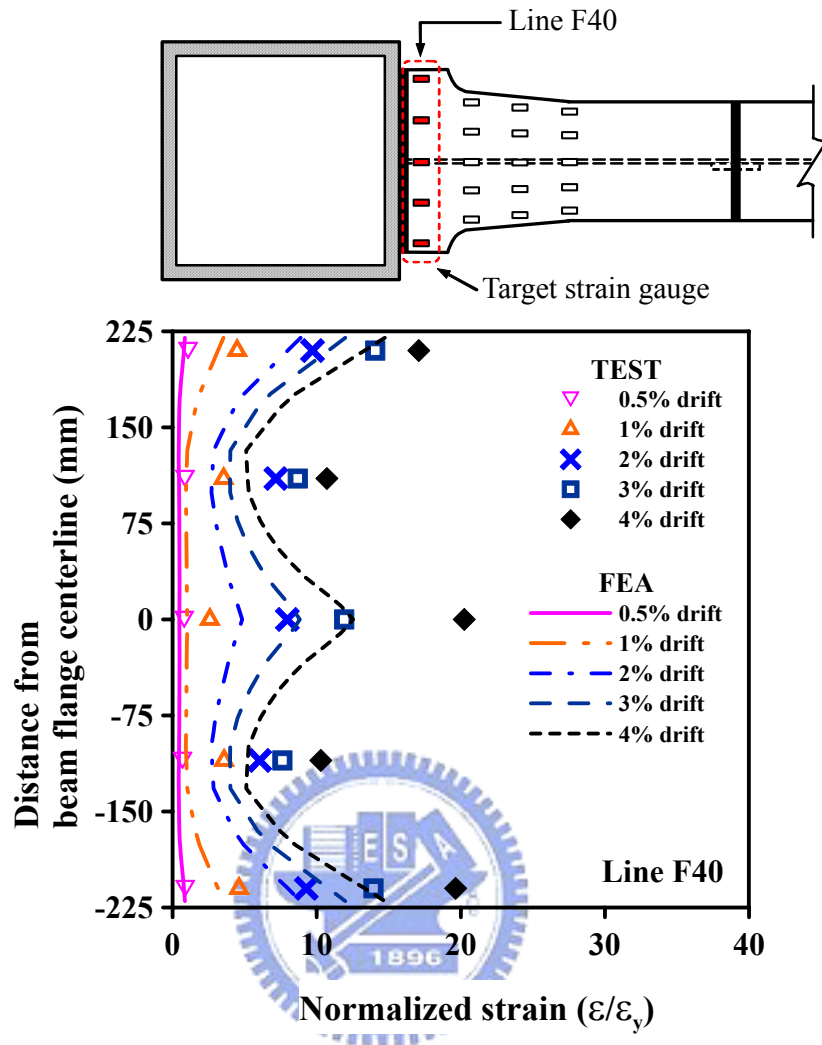


Figure 5.3 Verification of longitudinal strain distributions at line F40 for specimen W1-L03.

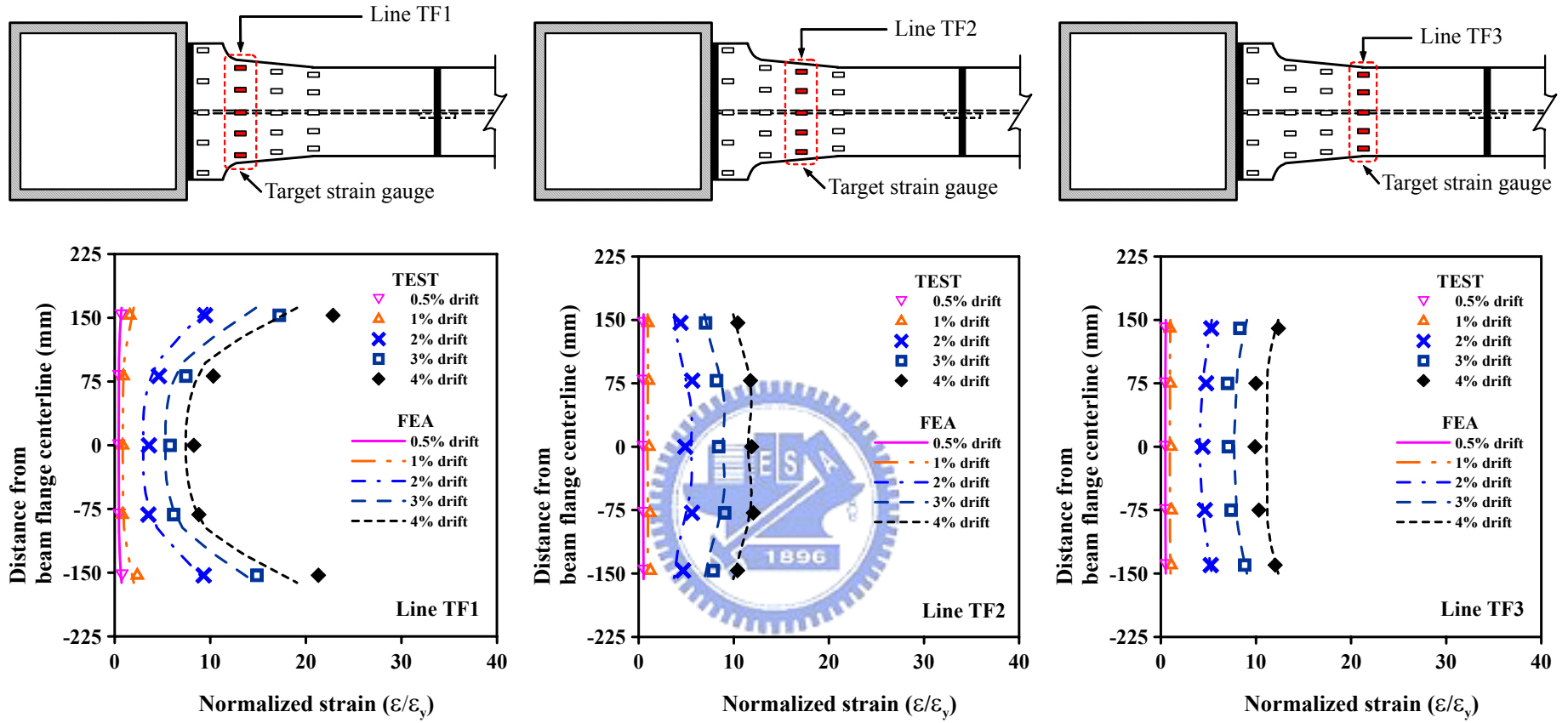


Figure 5.4 Verification of longitudinal strain distributions around tapered zone of beam flange for specimen W1-L03.

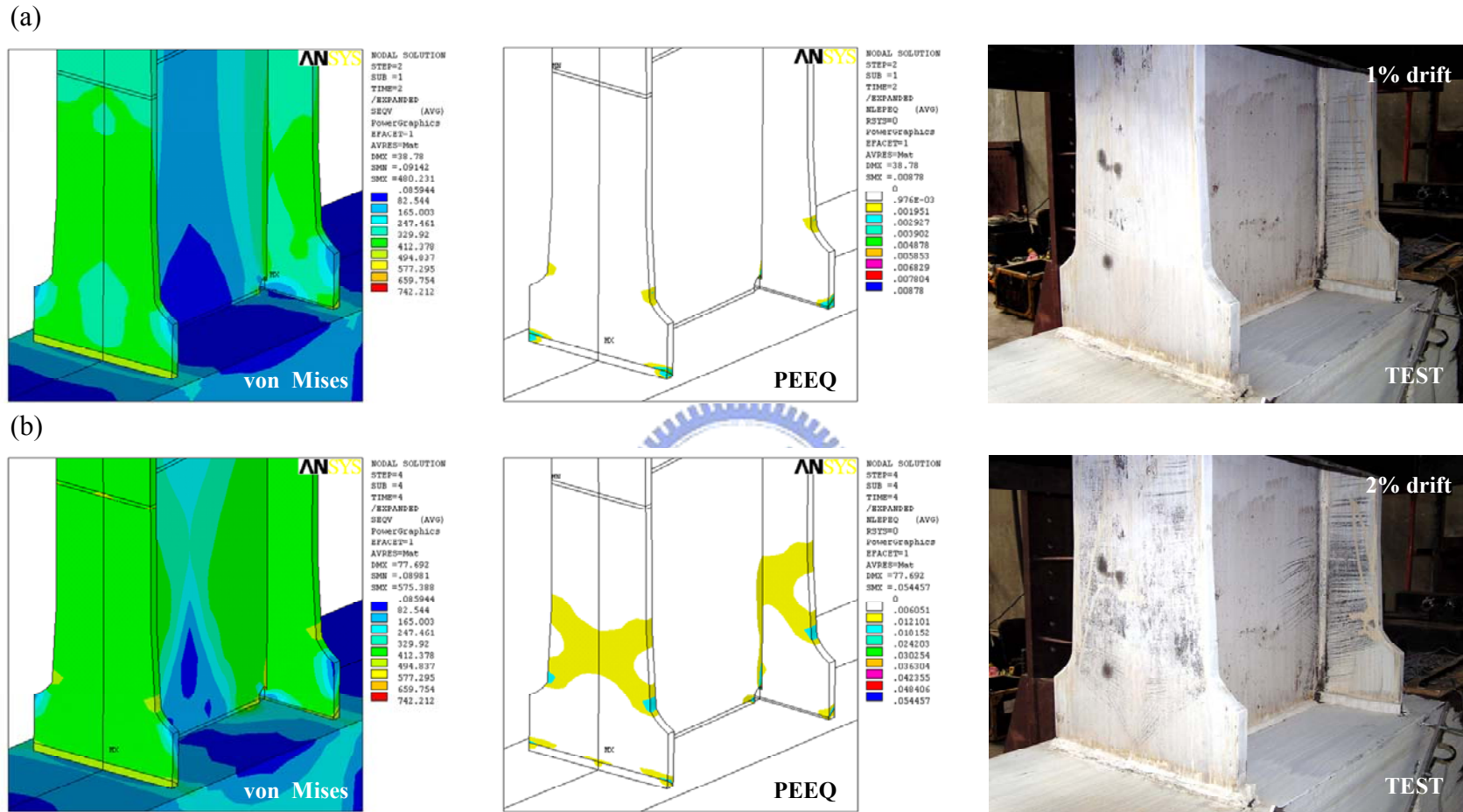


Figure 5.5 Von Mises stress contours, equivalent plastic strain contours, and yielding behavior during testing of specimen W1-L03: (a) at 1% rad story drift angle; (b) at 2% rad story drift angle.

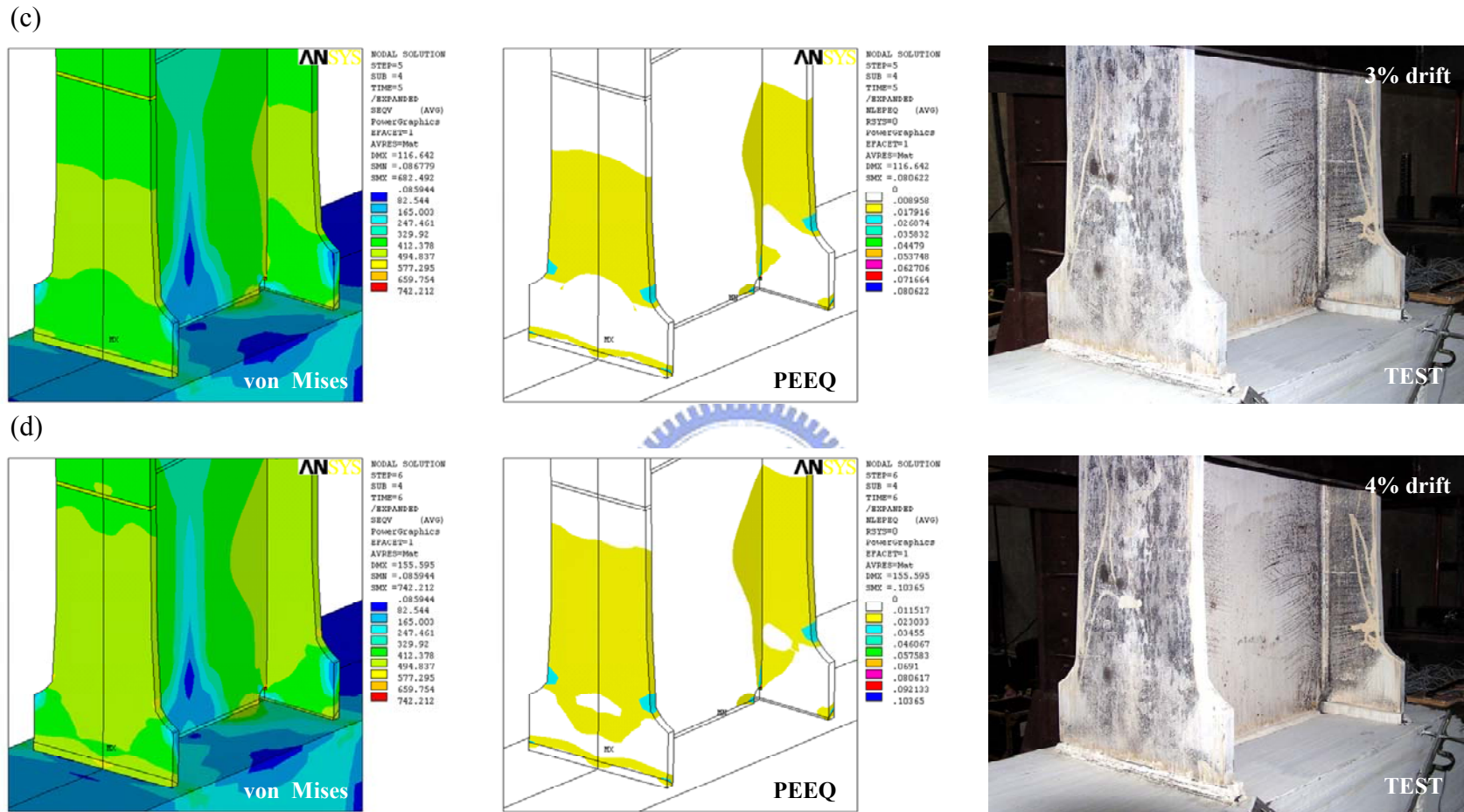


Figure 5.5 (continued) Von Mises stress contours, equivalent plastic strain contours, and yielding behavior during testing of specimen W1-L03: (c) at 3% rad story drift angle; (d) at 4% rad story drift angle.

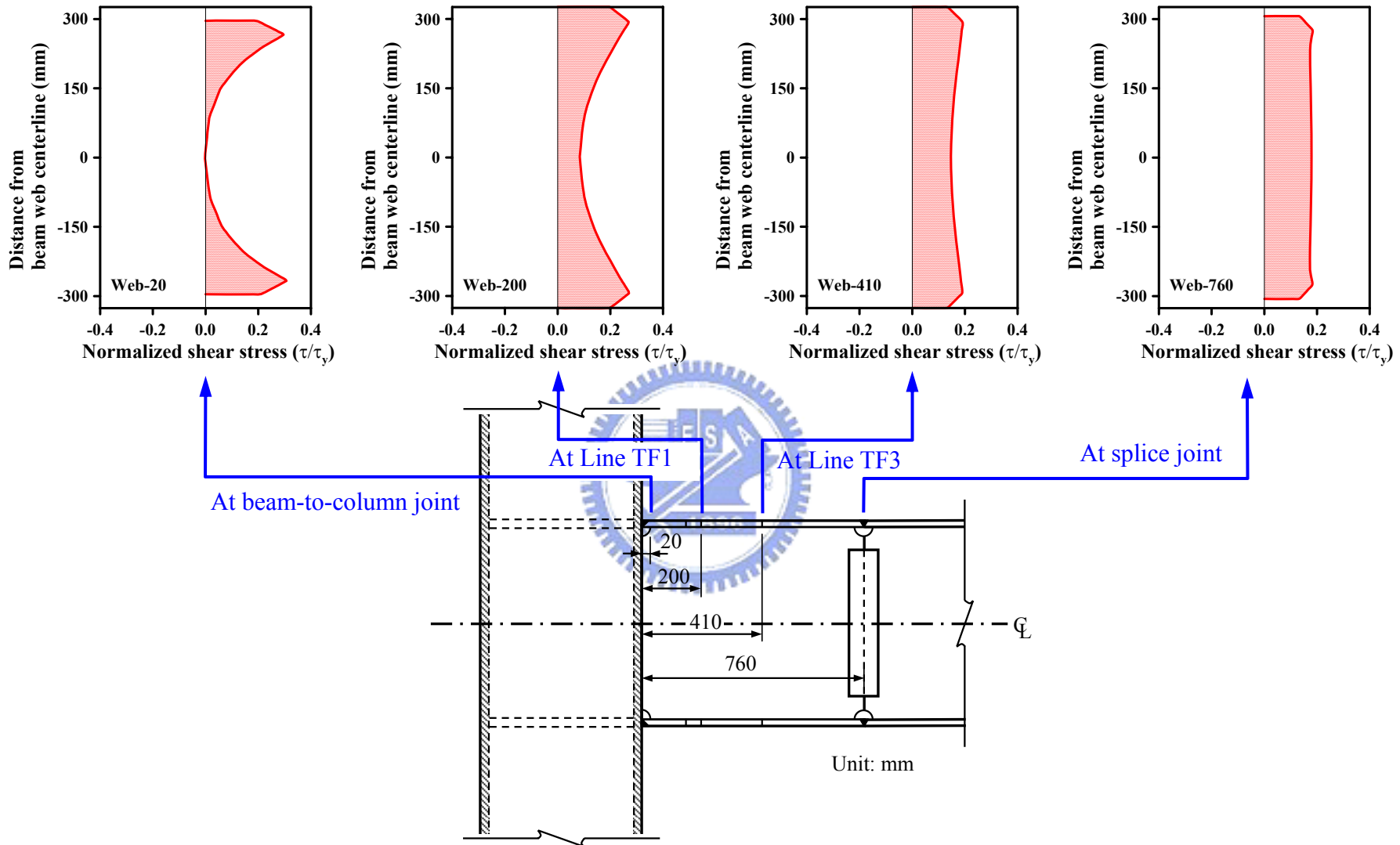


Figure 5.6 Normalized shear stress distributions along beam web depth at 0.5% rad story drift angle.

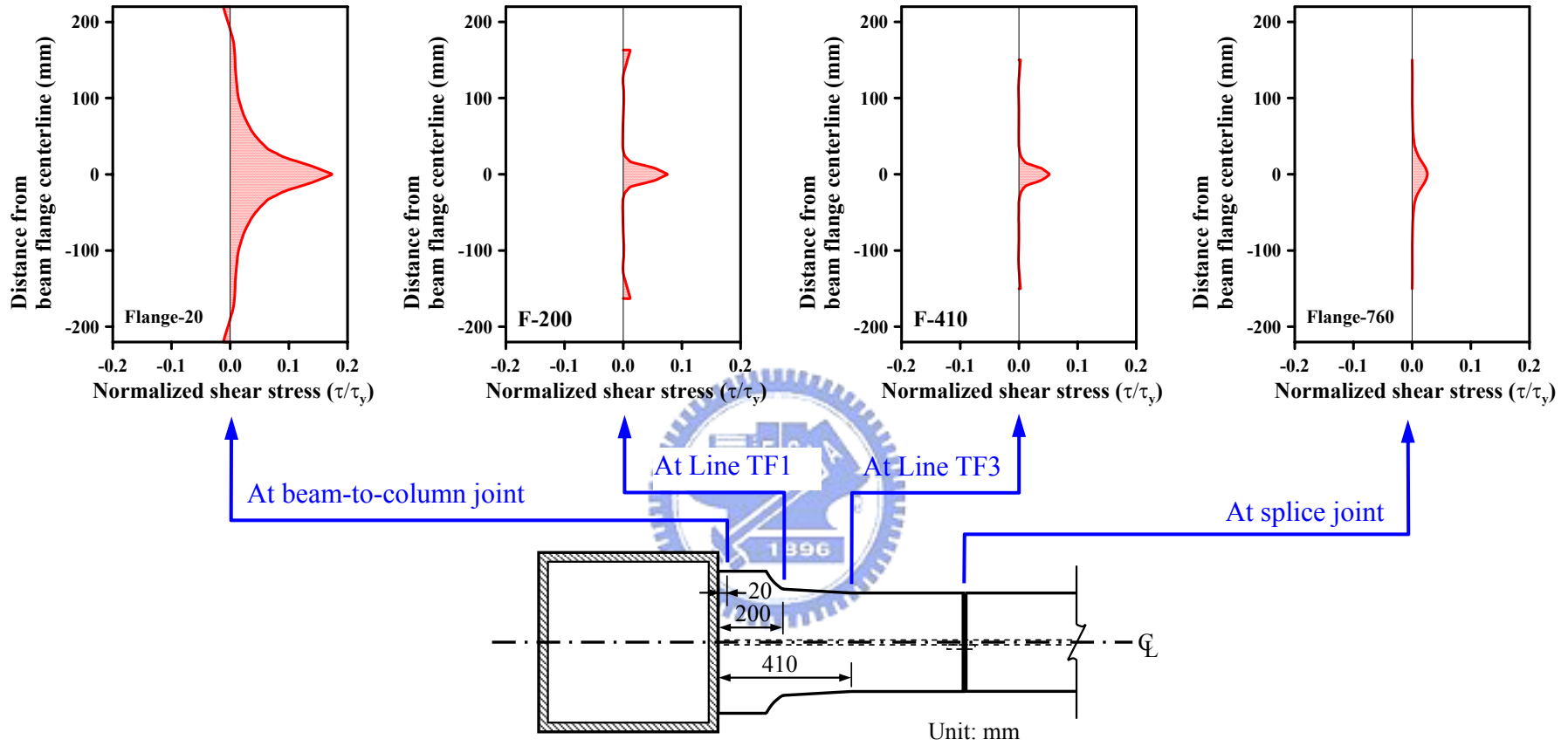


Figure 5.7 Normalized shear stress distributions along beam flange width at 0.5% rad story drift angle.

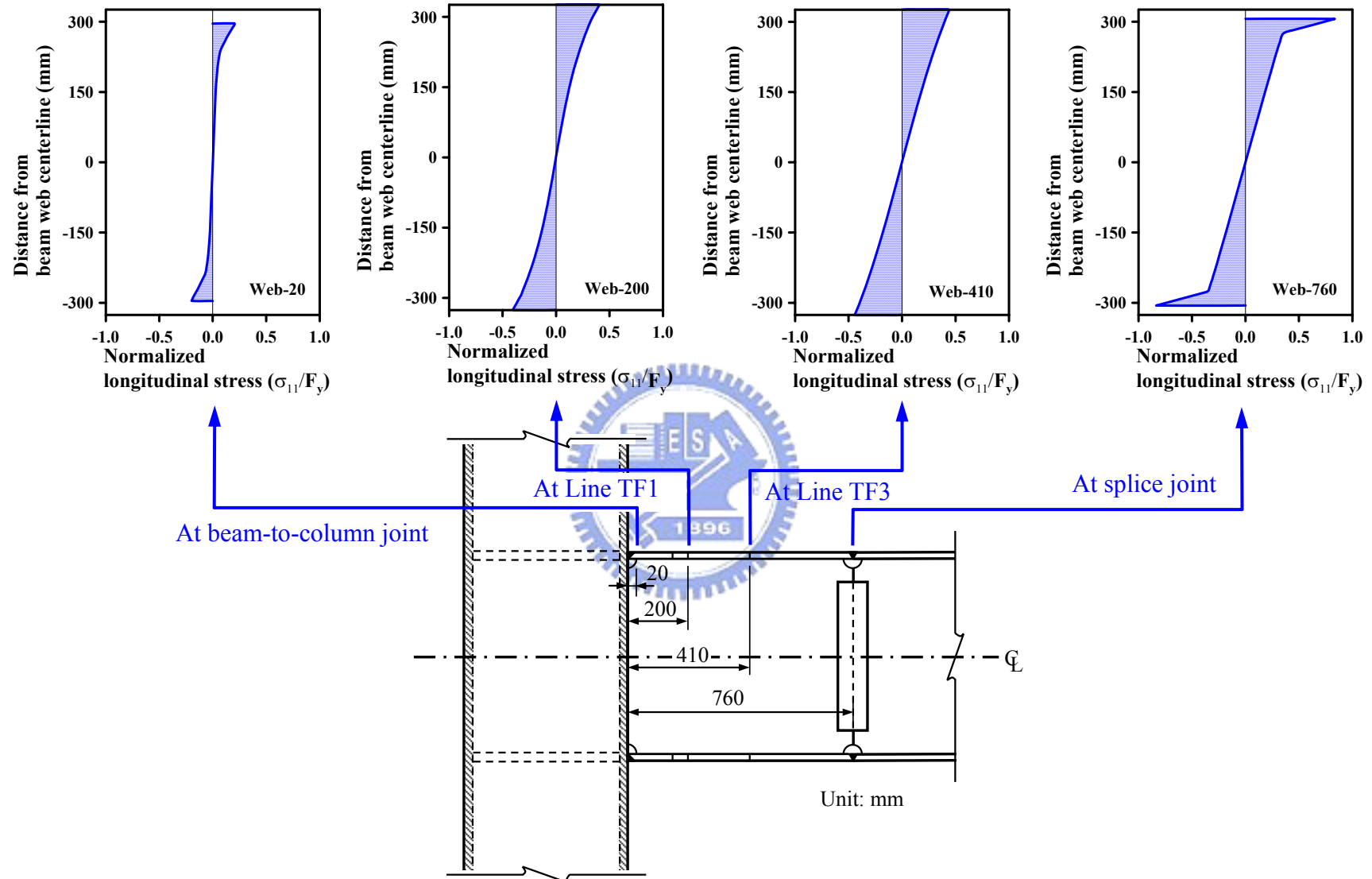


Figure 5.8 Normalized longitudinal stress distributions along beam web depth at 0.5% rad story drift angle.



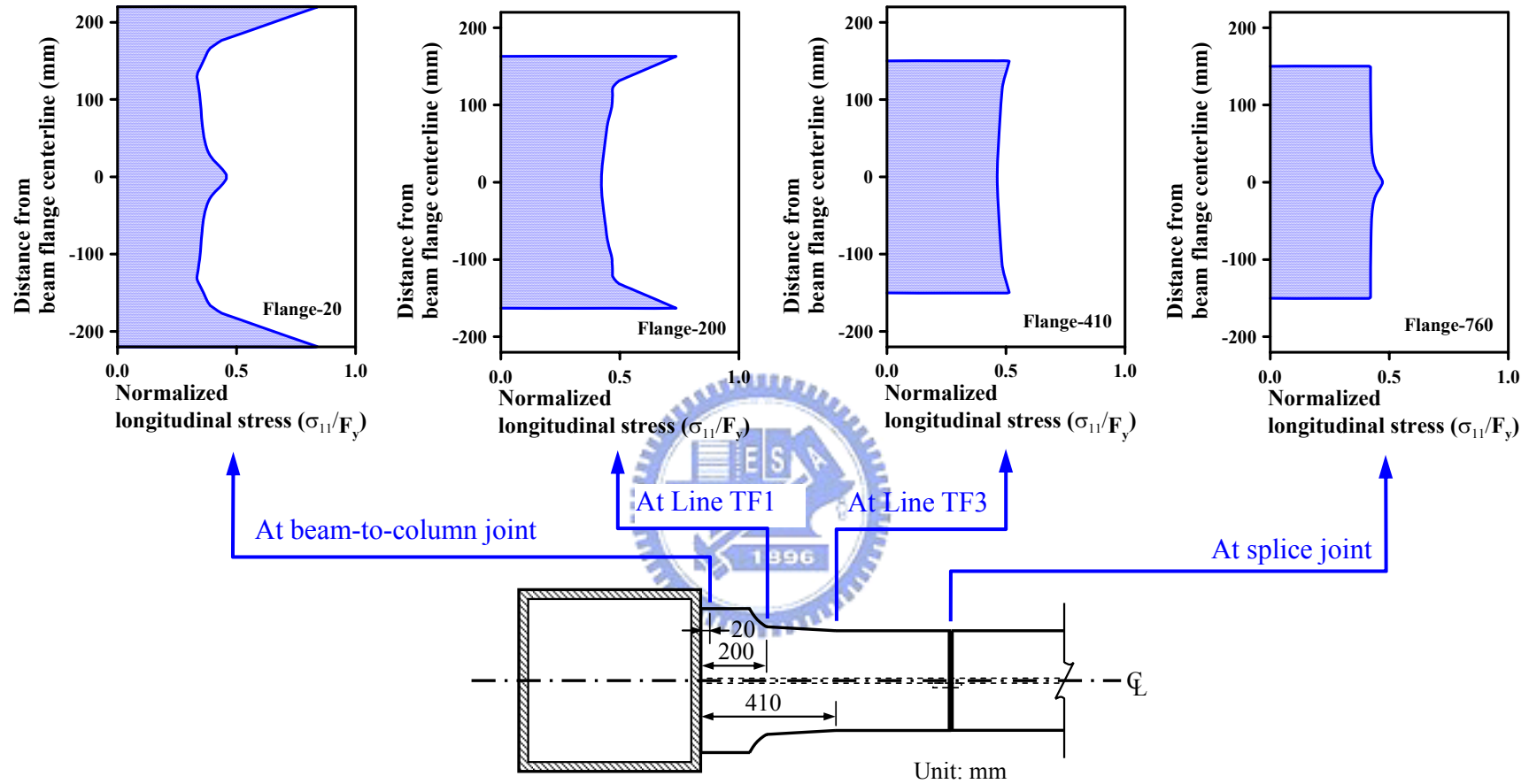


Figure 5.9 Normalized longitudinal stress distributions along beam flange width at 0.5% rad story drift angle.

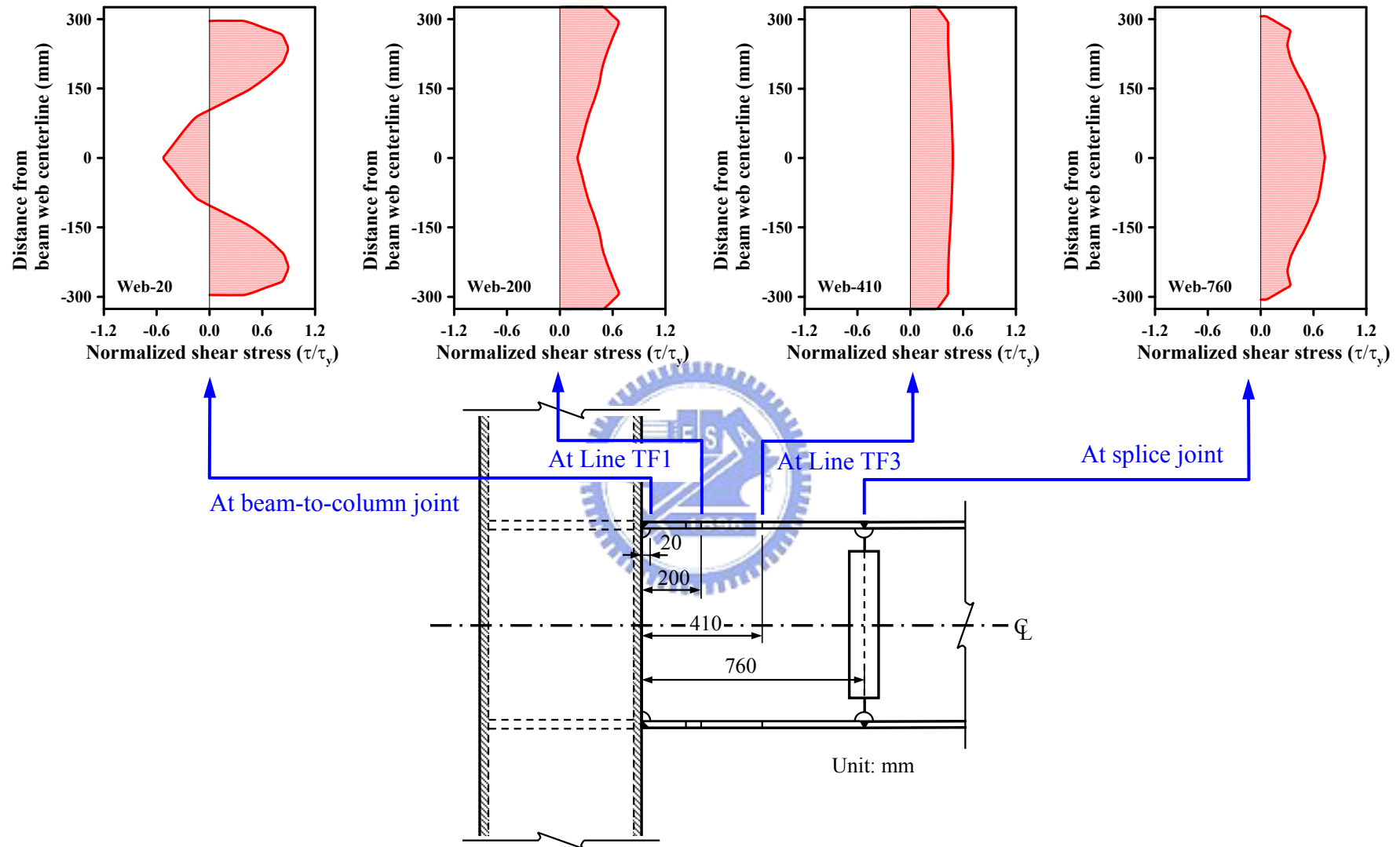


Figure 5.10 Normalized shear stress distributions along beam web depth at 4% rad story drift angle.

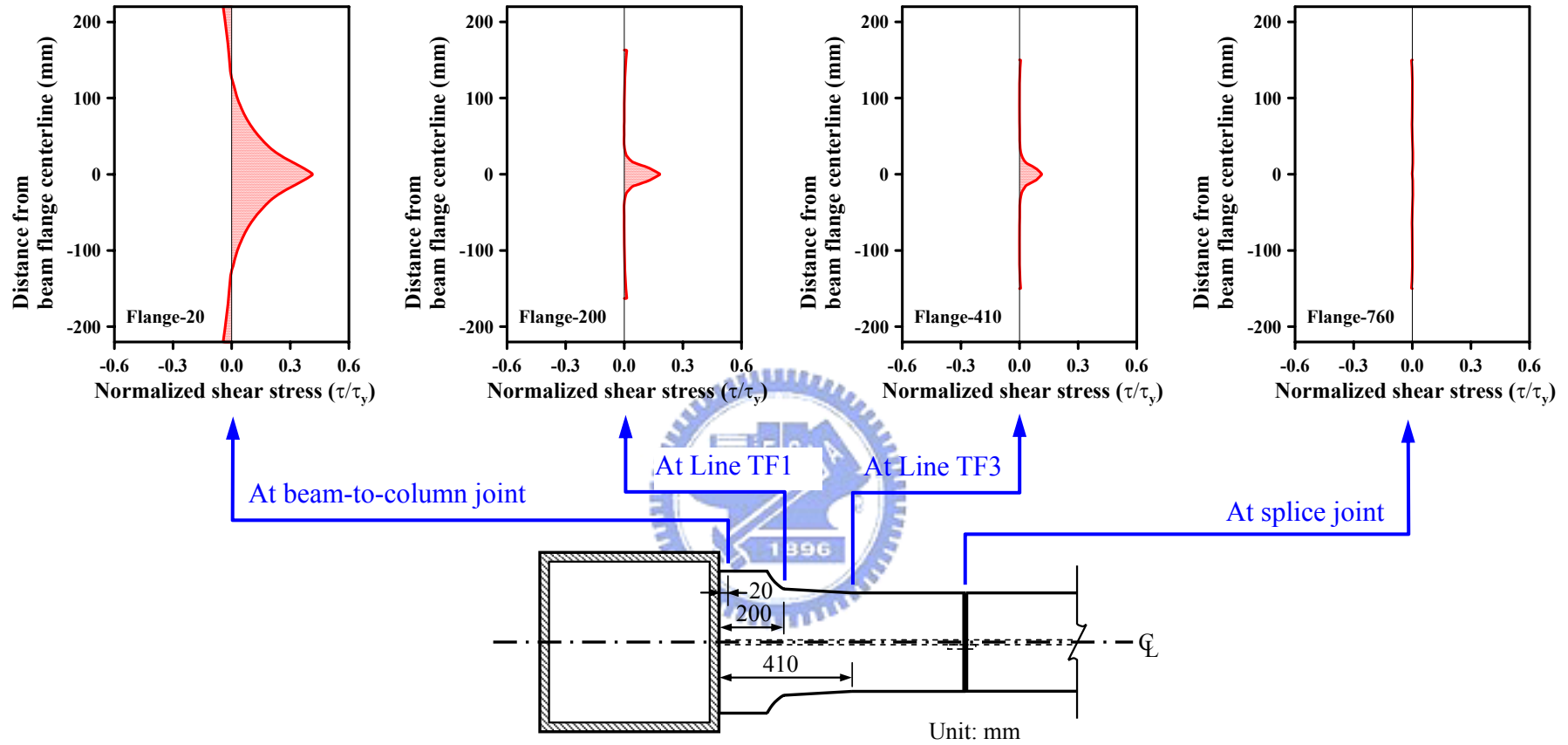


Figure 5.11 Normalized shear stress distributions along beam flange width at 4% rad story drift angle.

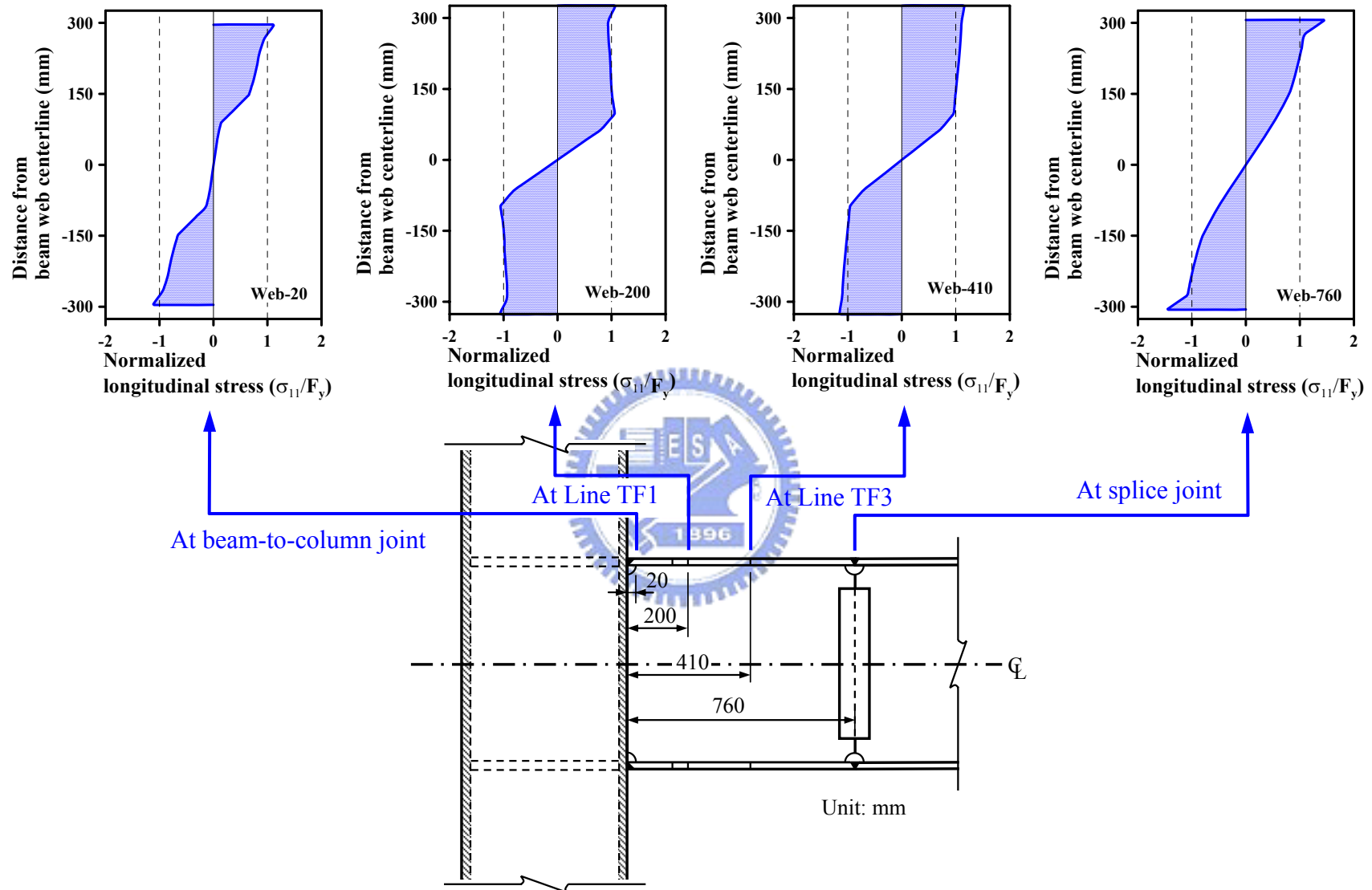


Figure 5.12 Normalized longitudinal stress distributions along beam web depth at 4% rad story drift angle.

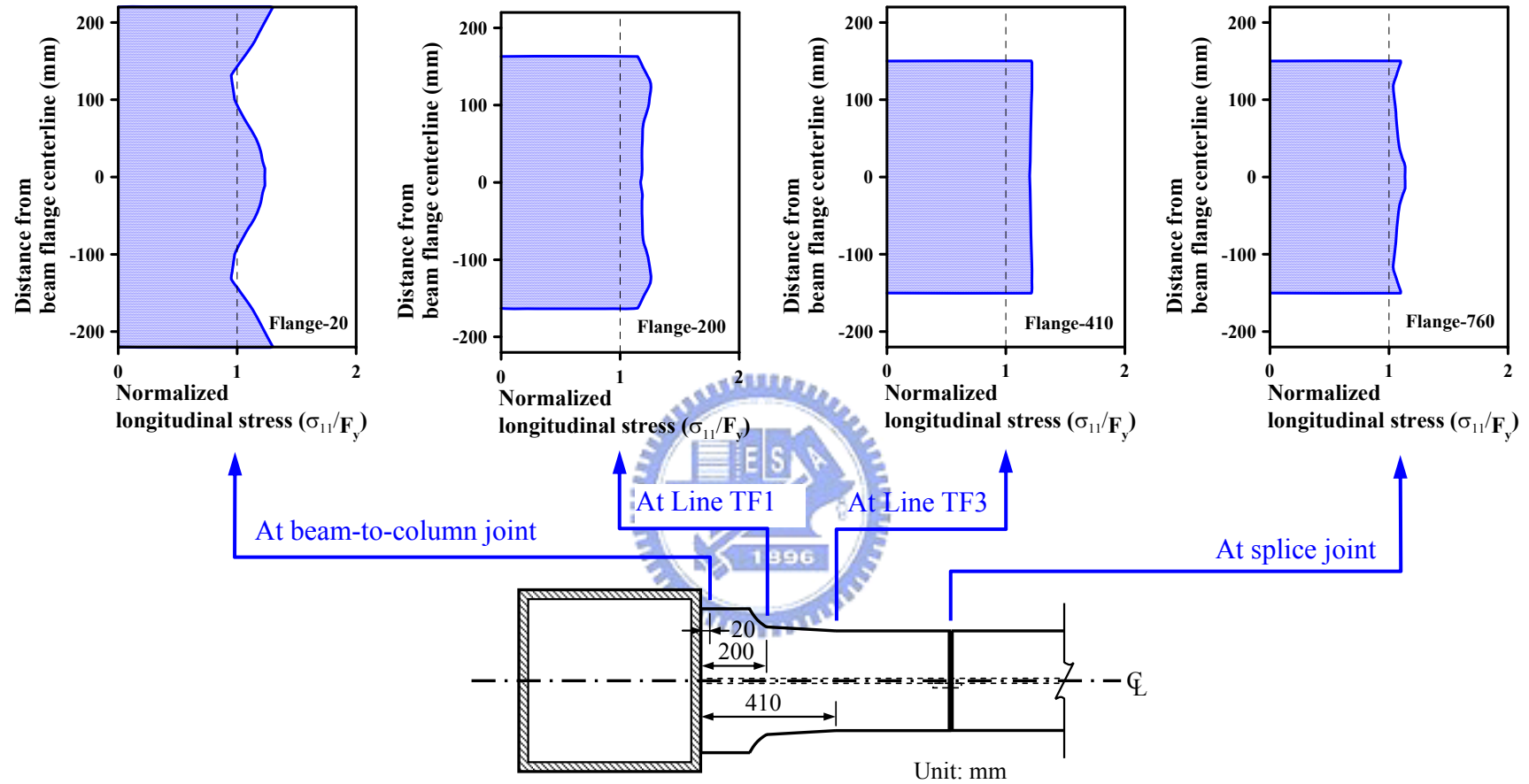


Figure 5.13 Normalized longitudinal stress distributions along beam flange width at 4% rad story drift angle.

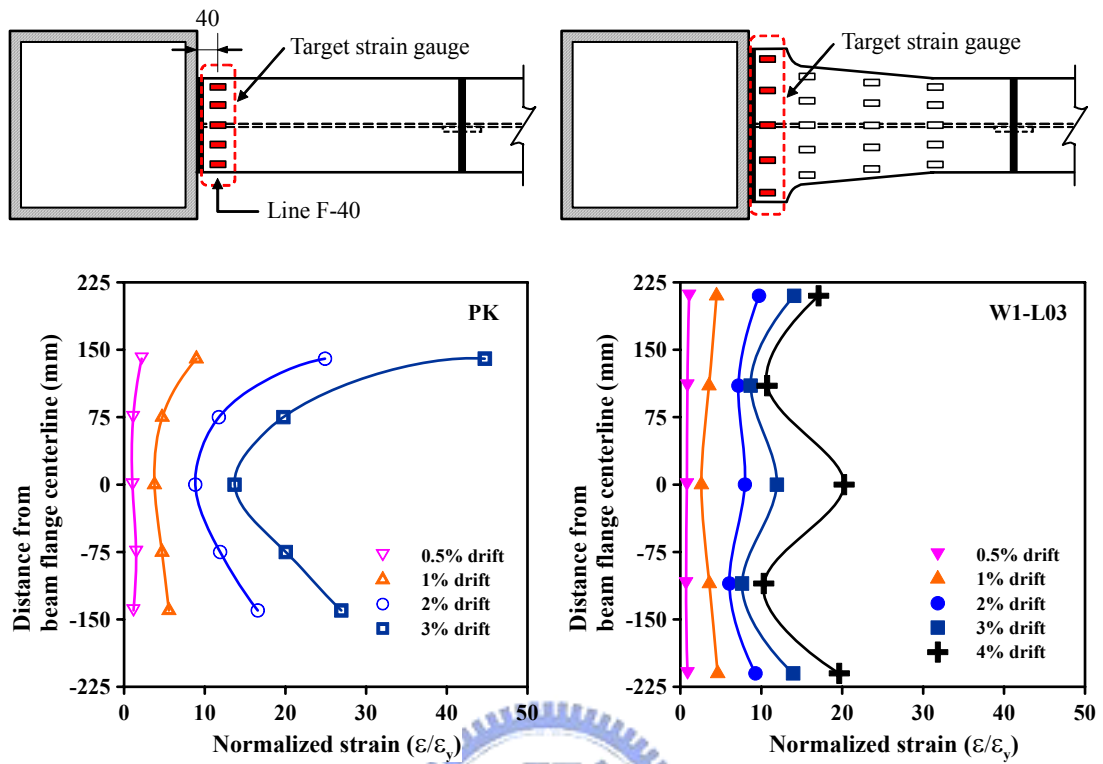


Figure 5.14 Distributions of normalized longitudinal strains along beam flange width at line F-40 between specimens PK and W10-L03.

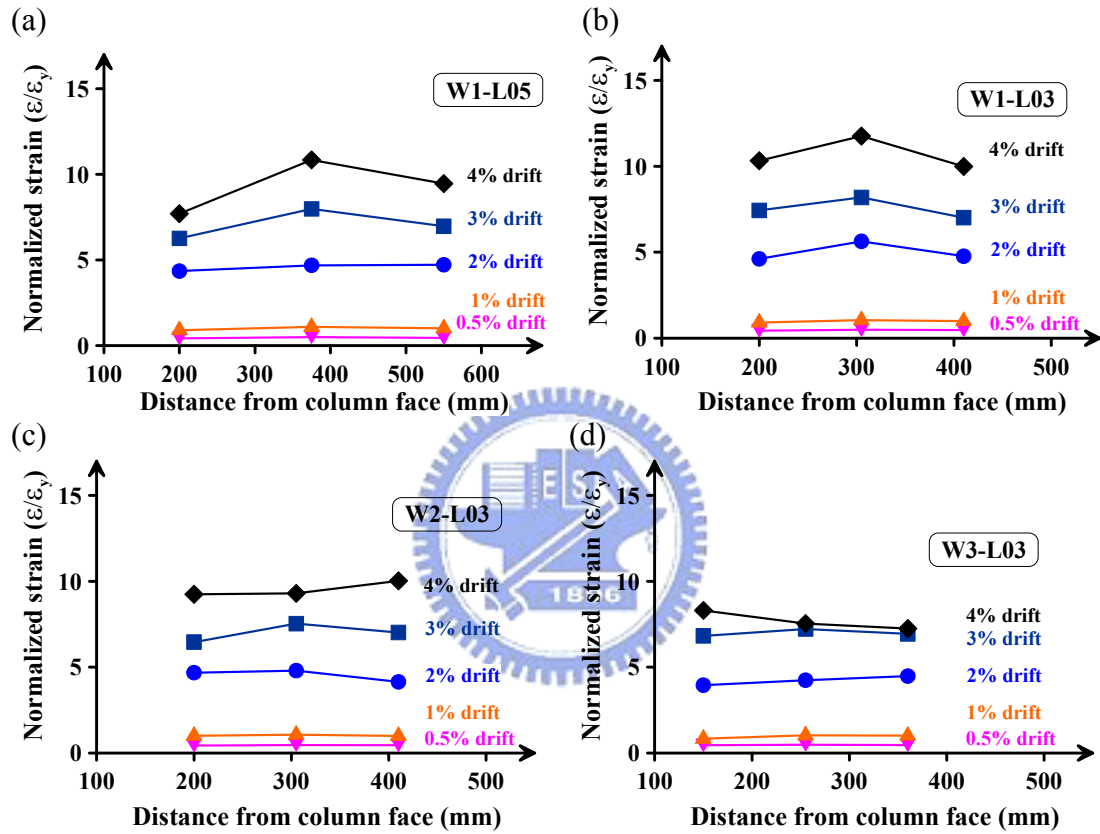
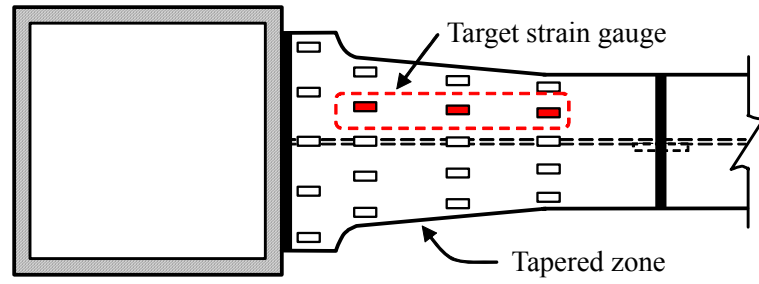


Figure 5.15 Distributions of normalized longitudinal strains across tapered zone of beam flange for column-tree specimens: (a) specimen W1-L05; (b) specimen W1-L03; (c) specimen W2-L03; (d) specimen W3-L03.

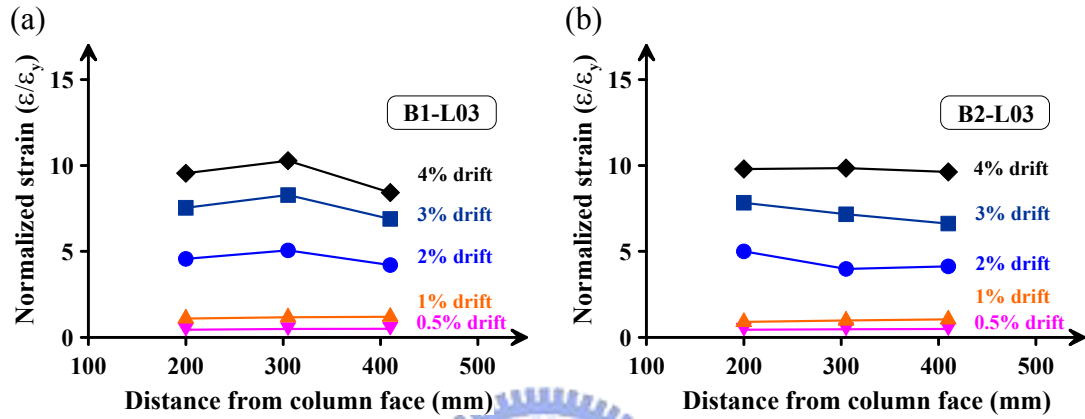
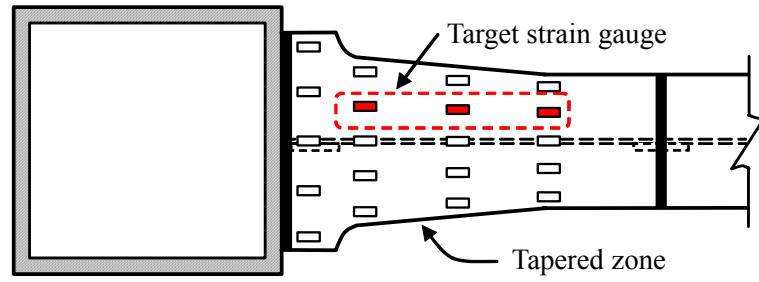


Figure 5.16 Distributions of normalized longitudinal strains across tapered zone of beam flange for web-bolted flange-welded specimens: (a) specimen B1-L03; (b) specimen B2-L03.



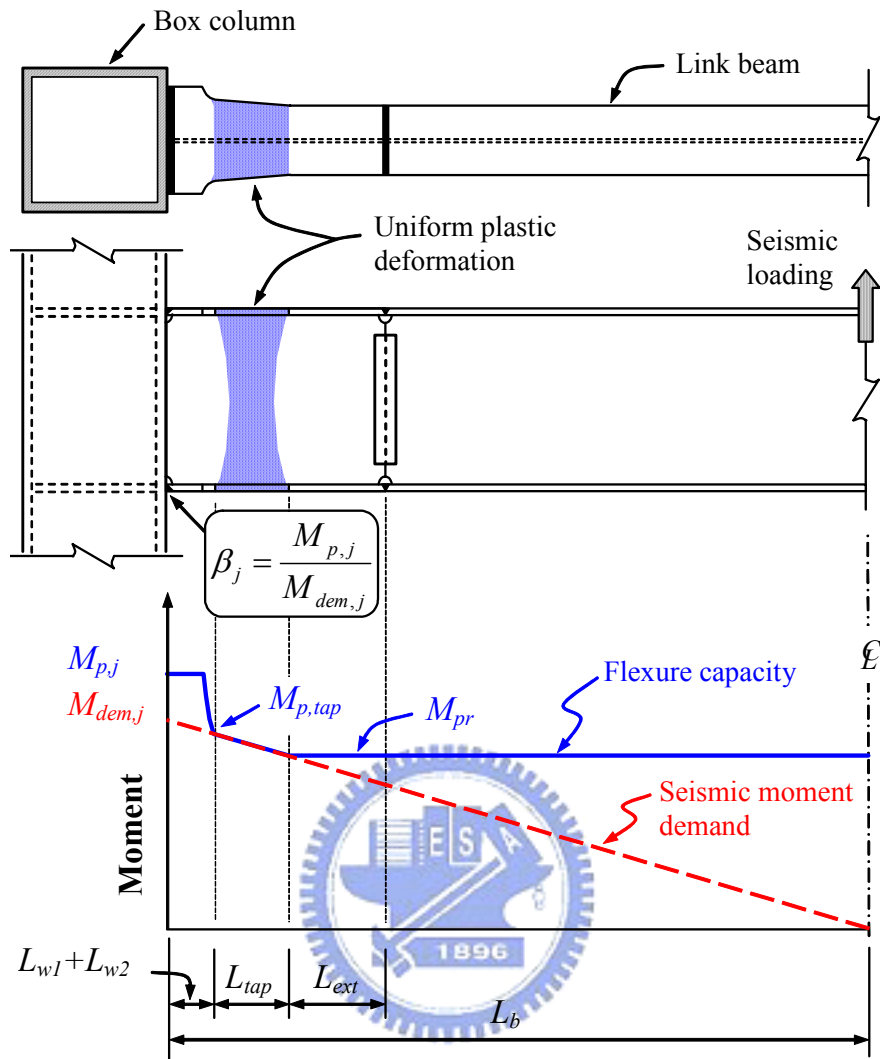


Figure 6.1 Moment gradient of tapered flange connection.

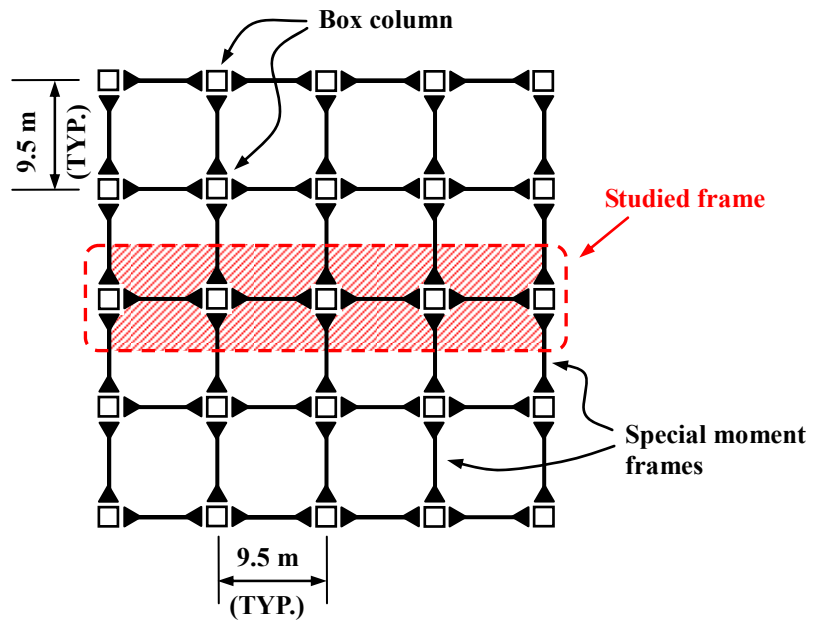


Figure 7.1 Floor plane view of prototype building.



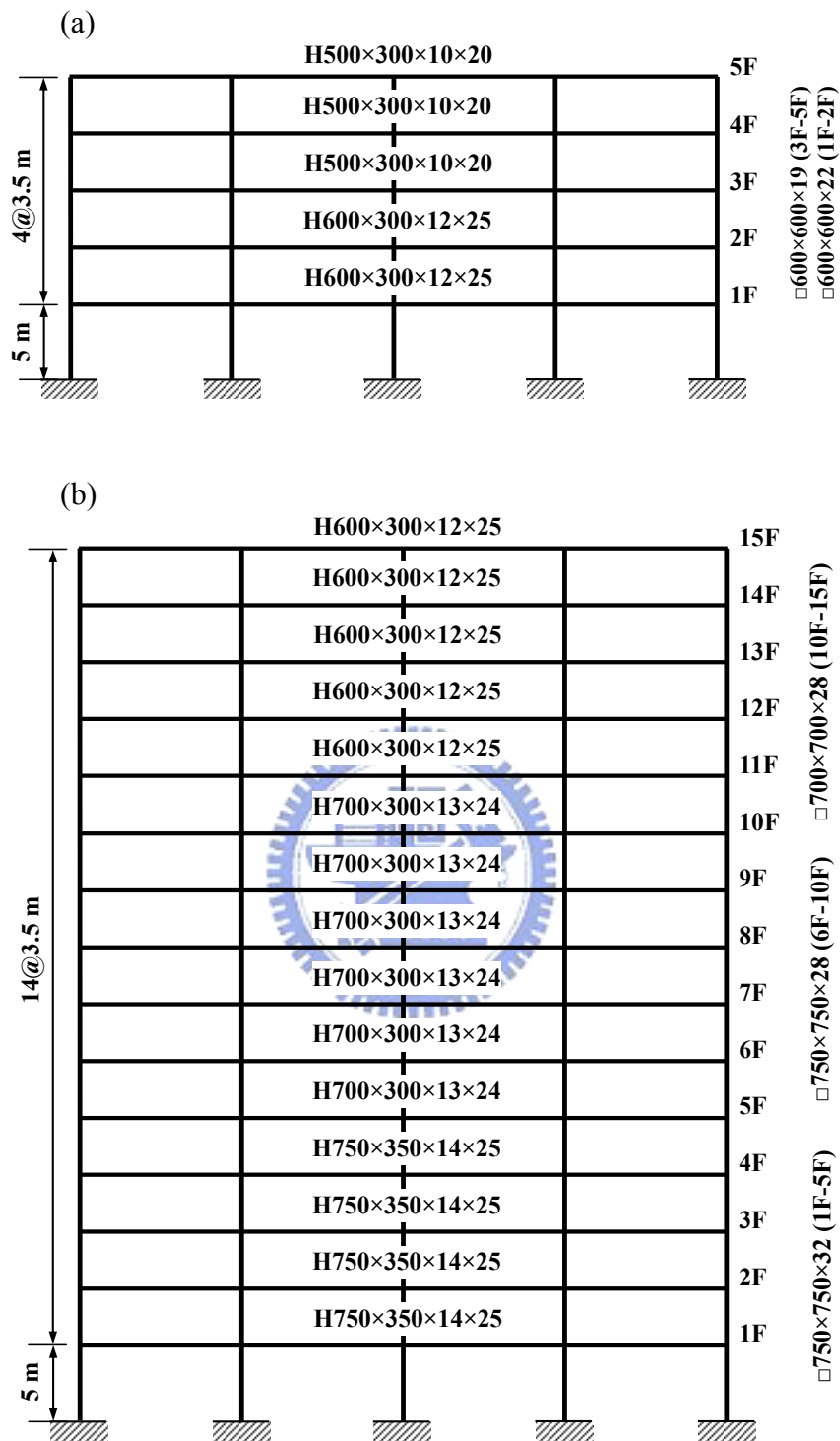


Figure 7.2 Design details of prototype buildings: (a) five-story frame; (b) fifteen-story frame.

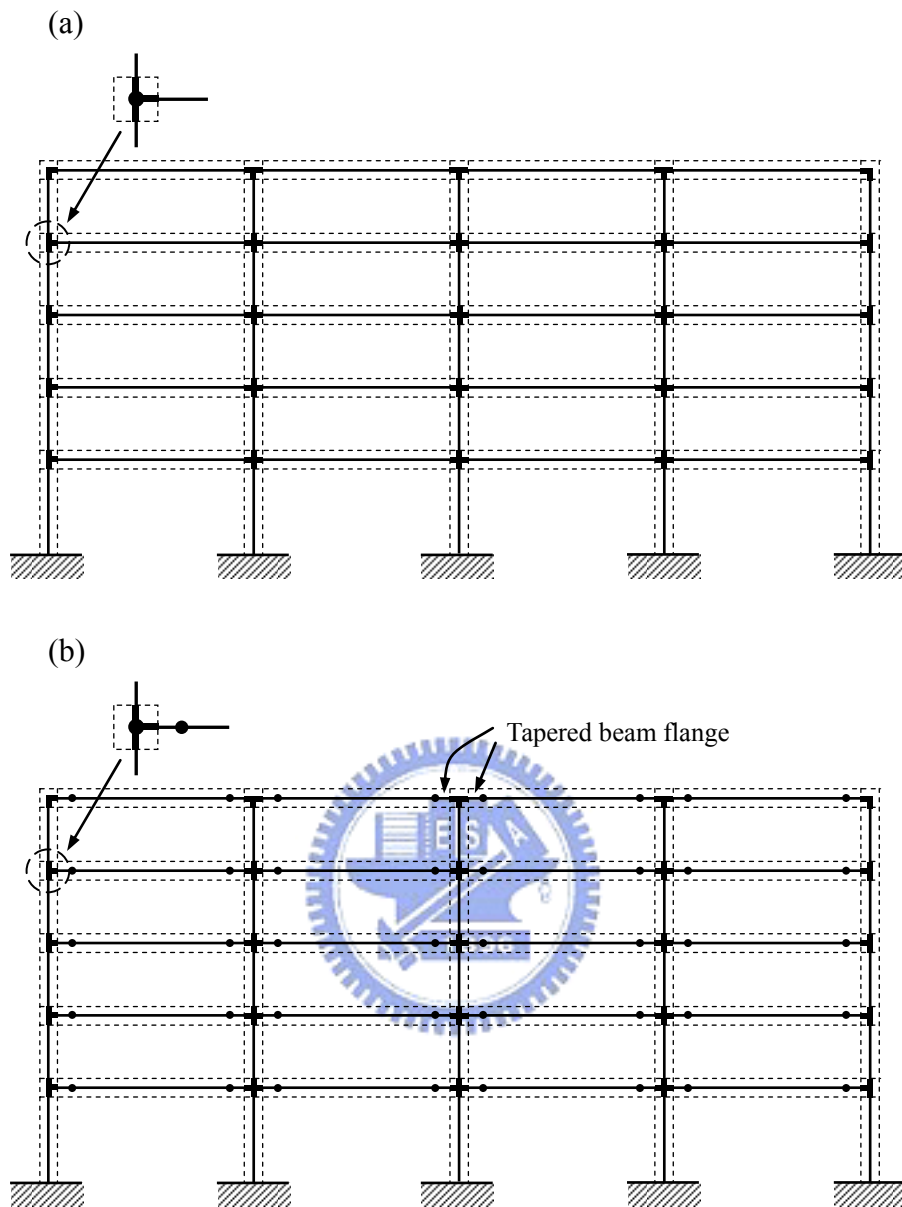


Figure 7.3 Analytical models for prototype buildings: (a) model UR-5F; (b) model TF-5F.

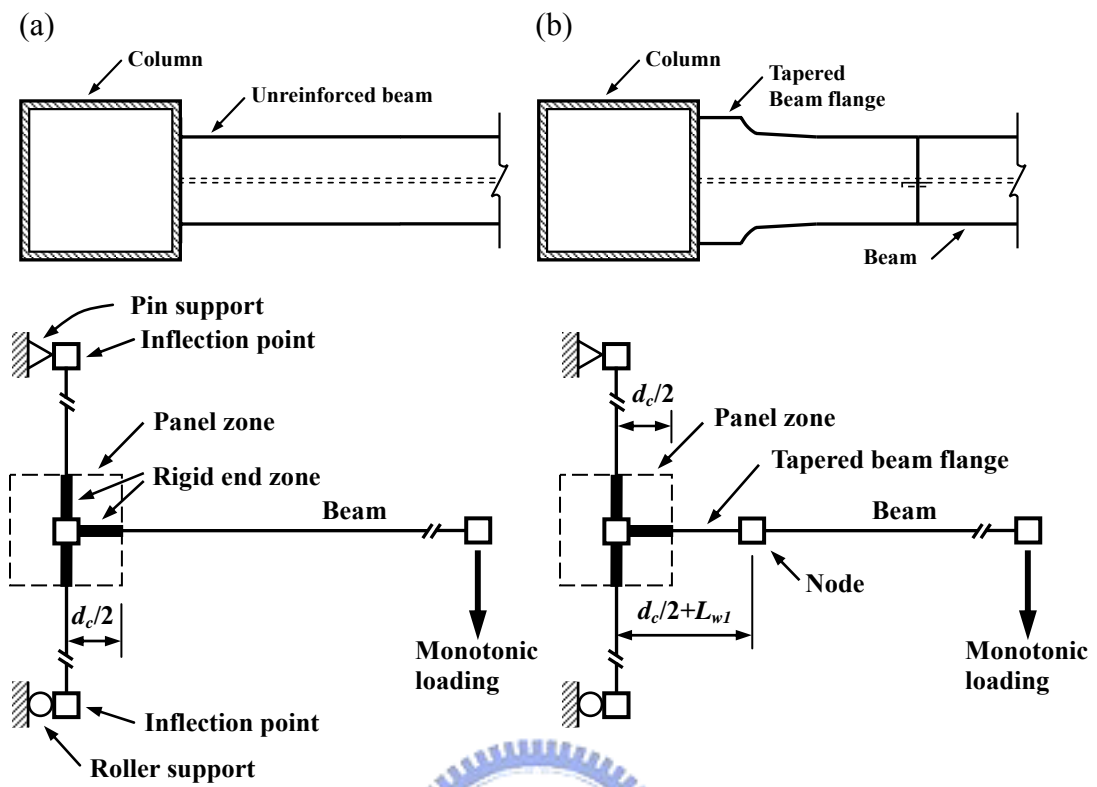


Figure 7.4 Analytical models for connection subassemblage: (a) model UR-C; (b) model TF-C.



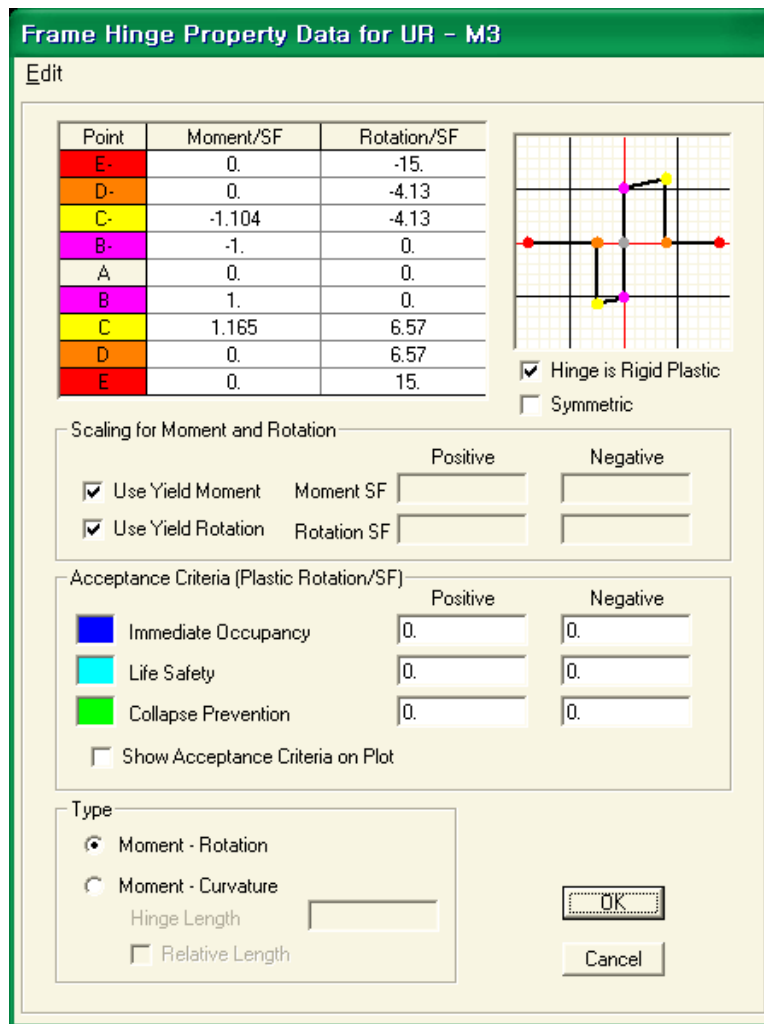


Figure 7.5 Properties of pushover hinge for model UR-C used in SAP2000.

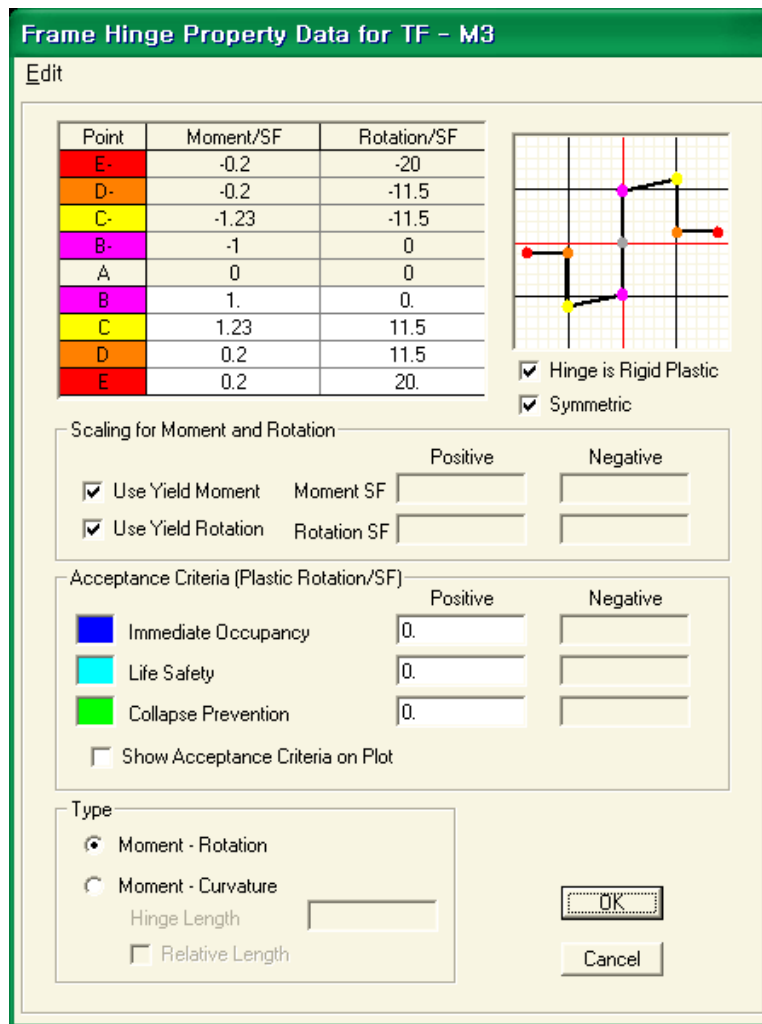


Figure 7.6 Properties of pushover hinge for model TF-C used in SAP2000.

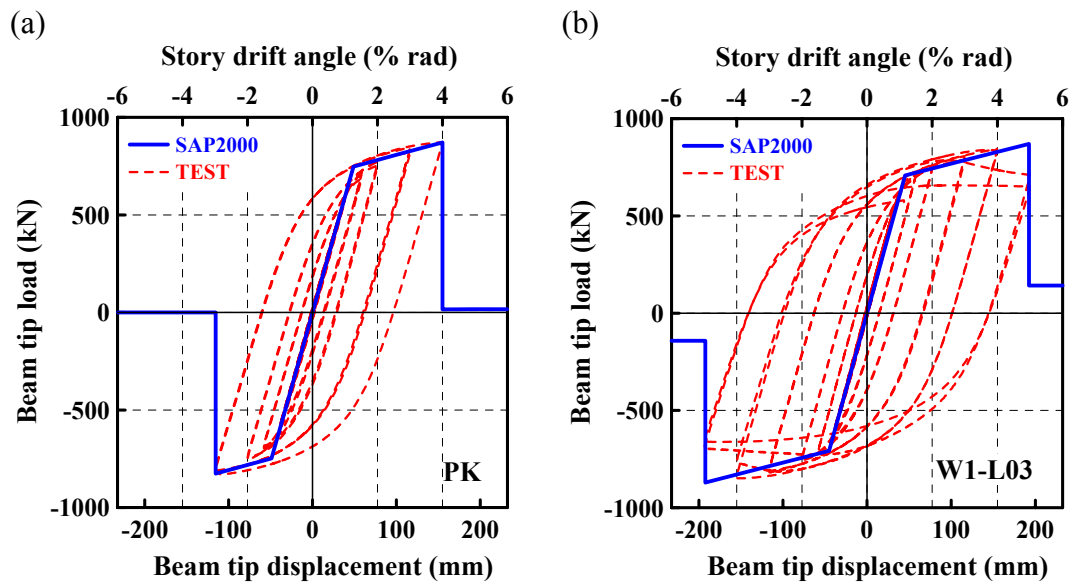


Figure 7.7 Verification of experimentally cyclic and numerically monotonic responses: (a) model UR-C; (b) model TF-C.

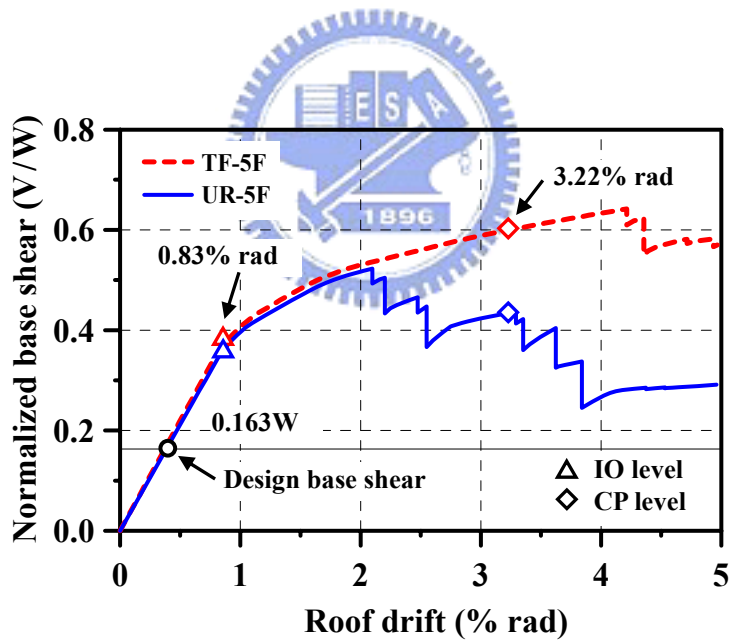


Figure 7.8 Pushover curves of normalized base shear versus roof drift for five-story frames.



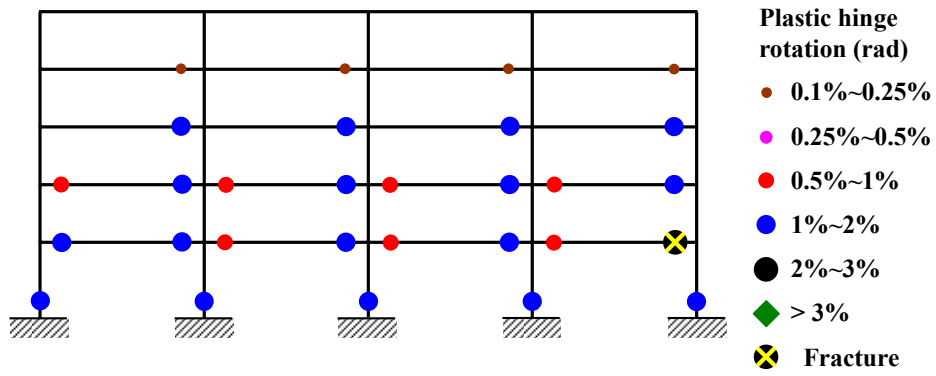


Figure 7.9 Distribution of plastic hinges for UR-5F at 2.1% rad roof drift.

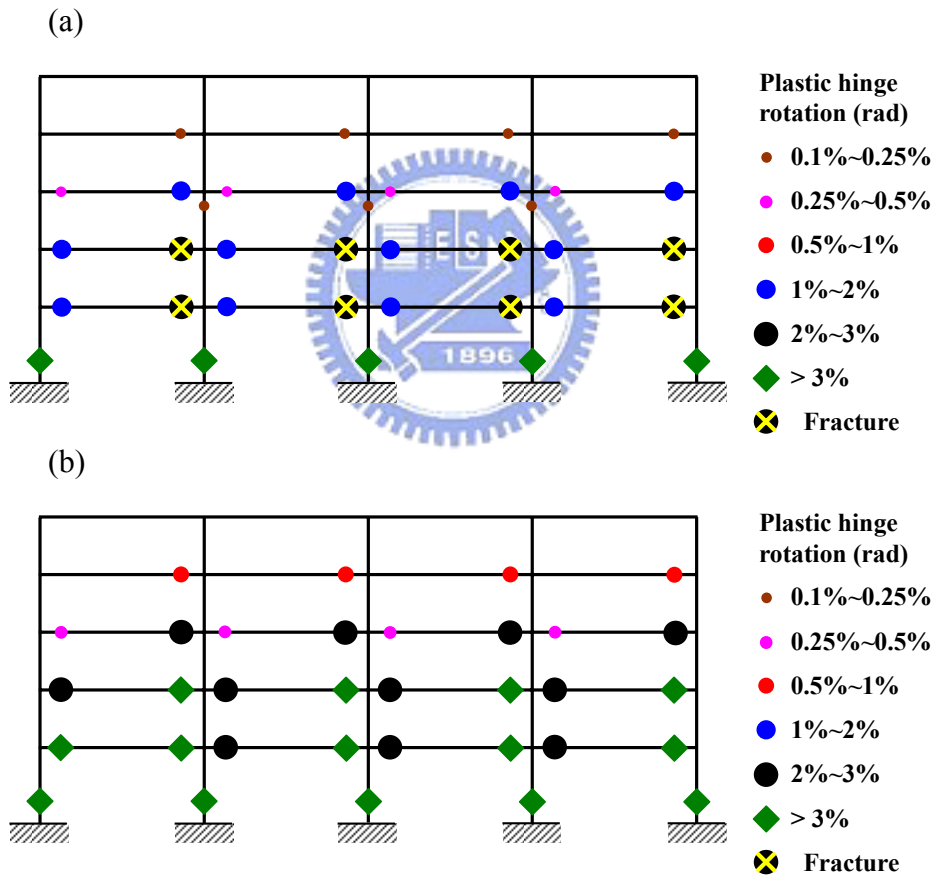


Figure 7.10 Distribution of plastic hinges at CP level (3.22% rad roof drift): (a) for UR-5F; (b) for TF-5F.

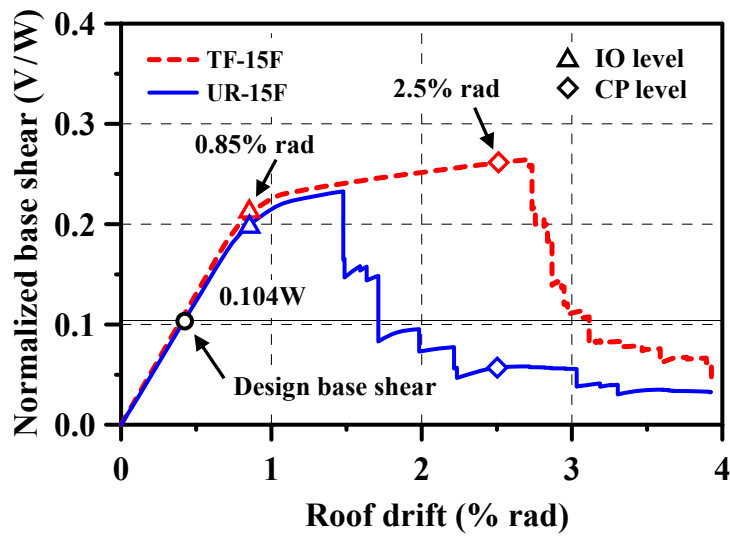


Figure 7.11 Pushover curves of normalized base shear versus roof drift for fifteen-story frames.

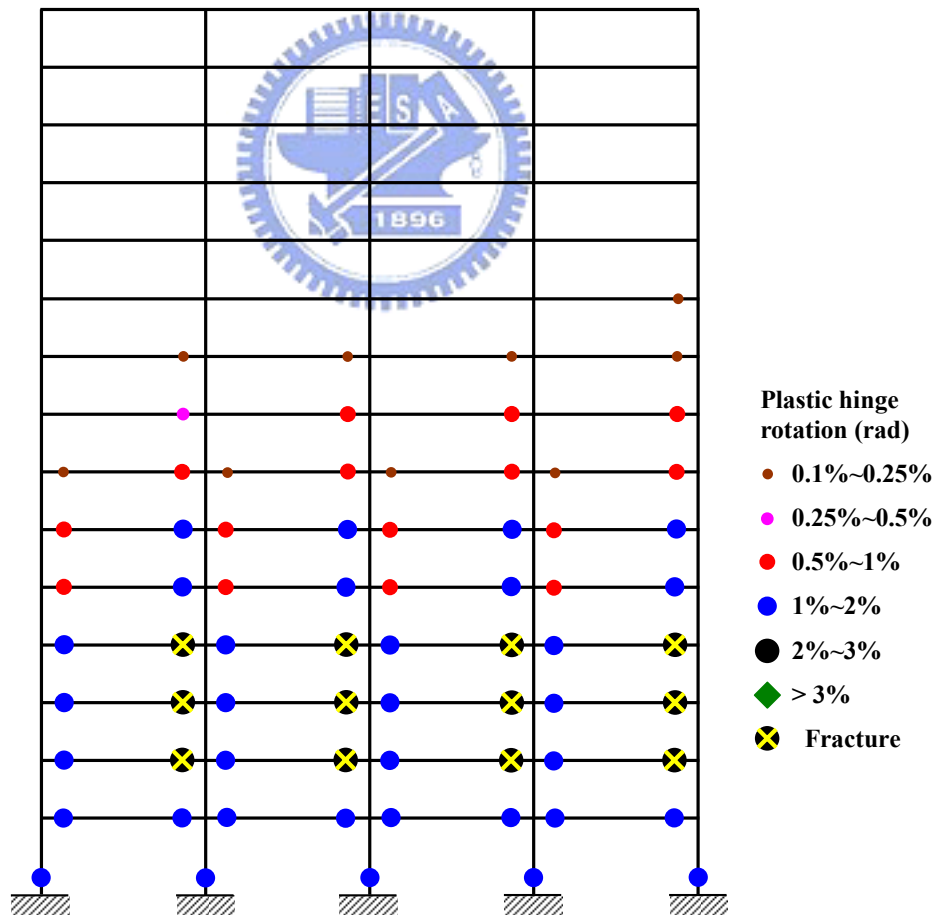


Figure 7.12 Distribution of plastic hinges for UR-15F at 1.5% rad roof drift.

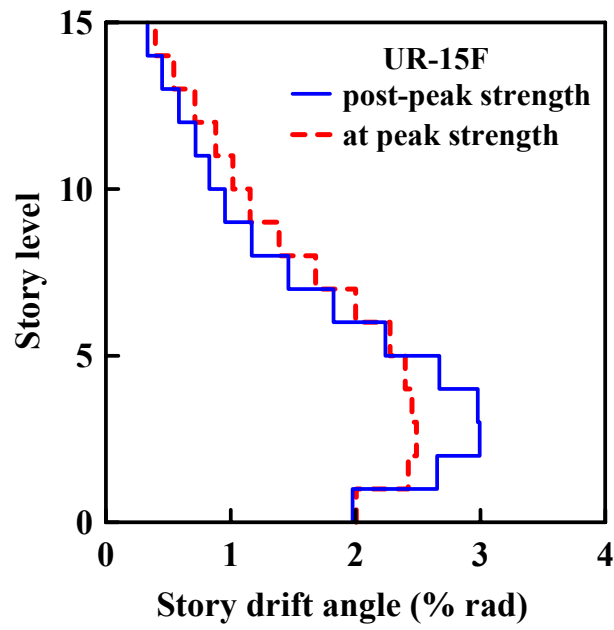


Figure 7.13 Story drift angle of UR-15F at 1.5% rad roof drift.

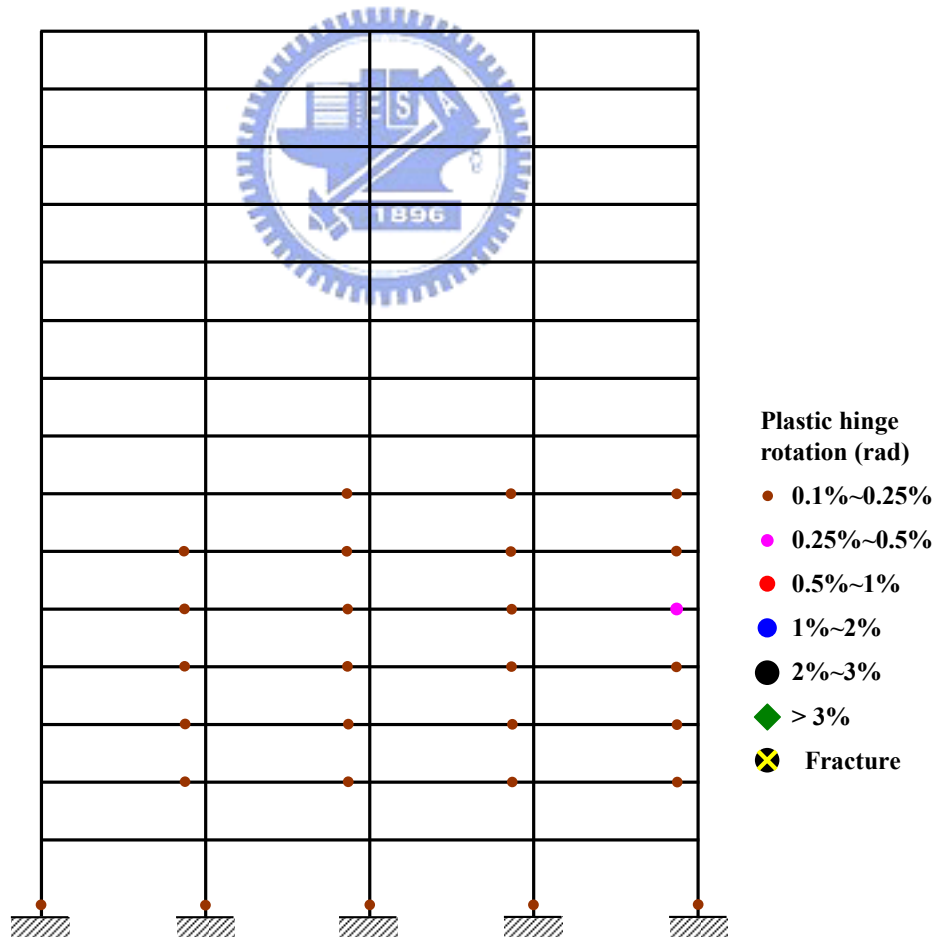


Figure 7.14 Distribution of plastic hinges for UR-15F at IO level (0.85% rad roof drift).

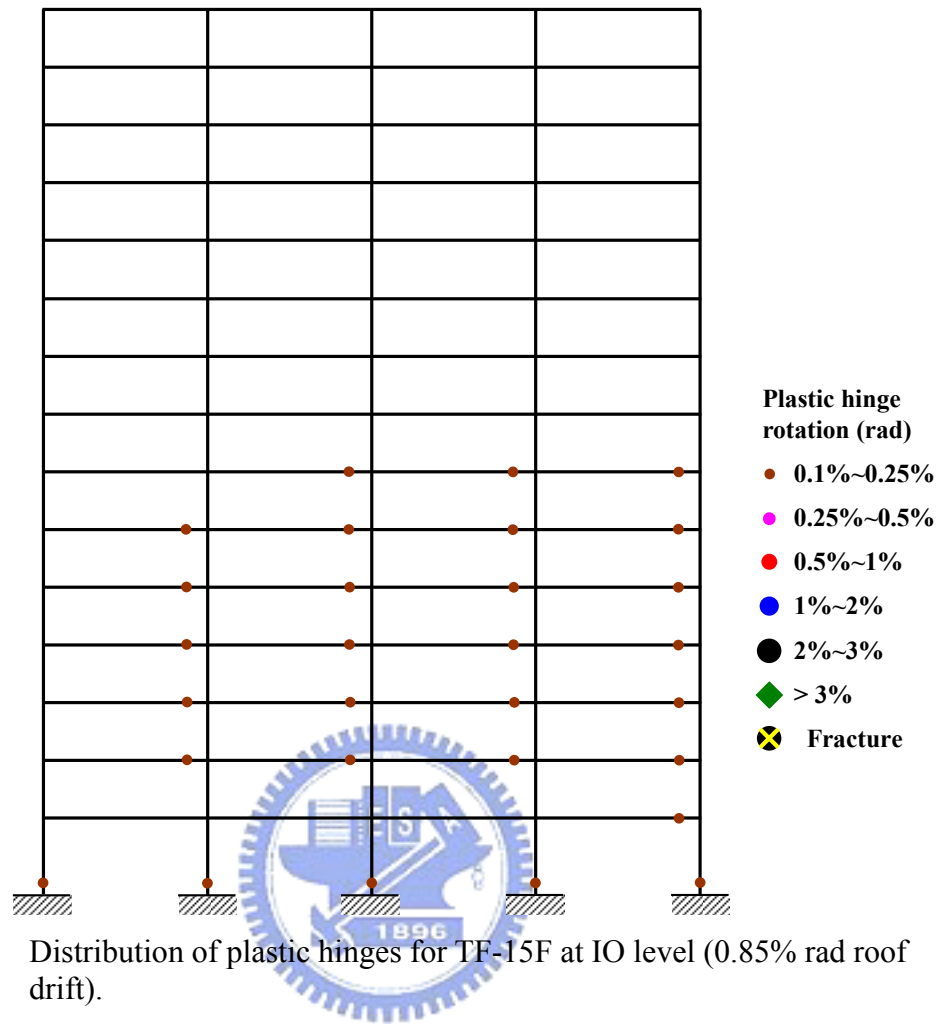


Figure 7.15 Distribution of plastic hinges for TF-15F at IO level (0.85% rad roof drift).

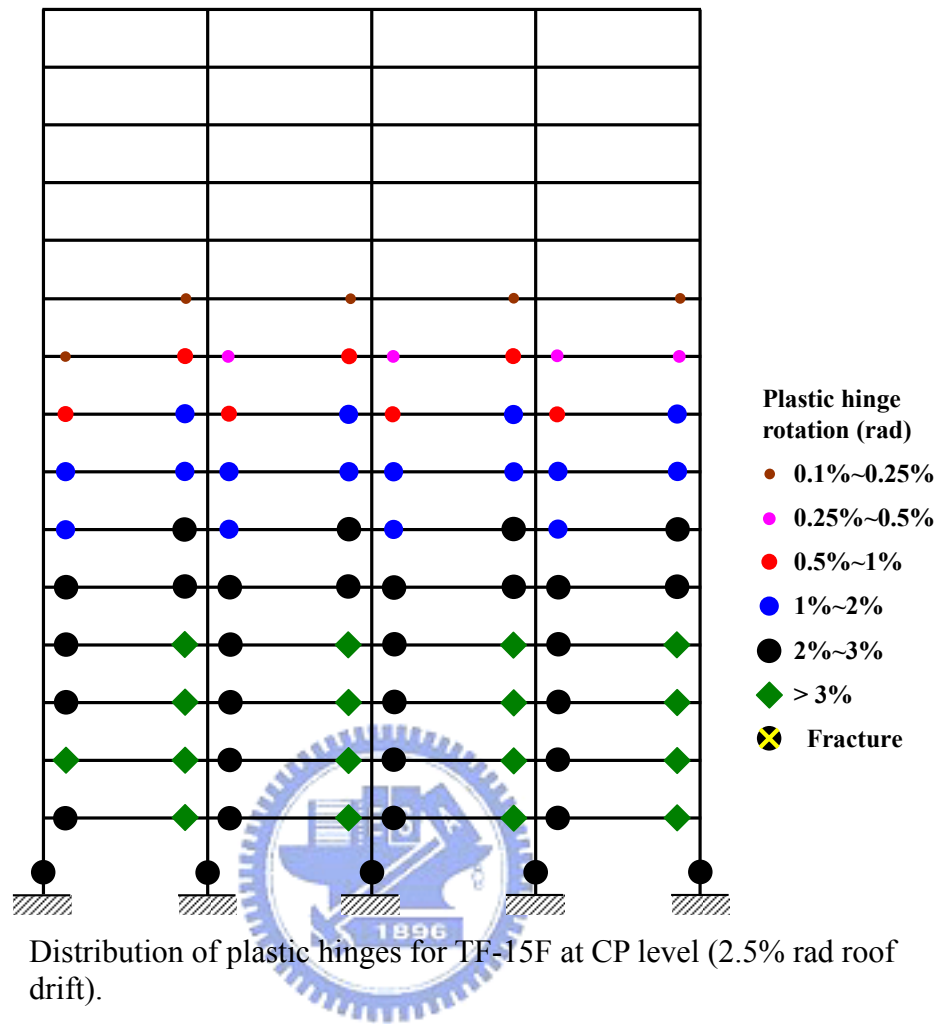


Figure 7.16 Distribution of plastic hinges for TF-15F at CP level (2.5% rad roof drift).

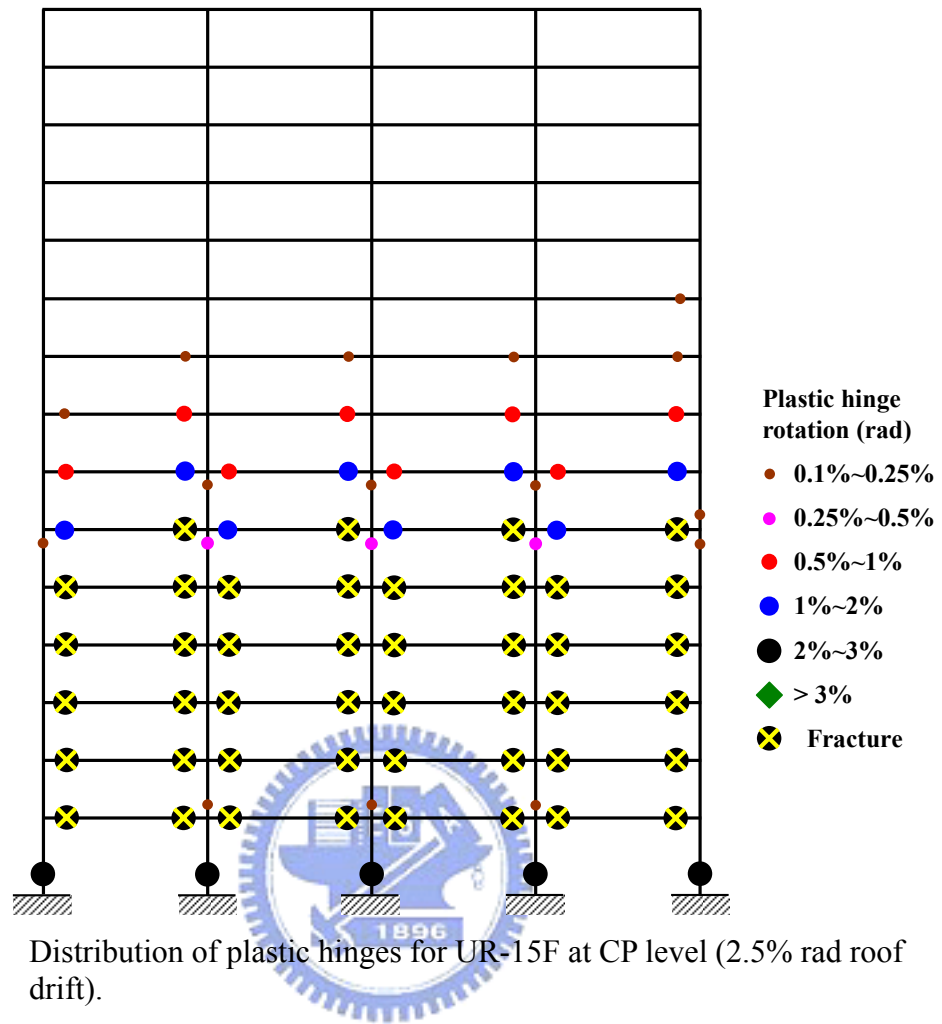


Figure 7.17 Distribution of plastic hinges for UR-15F at CP level (2.5% rad roof drift).

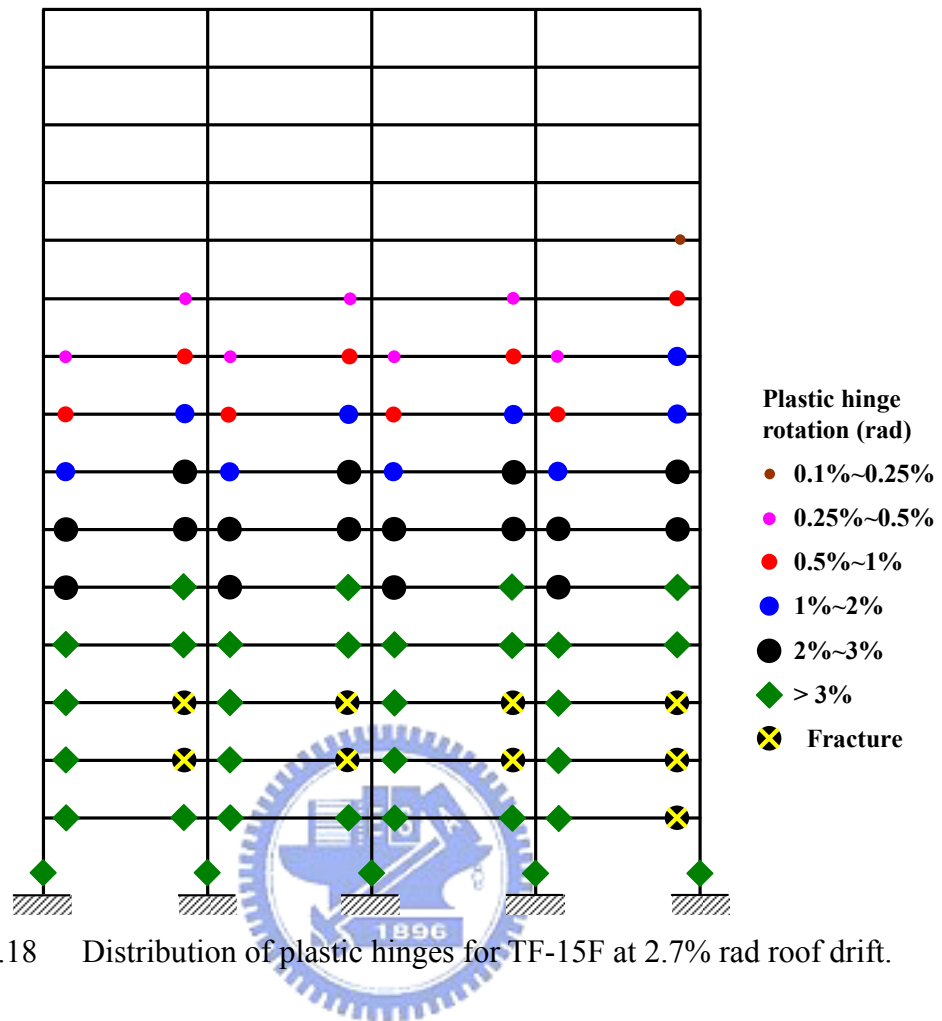


Figure 7.18 Distribution of plastic hinges for TF-15F at 2.7% rad roof drift.

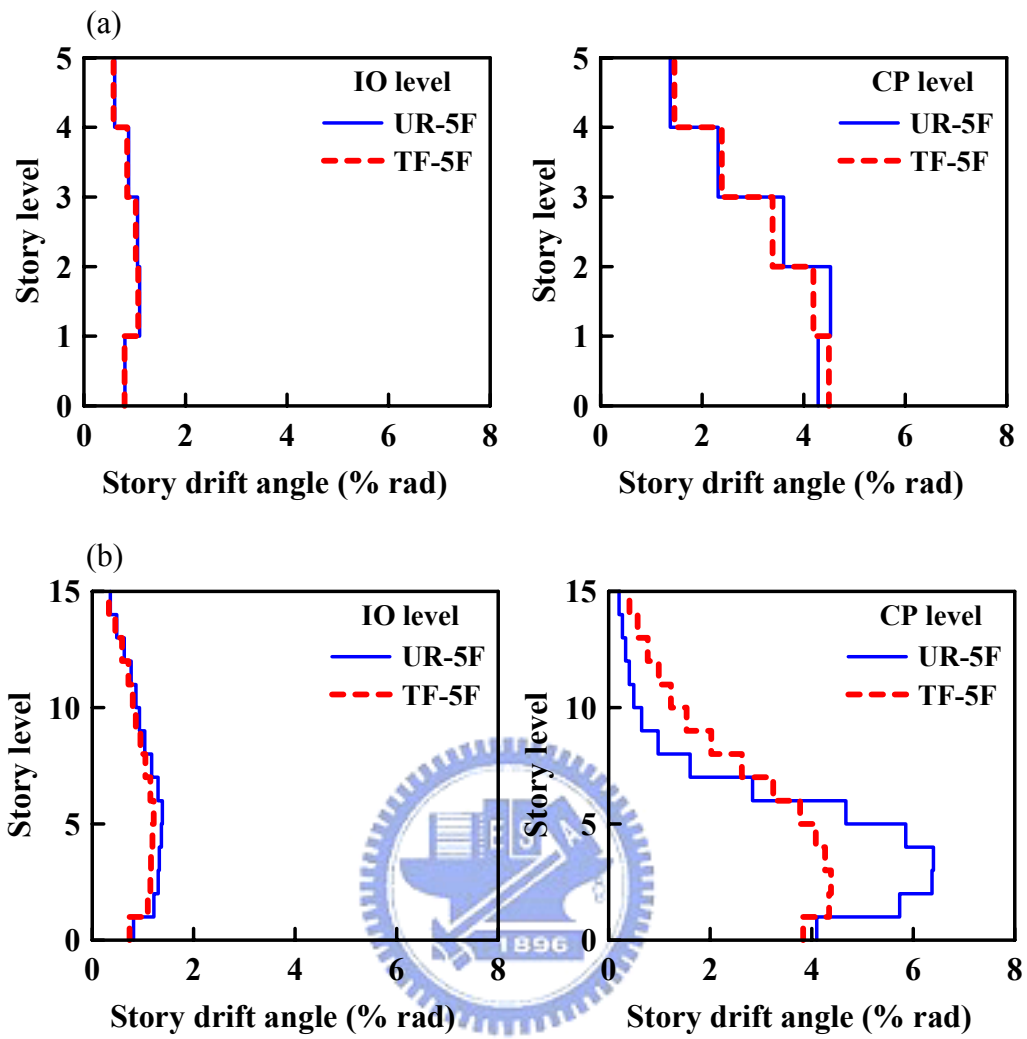


Figure 7.19 Structural demands at IO and CP performance levels: (a) for five-story frames; (b) for fifteen-story frames.



## Appendix A Design Example

To clarify the design procedure in Section 6.2, the following steps are presented to design the tapered flange for an H700×300×13×24 beam (A572 Grade 50 steel), with 8 m clear span. The H700×300×13×24 beam section properties:  $d_b=700$  mm,  $b_f=300$  mm,  $t_w=13$  mm,  $t_f=24$  mm,  $Z_b=6.25 \times 10^6$  mm<sup>3</sup>.

1. Determine beam expected plastic flexural strength,  $M_{pr}$

$$M_{pr} = C_{pr} R_y F_y Z_b = 1.2 \times 1.1 \times 345 \text{ MPa} \times 6.25 \times 10^6 \text{ mm}^3 = 2846 \text{ kN} \cdot \text{m}$$

2. Calculate design flexural strength at the end of the tapered zone,  $M_{p,tap}$

$$\begin{aligned} M_{p,tap} &= \frac{L_b - (L_{w1} + L_{w2})}{L_b - (L_{w1} + L_{w2} + L_{tap})} M_{pr} \\ &= \frac{4 \text{ m} - (0.15 + 0.05) \text{ m}}{4 \text{ m} - (0.15 + 0.05 + 0.21) \text{ m}} \times 2846 \text{ kN} \cdot \text{m} = 3013 \text{ kN} \cdot \text{m} \end{aligned}$$

3. Calculate the beam flange width at the end of the tapered zone,  $b_{f,tap}$

$$\begin{aligned} b_{f,tap} &= \frac{Z_{b,tap} - Z_{web}}{(d_b - t_f) t_f} = \frac{(M_{p,tap} / C_{pr} R_y F_y) - Z_{web}}{(d_b - t_f) t_f} \\ &= \frac{(3013 \text{ kN} \cdot \text{m} / 1.2 \times 1.1 \times 345 \text{ MPa}) - 1.38 \times 10^6 \text{ mm}^3}{(700 - 24) \text{ mm} \times 24 \text{ mm}} = 323 \text{ mm} \end{aligned}$$

4. Calculate design flexural strength at the beam-column interface,  $M_{p,j}$

$$\begin{aligned} M_{p,j} &= \beta_j M_{dem,j} = \frac{\beta_j L_b M_{pr}}{L_b - (L_{w1} + L_{w2} + L_{tap})} \\ &= \frac{1.2 \times 4 \text{ m} \times 2846 \text{ kN} \cdot \text{m}}{4 \text{ m} - (0.15 + 0.05 + 0.21) \text{ m}} = 3805 \text{ kN} \cdot \text{m} \end{aligned}$$

5. Calculate the width of the flange enlargement at the beam-column interface,  $b_{f,j}$

$$b_{f,j} = \frac{Z_{b,j} - Z_{web}}{(d_b - t_f) t_f} = \frac{(M_{p,j} / C_{pr} R_y F_y) - Z_{web}}{(d_b - t_f) t_f}$$

$$= \frac{(3805 \text{ kN} \cdot \text{m} / 1.2 \times 1.1 \times 345 \text{ MPa}) - 1.38 \times 10^6 \text{ mm}^3}{(700 - 24) \text{ mm} \times 24 \text{ mm}} = 430 \text{ mm}$$

6. Determine tapered flange extension  $L_{ext}$  and  $R$

$$L_{ext} = 0.5d_b = 350 \text{ mm}$$

$$R = L_{w1} = 0.5b_f = 150 \text{ mm}$$



## Appendix B Design Base Shear for Building

The design base shear,  $V$ , specified in the Building Seismic Design Provisions of Taiwan code (2005), is determined using Equation B.1.

$$V = \frac{I}{1.4\alpha_y} \left( \frac{S_{aD}}{F_u} \right)_m W \quad (\text{B.1})$$

and the permitted values of  $\left( \frac{S_{aD}}{F_u} \right)_m$  are

$$\left( \frac{S_{aD}}{F_u} \right)_m = \begin{cases} \frac{S_{aD}}{F_u} & ; \frac{S_{aD}}{F_u} \leq 0.3 \\ 0.52 \frac{S_{aD}}{F_u} + 0.144 & ; 0.3 < \frac{S_{aD}}{F_u} < 0.8 \\ 0.70 \frac{S_{aD}}{F_u} & ; \frac{S_{aD}}{F_u} \geq 0.8 \end{cases} \quad (\text{B.2})$$

where  $S_{aD}$  represents the mapped spectral response acceleration parameter, evaluated for the site-specified Design Earthquake (DE) hazard level;  $I$  is occupancy importance factor,  $I=1.0$  for office occupancy;  $W$  represents the total weight of building;  $\alpha_y$  is initial yield factor of seismic force,  $\alpha_y=1.2$  for steel constructional system; and  $F_u$  is structural system reduction factor of seismic force.

For the building located in Taipei basin, the mapped site-specified response acceleration parameters for evaluation of earthquake demand for the DE hazard level,  $S_{aD}$ , and Maximum Considered Earthquake (MCE) hazard level,  $S_{aM}$ , can be computed from Equation B.3 and Equation B.4.

$$S_{aD} = \begin{cases} S_{DS} (0.4 + 3T/T_0^D) & ; T \leq 0.2T_0^D \\ S_{DS} & ; 0.2T_0^D < T \leq T_0^D \\ S_{DS} T_0^D / T & ; T_0^D < T \leq 2.5T_0^D \\ 0.4S_{DS} & ; 2.5T_0^D < T \end{cases} \quad (\text{B.3})$$

$$S_{aM} = \begin{cases} S_{MS} (0.4 + 3T/T_0^M) & ; T \leq 0.2T_0^M \\ S_{MS} & ; 0.2T_0^M < T \leq T_0^M \\ S_{MS} T_0^M / T & ; T_0^M < T \leq 2.5T_0^M \\ 0.4S_{MS} & ; 2.5T_0^M < T \end{cases} \quad (\text{B.4})$$

where  $S_{DS}$  and  $S_{MS}$  represent the mapped short-period response acceleration parameter, evaluated respectively for the site-specified DE and MCE hazard level. The parameters  $S_{DS}$  of 0.6 and  $S_{MS}$  of 0.8 were adopted since the building site was assumed to locate in Taipei seismic zone 1.  $T_0^D$  and  $T_0^M$  are the boundary period between a short period and a middle period and equal to 1.6 seconds for this design case.  $T$  is the fundamental period of the building.

The structural system reduction factor,  $F_u$ , can be determined from Equation B.5:

$$F_u = \begin{cases} R_a & ; T \geq T_0^D \\ \sqrt{2R_a - 1} + (R_a - \sqrt{2R_a - 1}) \times \frac{T - 0.6T_0^D}{0.4T_0^D} & ; 0.6T_0^D \leq T \leq T_0^D \\ \sqrt{2R_a - 1} & ; 0.2T_0^D \leq T \leq 0.6T_0^D \\ \sqrt{2R_a - 1} + (\sqrt{2R_a - 1} - 1) \times \frac{T - 0.2T_0^D}{0.2T_0^D} & ; T \leq 0.2T_0^D \end{cases} \quad (\text{B.5})$$

where  $R_a$  is allowable ductility capacity of structural system. For Taipei basin, this value can be calculated from Equation B.6, below:

$$R_a = 1 + \frac{(R-1)}{2} \quad (\text{B.6})$$

where the ductility capacity of structural system  $R$  of 4.8 is used for steel SMF system.

Therefore,  $F_u$  is calculated using Equation B.5 of  $\sqrt{2R_a - 1}$  with  $R_a = 2.9$ .

Eventually, the seismic base shear can be calculated by using the above parameters.



## 個人簡歷



姓名：林群洲 (Chun-Chou Lin)

生日：1978/ 04/ 16

學歷：私立中原大學土木工程學系 學士 (1996~2000)

國立交通大學土木工程學系 結構組碩士 (2000~2002)

國立交通大學土木工程學系 結構組博士 (2002~2006)

榮耀：中興工程科技研究發展基金會獎學金 (2004~2006)

電郵：cclin1@gmail.com

學術著作：

(A) 期刊論文

1. Chen, Cheng-Chih, Lin, Chun-Chou, and Lin, Chieh-Hsiang, (2006), “Ductile moment connections used in steel column-tree moment-resisting frames.” *Journal of Constructional Steel Research*, Vol. 62, No. 8, pp 793-801.
2. Chen, Cheng-Chih, Lu, Cheng-An, and Lin, Chun-Chou, (2005), “Parametric study and design of rib-reinforced steel moment connections.” *Engineering Structures*, Vol. 27, No. 5, pp 699-708.
3. Chen, Cheng-Chih, Lin, Chun-Chou, and Tsai, Chia-Liang, (2004), “Evaluation of reinforced connections between steel beams and box columns.” *Engineering Structures*, Vol. 26, No. 13, pp 1889-1904.
4. 陳誠直、林群洲，(2005)，「扇形焊接開孔于鋼骨梁柱接頭耐震行為之影響」，*建築鋼結構進展*，第七卷，第五期，50-56 頁。

(B) 研討會論文

1. Lin, Chun-Chou, Chen, Cheng-Chih, and Lee, Chih-Ming, (2006), "Experimental evaluation of steel moment connections with a widened beam flange." *Proceedings of the tenth East Asia-Pacific Conference on Structural Engineering & Construction (EASEC)*, Bangkok, Thailand, Vol. 6, pp. 45-50.
2. Chen, Cheng-Chih, Lin, Chun-Chou, and Lu, Cheng-An, (2004), "Analytical evaluation of rib-reinforced steel moment connections." *Proceedings of the sixth Korea-Taiwan-Japan Joint Seminar on Earthquake Engineering for Building Structures (SEEBUS)*, Taiwan, pp 239-247.
3. 陳誠直、林群洲、陳澤許、張新梓，(2004)，「鋼骨箱型柱梁柱偏心接合試驗研究」，第七屆結構工程學術研討會，台灣中壢。
4. 林群洲、陳誠直，(2003)，「接合細部於箱型柱梁柱接頭行為之影響」，第二十七屆全國力學會議，台灣台南。
5. 陳誠直、林群洲、蔡佳良，(2002)，「鋼骨箱型柱梁柱接頭之肋板補強試驗」，第六屆結構工程學術研討會，台灣墾丁。

(C) 技術報告

1. 林群洲，(2006)，「鋼骨托梁抗彎接頭含梯度漸擴式梁翼板之耐震行為」，中興工程科技研究發展基金會獎學金研究成果報告。
2. 林群洲，(2005)，「肋板補強式梁柱接頭於鋼骨抗彎構架之耐震行為」，中興工程科技研究發展基金會獎學金研究成果報告。
3. 陳誠直，林群洲，林潔祥，(2005)，「鋼構造抗彎接頭耐震行為」，國科會專題研究計畫成果報告 NSC93-2211-E-009-024。
4. 陳誠直、林群洲、陳澤許、張新梓，(2004)，「箱型柱與鋼梁偏心接合耐震行為研究」，中興工程顧問社專案研究報告 R-ST-04-04。
5. 陳誠直、林群洲、蔡佳良，(2002)，「鋼骨箱型柱肋板補強梁柱接頭耐震行為」，中興工程顧問社專案研究報告 R-ST-02-05。